Nanoscale

REVIEW

View Article Online
View Journal | View Issue

Cite this: *Nanoscale*, 2019, **11**, 19012

Advances in the synthesis and design of nanostructured materials by aerosol spray processes for efficient energy storage

Jin-Sung Park,†[a] Jin Koo Kim, †[a] Jeong Hoo Hong,[a] Jung Sang Cho,[b] Seung-Keun Park [c] and Yun Chan Kang *[a]

The increasing demand for energy storage has motivated the search for highly efficient electrode materials for use in rechargeable batteries with enhanced energy density and longer cycle life. One of the most promising strategies for achieving improved battery performance is altering the architecture of nanostructured materials employed as electrode materials in the energy storage field. Among numerous synthetic methods suggested for the fabrication of nanostructured materials, aerosol spray techniques such as spray pyrolysis, spray drying, and flame spray pyrolysis are reliable, as they are facile, cost-effective, and continuous processes that enable the synthesis of nanostructured electrode materials with desired morphologies and compositions with controlled stoichiometry. The post-treatment of spray-processed powders enables the fabrication of oxide, sulfide, and selenide nanostructures hybridized with carbonaceous materials including amorphous carbon, reduced graphene oxide, carbon nanotubes, *etc*. In this article, recent progress in the synthesis of nanostructured electrode materials by spray processes and their general formation mechanisms are discussed in detail. A brief introduction to the working principles of each spray process is given first, and synthetic strategies for the design of electrode materials for lithium-ion, sodium-ion, lithium–sulfur, lithium–selenium, and lithium–oxygen batteries are discussed along with some examples. This analysis sheds light on the synthesis of nanostructured materials by spray processes and paves the way toward the design of other novel and advanced nanostructured materials for high performance electrodes in rechargeable batteries of the future.

Received 2nd July 2019,
Accepted 3rd August 2019

DOI: 10.1039/c9nr05575d

rsc.li/nanoscale

1. Introduction

Nanostructured materials and their impact on diverse applications are of immense importance, and they have continued to attract attention due to their tailorable physicochemical properties that are distinct from their bulk counterparts. In particular, the architecture of nanostructured materials with optimum composition and controlled morphology is considered a critical strategy for achieving high performance electrode materials for lithium-ion batteries (LIBs), which currently represent the dominant power source, as well as for next-generation batteries including sodium-ion (SIB), lithium–sulfur (Li–S), lithium–selenium (Li–Se), and lithium–oxygen (Li–O_2) batteries.[1–5] To meet the skyrocketing demands for energy storage materials with high energy density and long cycle life, extensive efforts have been made to design and synthesize nanostructured materials suitable for energy storage devices.[6–15]

Various liquid-phase techniques including hydrothermal, sol–gel, and microwave processes have been proposed to synthesize nanostructured materials designed for enhancing the electrochemical properties of electrode materials.[16–28] The advantages of liquid-phase processes include the formation of nanostructures with precisely controlled morphology and ultrafine particles with unimodal size distributions by exploiting the slow reaction rate of the process.[29–33] However, the liquid phase process faces some difficulty in synthesizing nanostructured materials with desired compositions, as composition diversity is limited to some degree. Nanostructured materials synthesized *via* the liquid process undergo structural changes with respect to composition differences, which can act both as an advantage or disadvantage when employed as an electrode material in rechargeable batteries.

Among the synthesis methods, the spray process, a type of gas-phase process, has received much attention since it is a continuous process that can easily be scaled up.[34–44] The spray

[a]*Department of Materials Science and Engineering, Korea University, Anam-dong, Seongbuk-gu, Seoul 136-713, Republic of Korea. E-mail: yckang@korea.ac.kr; Fax: +82 2-928-3584*
[b]*Department of Engineering Chemistry, Chungbuk National University, Chungdae-ro 1, Seowon-gu, Cheongju, Chungbuk 361-763, Republic of Korea*
[c]*Department of Chemical Engineering, Kongju National University, Budae-dong 275, Cheonan, Chungnam 314-701, Republic of Korea*
† These authors contributed equally to the work.

techniques include spray pyrolysis, spray drying, and flame spray pyrolysis processes. In general, spray pyrolysis involves the atomization of droplets from a precursor solution using ultrasonic power and subsequent evaporation and decomposition in a thermal reactor. The spray drying process, which mainly uses a two-fluid nozzle to produce atomized micron-sized droplets, followed by drying in a heated chamber, yields microspheres with a desired composition. Flame spray pyrolysis uses atomized droplets that are carried into the high-temperature flame. The droplets go through evaporation, nucleation, and growth steps to produce nanosized powders. Nanostructured materials prepared from spray processes have been investigated for application in electrode materials for rechargeable batteries. Merits of spray processes include homogeneous composition, since micron-sized droplets are atomized from a solution with a desired ratio of precursor materials, and ease of fabricating carbon composite microspheres.[34–44] Furthermore, the spherical shape can be obtained from the spray processes, which is advantageous for achieving high packing density. Finally, the addition of template materials that can be dissolved or dispersed in the spray solution enables tailoring of the nanostructure in the obtained powder.

The synthesis of materials with an ideal composition and desired nanostructure suitable for electrode materials by the spray process requires a comprehensive understanding of various formation mechanisms. The representative formation mechanisms can be summarized as follows: application of various organic additives, combustion of a carbon composite, Kirkendall diffusion, phase separation, inorganic/organic templates, use of colloidal particles, *etc*. Through the understanding and application of various formation mechanisms to spray processes, numerous studies were reported on the synthesis of nanostructures *via* the spray process for applications not only in energy storage, but also in gas sensing, water splitting, *etc*.[42–56] Particularly in the field of energy storage, the formation mechanisms in the spray process enable a facile synthesis of a carbon composite, which is highly beneficial for the cycling and rate performances of electrode materials in the anodes of rechargeable batteries.[41–44] In addition, the controlled porosity in nanostructured materials prepared from the spray process leads to a longer battery life and power density. Thus, taking into account the emerging popularity of spray processes for the fabrication of nanostructured materials for energy storage applications, a thorough understanding of the formation mechanisms in the spray processes is required.

Here, research conducted on the synthesis of nanostructured materials applicable to electrode materials in rechargeable batteries by the spray process was investigated and analyzed with respect to the formation mechanisms. First, a brief introduction to spray processes, including spray pyrolysis, spray drying, and flame spray pyrolysis, is presented. Different strategies for designing nanostructured materials with desired properties are explained in detail, and nanostructured materials representative for each formation mechanism reported in the literature are introduced. The last section provides a summary and discussion of the current status and future outlook regarding the synthesis of nanostructured materials *via* the spray process.

2. Preparation of particles by spray processes

In this section, spray processes including spray pyrolysis, spray drying, and flame spray pyrolysis are examined along with their working principles.

2.1 Spray pyrolysis

The spray pyrolysis process is comprised of the "spray" step, in which the precursor solution is atomized into a droplet by ultrasonic force, and the "pyrolysis" step, where the droplets evaporate and decompose in a thermal reactor. The schematic diagram of the spray pyrolysis apparatus is shown in Scheme 1a. First, the solution containing chemical components is atomized into droplets using an ultrasonic spray nebulizer with a desired number of sonic vibrators to produce a large quantity of droplets. The generated droplets are then transported to a heated reactor using carrier gas, and then par-


Jin-Sung Park

Jin-Sung Park is a Ph.D. candidate at Korea University under the supervision of Prof. Yun Chan Kang. He received his Bachelor's degree from the Department of Materials Science and Engineering, Korea University, Seoul, Korea in 2015. His current research focuses on the development of nanostructured materials by spray processes for use in energy storage, catalysis, and gas sensing.


Jin Koo Kim

Jin Koo Kim is a Ph.D. candidate at Korea University under the supervision of Prof. Yun Chan Kang. He received his Bachelor's degree from the Department of Materials Science and Engineering, Korea University, Seoul, Korea in 2016. His current research focuses on the development of nanostructured materials by spray processes for use in energy storage, catalysis, and gas sensing.

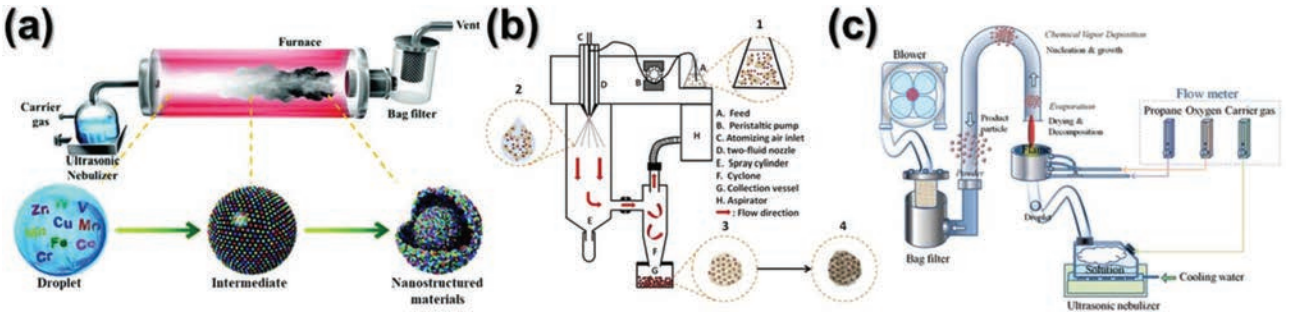

Scheme 1 Schematic diagrams for the typical apparatus for (a) spray pyrolysis, (b) spray drying, and (c) flame spray pyrolysis processes. Reproduced with permission from ref. 163. Copyright 2014, The Royal Society of Chemistry. Reproduced with permission from ref. 244. Copyright 2012, American Chemical Society. Reproduced with permission from ref. 348. Copyright 2014, The Royal Society of Chemistry.

ticles are formed through evaporation, decomposition, and crystallization steps. Notably, the residual time of particles in the reactor furnace is in the range as low as several seconds, and an aggregate-free spherical powder is obtained, since the reactions are confined within each microreactor (droplet). Various types of gases such as air, argon, and a hydrogen/argon mixture can be used as a carrier gas to produce powder with a desired composition. Finally, the powder is generally collected in a bag filter. Micron-sized powder with a narrow size distribution can be obtained from spray pyrolysis, since one spray-pyrolyzed microsphere originates from a single droplet atomized at the same frequency. Subsequent post heat treatments such as oxidation, reduction, sulfidation, *etc.*, can be further performed to obtain the desired nanostructured materials.

2.2 Spray drying

The spray drying process produces powder from an atomized droplet by rapid drying with a hot gas in a heated chamber. Droplets are formed by pneumatic atomization using a two-fluid nozzle. The solution and gas are consecutively injected to the inner core and outer nozzle, and aerosol droplets are formed due to the disintegration of the liquid because of the large difference in the velocity between the gas and liquid that cause shear force. Spray drying is conventionally used for drying foods and pharmaceuticals, but advances have been made in the field of energy storage using the spray drying process owing to its scalability, cost-efficiency, and capability to produce spherical particles. A schematic diagram of the spray drying process is illustrated in Scheme 1b. First, the solution containing the desired chemical components is injected into the inner core of the two-fluid nozzle using a peristaltic pump. The solution is then atomized into droplets due to the compressed air flow into the outer nozzle, and the droplets are rapidly dried as they enter the heated chamber. A cyclone is used to separate particles with a desired size, and the product is collected at the collection vessel. The obtained spray-dried powders undergo the drying step in a heated chamber and are vulnerable to humidity, thus post heat treatment must be conducted for their use in energy storage applications.

2.3 Flame spray pyrolysis

Flame spray pyrolysis is a gas-phase combustion method that uses a high-temperature flame. It is suitable for the synthesis of nanosized metal oxide and doped metal oxide particles. The

Jeong Hoo Hong

Jeong Hoo Hong is a Ph.D. candidate at Korea University under the supervision of Prof. Yun Chan Kang. He received his Bachelor's degree from the Department of Chemical Engineering, Kyung Hee University, Suwon, Korea in 2018. His current research focuses on the development of nanostructured materials by spray processes for use in energy storage, catalysis, and gas sensing.

Jung Sang Cho

Prof. Jung Sang Cho received his Ph.D. from the Interdisciplinary Program for Bioengineering, Seoul National University, Korea in 2013, and had post-doc experience at the Department of Materials Science and Engineering, Korea University, Korea (2014–2016). He has been a professor at the Department of Engineering Chemistry, Chungbuk National University, Cheongju, Korea since 2016. His research group works on the development of nanostructured materials for energy storage, sensors, catalysts, displays, and biomaterials.

schematic diagram of the flame spray pyrolysis is illustrated in Scheme 1c. Generally, the precursor solution is atomized by the use of an ultrasonic spray nebulizer, and the droplets are carried to a premixed propane-oxygen flame at temperatures >2000 °C. The aerosolized droplet undergoes decomposition of precursors, evaporation, and nucleation & growth of particles in sequence, resulting in the formation of nanosized metal oxide nanoparticles. After the aerosol stream passes through the part of the flame with high temperature, particles cool down and are collected in the bag filter. To obtain nanoparticles with a desired morphology and crystallinity, the element types, processing temperature, and residence time in flame should be controlled, as these factors affect the degree of particle coalescence or sintering. In some cases, the synthesized nanoparticles need additional heat treatment steps for their use in energy storage applications.

3. Formation mechanisms of nanostructured materials for energy storage applications

3.1 Application of metal precursors and organic additives

3.1.1 Metal precursors. The type and concentration of metal salts can determine the morphology and the size of the nanostructured materials synthesized from spray processes. The key requirements for the attributes of metal salts concern their solubility and decomposition temperature. The groups of metal salts that meet the required criteria are inorganic compounds including nitrate, sulfate, and chloride, as well as metal–organic compounds such as acetate, oxalate, alkoxide, *etc.*[57–73] Inorganic compounds are easily dissolved in aqueous solutions and are inexpensive, thus they are most commonly used for spray processes. Li *et al.* demonstrated in a study that the selection of different metal precursors results in different morphologies and microstructures in the spray pyrolysis process (Fig. 1a).[74] The atomized droplets undergo solvent evaporation, decomposition, and crystallization processes during the pyrolysis process and result in different morphologies attributed to the differences in the solubility, supersaturation degree, and thermal characteristics of various metal salts. Scanning electron microscopy (SEM) images shown in Fig. 1b–d reveal that the morphologies obtained from aqueous solutions containing cobalt acetate, chloride, and nitrate salts exhibit microspheres with a wrinkled surface (A–Co_3O_4), porous spherical shape (C–Co_3O_4), and durian-like hollow spherical shape (N–Co_3O_4). C–Co_3O_4 exhibits the highest discharge capacity of 961 mA h g^{-1} after 200 cycles at 0.4 A g^{-1}, whereas the discharge capacities for A–Co_3O_4 and N–Co_3O_4 were 593 mA h g^{-1} and 326 mA h g^{-1}, respectively. Ju *et al.* observed the morphological variation of spray-pyrolyzed microspheres prepared from various Mn precursors including chloride, nitrate, and acetate, and employed them as the cathode in LIBs.[75] Particles prepared from the spray pyrolysis of manganese acetate and chloride precursors exhibited hollow and porous morphologies. In contrast, those prepared from a nitrate precursor exhibited dense and spherical morphologies. The discharge capacity retention of particles prepared from Mn nitrate after 25 cycles at 0.1C rate was 85% of their initial value. However, in most cases it is not easy to precisely predict the type of morphology prepared from spray processes due to the complexity in combination of metal salts and additives dissolved in the spray solution. Ko *et al.* synthesized hollow cobalt selenide microspheres *via* spray pyrolysis for use as anode materials in SIBs (Fig. 1e).[76] First, hollow cobalt oxide microspheres were prepared from spray pyrolysis of the cobalt nitrate precursor solution and then selenized under an H_2/Ar atmosphere, as shown in SEM and transmission electron microscopy (TEM) images in Fig. 1f–h. The hollow morphology was obtained during the spray pyrolysis step due to the fast drying rate of droplets and rapid decomposition of metal salts. When applied as the anode material for SIBs, a discharge capacity of 467 mA h g^{-1} was achieved after 40 cycles at

Seung-Keun Park

Prof. Seung-Keun Park received his Ph.D. from the Graduate School of Convergence Science and Technology, Seoul National University, Korea in 2016. He then joined Prof. Yun Chan Kang's lab as a post-doc at the Department of Materials Science and Engineering, Korea University, Seoul, Korea. He has been a professor at the Department of Chemical Engineering, Kongju National University, Cheonan, Korea since 2018. His research group focuses on the design and synthesis of nanostructured materials for energy storage applications.

Yun Chan Kang

Prof. Yun Chan Kang received his Ph.D. from the Department of Chemical Engineering, Korea Advanced Institute of Science and Technology (KAIST), Korea in 1997. He became a professor at the Department of Chemical Engineering, Konkuk University, Seoul, Korea (2004–2014). He has been a professor at the Department of Materials Science and Engineering, Korea University, Seoul, Korea since 2014. His research group works on the development of nanostructured materials by spray processes for energy storage.

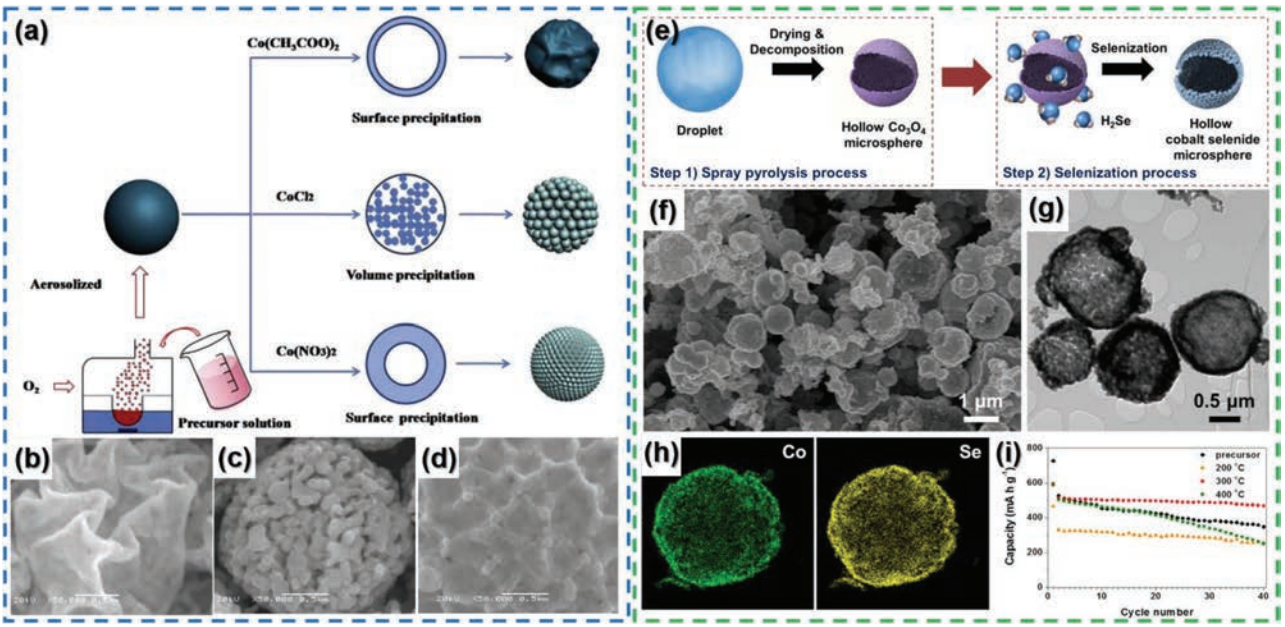

Fig. 1 (a) Schematic illustration of the synthetic process of A–Co_3O_4, C–Co_3O_4, and N–Co_3O_4. SEM images of (b) A–Co_3O_4, (c) C–Co_3O_4, and (d) N–Co_3O_4. Reproduced with permission from ref. 74. Copyright 2017, Elsevier. (e) Schematic illustration for the preparation procedure of the hollow cobalt selenide microspheres, (f) SEM and (g) TEM images of the nanostructured microspheres, (h) elemental dot mapping images, and (i) cycling performance. Reproduced with permission from ref. 76. Copyright 2016, American Chemical Society.

0.5 A g^{-1} (Fig. 1i). Park *et al.* synthesized mesoporous cobalt hydroxychloride microspheres prepared from a spray solution containing cobalt chloride under a nitrogen atmosphere at 700 °C.[77] The discharge capacities of $Co_2(OH)_3Cl$ for the 2nd and the 1000th cycles were 818 mA h g^{-1} and 609 mA h g^{-1}, respectively, when cycled at 5 A g^{-1}.

3.1.2 Organic additives. Many studies have addressed the morphology variation of the powder obtained from spray processes according to the use of numerous organic additives including citric acid, ethylene glycol, sucrose, dextrin, polyvinylpyrrolidone (PVP), *etc.*[78–98] This section describes the formation of microspheres with hollow and dense morphologies *via* spray processes using organic additives. Citric acid has been widely studied for the fabrication of microspheres with hollow morphologies.[79–87] Kim *et al.* synthesized hollow cobalt sulfide–carbon composite microspheres by a spray drying process using a precursor solution containing cobalt salts and citric acid for use as the anode in LIBs.[99] It is highly probable that the microspheres formed from the metal chelates of citric acid showed a low degree of gas penetration, and a large amount of gas evolved during citric acid decomposition, triggering the formation of hollow structures. The spray-dried microspheres were post-treated and tested as anode materials for LIBs, where a discharge capacity of 790 mA h g^{-1} was achieved after 70 cycles at 1 A g^{-1}. In some cases, different types of organic additives can be applied to synthesize hollow microspheres with unique morphologies.[100–111] Park *et al.* employed tartaric acid as the organic precursor in the spray solution and obtained hollow microspheres comprised of Sb nanoparticle-embedded in a carbon/reduced graphene oxide (rGO) composite shell with empty rooms.[112] When employed as the anode for SIBs, the microspheres exhibited a discharge capacity of 320 mA h g^{-1} after 500 cycles at 0.5 A g^{-1}, and the capacity retention measured from the 5th cycle was 80%.

Other organic additives including sucrose, dextrin, and PVP can be employed in spray processes for the synthesis of unique structures that are applicable in the energy storage field.[88–98,113–116] Sucrose was applied to synthesize dense, hollow, and yolk–shell structured microspheres by controlling the carrier gas type and sucrose concentration in aqueous solution.[88–94] Zachariah's group reported on the synthesis of Mn_3O_4 hollow spheres used as the anode in LIBs.[113] Manganese nitrate, sucrose, and hydrogen peroxide solution were added to the precursor solution and sprayed under an air atmosphere (Fig. 2a). The aerosol underwent surface precipitation and solvent evaporation, and thus the hollow morphology was obtained (Fig. 2b and c). A discharge capacity of 980 mA h g^{-1} was achieved after the 140th cycle at 0.2 A g^{-1} (Fig. 2d). At high current densities of 5 A g^{-1} and 10 A g^{-1}, the discharge capacities of 520 mA h g^{-1} and 300 mA h g^{-1} were obtained, respectively (Fig. 2e). If a large amount of sucrose had been added to the spray solution containing the metal salt, microspheres with a yolk–shell structure would have been obtained when pyrolyzed under an air atmosphere. The yolk–shell formation mechanism is discussed thoroughly in section 3.2. Dextrin is likewise usually used in spray processes and results in dense microspheres, or microspheres containing empty rooms.[96–98,114] Jeon *et al.* synthesized MnS–C composite microspheres *via* the spray drying process using a precursor solution containing manganese nitrate and dextrin and a sub-

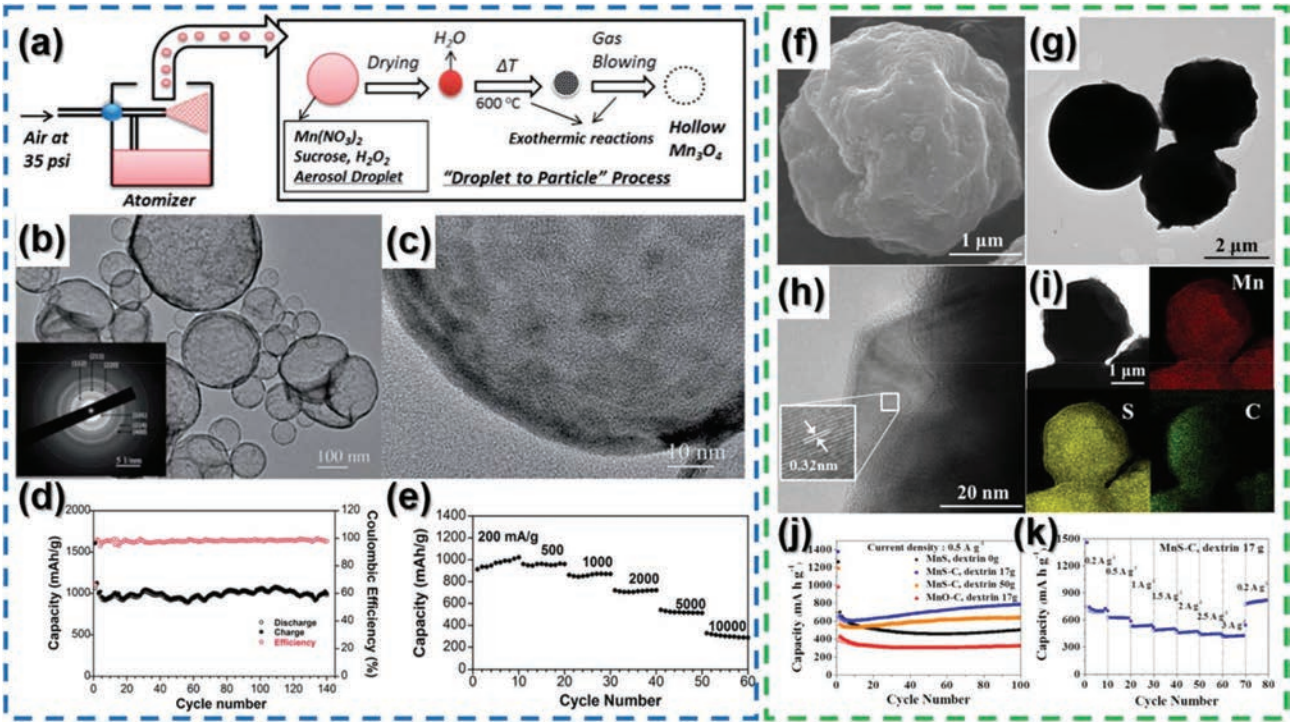

Fig. 2 (a) Schematic illustration of the synthetic process of hollow Mn_3O_4 spheres, (b) TEM and SAED images of the as-collected hollow Mn_3O_4 spheres, (c) HRTEM image of the microspheres, (d) cycling performance at 0.2 A g^{-1}, and (e) rate performance. Reproduced with permission from ref. 113. Copyright 2014, The Royal Society of Chemistry. Morphologies and elemental mapping images of the MnS–C powders prepared from spray drying and sulfidation heat treatment: (f) high resolution SEM image, (g) low and (h) high resolution TEM images, and (i) elemental dot mapping images. (j) Cycling and (k) rate performances of MnS–C microspheres. Reproduced with permission from ref. 97. Copyright 2015, Elsevier.

sequent sulfidation process.[97] The microspheres exhibited dense morphology (Fig. 2f–i), and a discharge capacity of 786 mA h g^{-1} could be achieved after the 100th cycle at 0.5 A g^{-1} (Fig. 2j). When cycled at 3 A g^{-1}, the microspheres exhibited a discharge capacity of 423 mA h g^{-1} (Fig. 2k). It was discovered that dextrin and metal salts can be phase separated, resulting in numerous empty rooms inside the microspheres, which is discussed in detail later in this paper.[117] The use of PVP results in the formation of a debossed structure, which is attributed to the melting point differences between the metal salts and PVP.[115,116] In particular, the migration of PVP to the surface due to phase segregation results in the formation of the debossed structure.[115,116] Hong *et al.* prepared double-shelled CuO yolk–shell powders from a spray solution containing Cu nitrate and PVP at 300 °C with subsequent post-treatment (Fig. 3a).[118] The surface of the synthesized yolk–shell microspheres exhibits debossed morphology due to the presence of PVP in the spray solution (Fig. 3b–d). The yolk–shell structured CuO microspheres exhibited a discharge capacity of 726 mA h g^{-1} after 500 cycles at 0.5 A g^{-1}, with a rate performance of 470 mA h g^{-1} at 2.5 A g^{-1} (Fig. 3e and f).

Dense spherical microspheres are ideal for energy storage materials due to the high tap density, which leads to a high energy density when employed as the electrode in rechargeable batteries. The study by Ju *et al.* on the synthesis of Li $(Ni_{1/3}Co_{1/3}Mn_{1/3})O_2$ microspheres revealed that the addition of a polymer precursor and drying control chemical additives (DCCAs) resulted in a less hollow particle compared with the microspheres prepared from a solution without them (Fig. 3g–j).[119] DCCAs are used in spray processes for controlling the drying rate of the atomized droplets to obtain microspheres with desired porosity/hollowness and dense microspheres.[119–125] Partial volume precipitation and gel formation occur due to the presence of a polymer precursor, if the suitable amount and ratio of the additives are achieved.[119–124,126–135] The combination of citric acid and ethylene glycol is employed since the hydroxyl group in ethylene glycol and carboxyl group in citric acid trigger the esterification reaction inside the atomized droplets and yield organic polymers, leading to volume precipitation inside the droplets.[135,136] Nickel nitrate, cobalt nitrate, manganese acetate, DCCA, citric acid, and ethylene glycol were added to the spray solution, and the atomized droplets were spray-pyrolyzed at 900 °C, resulting in the formation of dense Li $(Ni_{1/3}Co_{1/3}Mn_{1/3})O_2$ microspheres (Fig. 3i and j).[119] When applied as the cathode for LIBs, the microspheres exhibit a discharge capacity of 154 mA h g^{-1} after 30 cycles and at 0.5C (Fig. 3k).

3.2 Homogeneous yolk–shell microspheres

Represented by the core@void@shell configuration, the yolk–shell structure has attracted tremendous interest in various

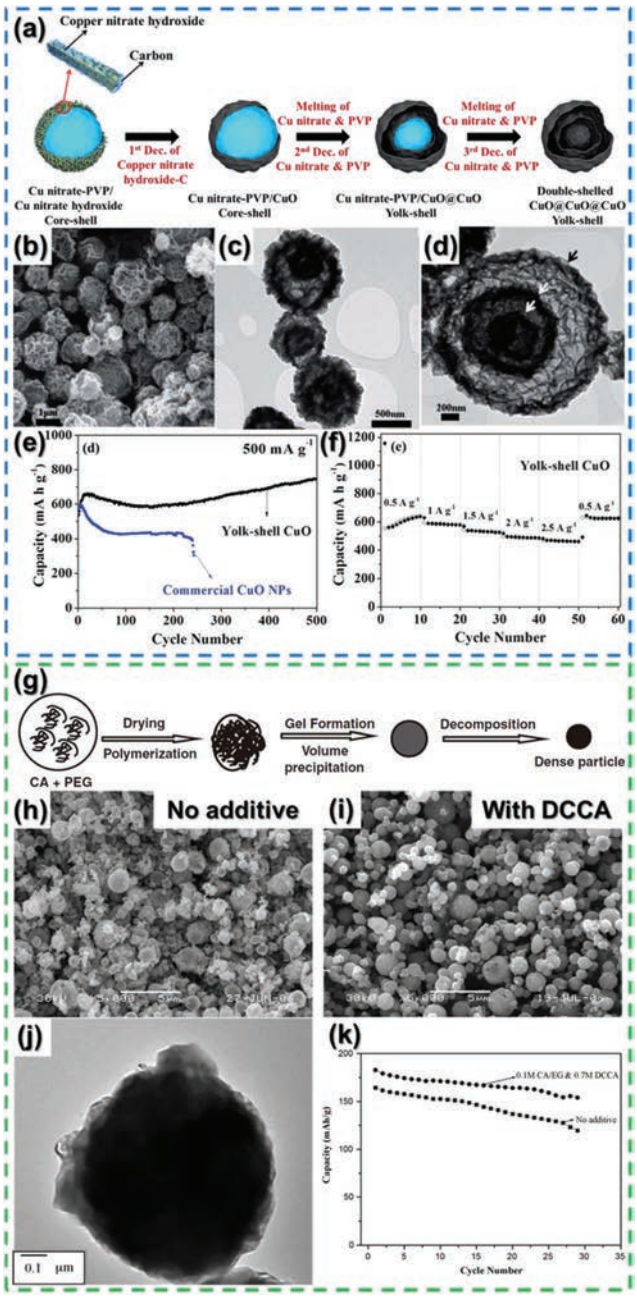

Fig. 3 (a) Schematic illustration of the synthetic process of CuO yolk–shell powder, (b) SEM image, (c and d) TEM images, (e) cycling performance at 0.5 A g^{-1}, and (f) rate performance of CuO yolk–shell microspheres. Reproduced with permission from ref. 118. Copyright 2014, The Royal Society of Chemistry. (g) Schematic illustration of the synthetic process of dense particle formation in spray pyrolysis. SEM images of the $Li(Ni_{1/3}Co_{1/3}Mn_{1/3})O_2$ cathode powder prepared (h) without and (i) with DCCA, (j) TEM image of the dense $Li(Ni_{1/3}Co_{1/3}Mn_{1/3})O_2$ cathode powder, and (k) cycling performances of $Li(Ni_{1/3}Co_{1/3}Mn_{1/3})O_2$ prepared from spray solutions with and without additives. Reproduced with permission from ref. 119. Copyright 2008, Elsevier.

research fields, such as energy storage, gas sensing, catalysis, photoluminescence, and drug delivery.[137–142] When such a design is applied to the anode materials of LIBs or SIBs, the void between the core and shell can serve as an efficient buffering space to accommodate the stress from the volume change during the (dis)charge processes. This void space also provides a shortened diffusion length and increased contact area between the active sites and the electrolyte, facilitating the overall electrochemical processes. Therefore, yolk–shell structured powders exhibit outstanding cycling and rate performances without compromising the energy density to a significant extent by increasing the fraction of the electrochemically active component.[143–145] A conventional method for synthesizing yolk–shell structured materials relies on the selective etching of templates between the core and shell materials, which is a time-consuming and multistep method that lacks scalability.[146–149] Since the pioneering work carried out by Kang's group in 2013,[150] spray pyrolysis and spray drying have been the major protocols to synthesize yolk–shell structured materials as they are rapid, continuous, straightforward, and scalable processes. Kang's group suggested that the repeated combustion and contraction of the carbon–metal precursor composite by ignition during spray pyrolysis is key to the formation of the yolk–shell structure. In their first study, the droplet containing tin oxalate and sucrose dried and decomposed to form a C–SnO_2 intermediate, followed by immediate combustion of the surface for instantaneous formation of the highly crystalline SnO_2 shell with a C–SnO_2 core (Fig. 4a).[150] The C–SnO_2 core did not undergo combustion immediately, because the oxygen supply to the inside of the SnO_2 shell was insufficient. The combustion reinitiated after the contraction of the core generated the void in between the shell and core that allowed the infusion of oxygen. The repeated combustion and contraction produced the double-shelled SnO_2 yolk–shell, as shown in SEM and TEM images in Fig. 4b–e. When tested as the anode material for LIBs, yolk–shell structured SnO_2 exhibited a discharge capacity of 642 mA h g^{-1} after the 40th cycle at 625 mA g^{-1} (Fig. 4f).

More intensive mechanistic research regarding the formation and features of the yolk–shell structure synthesized by spray processes was conducted by several follow-up studies. For successful formation of the yolk–shell structure, the metal salts and carbon precursors should be compatible in a way that the droplets containing them produce a dense intermediate after drying before they undergo combustion. Choi *et al.* reported the kilogram-scale production of the SnO_2 yolk–shell powder by the pilot-scale spray drying process.[151] In this work, the authors used different carbon sources to investigate their influence on the final morphologies of the powders. Citric acid and PVP were not compatible with Sn oxalate, as they formed hollow and deformed composites after spray drying. A sucrose-containing solution formed dense particles; however, these aggregated shortly after spray drying due to the deliquescing of sucrose. Dextrin with low deliquescence was found to be the best carbon source, since it formed a spherical and dense composite with Sn oxalate and played a role of an effective drying agent. Among various carbon sources–Sn composites, only the Sn oxalate–dextrin composite produced the yolk–shell structured SnO_2 powder after oxidation. When used

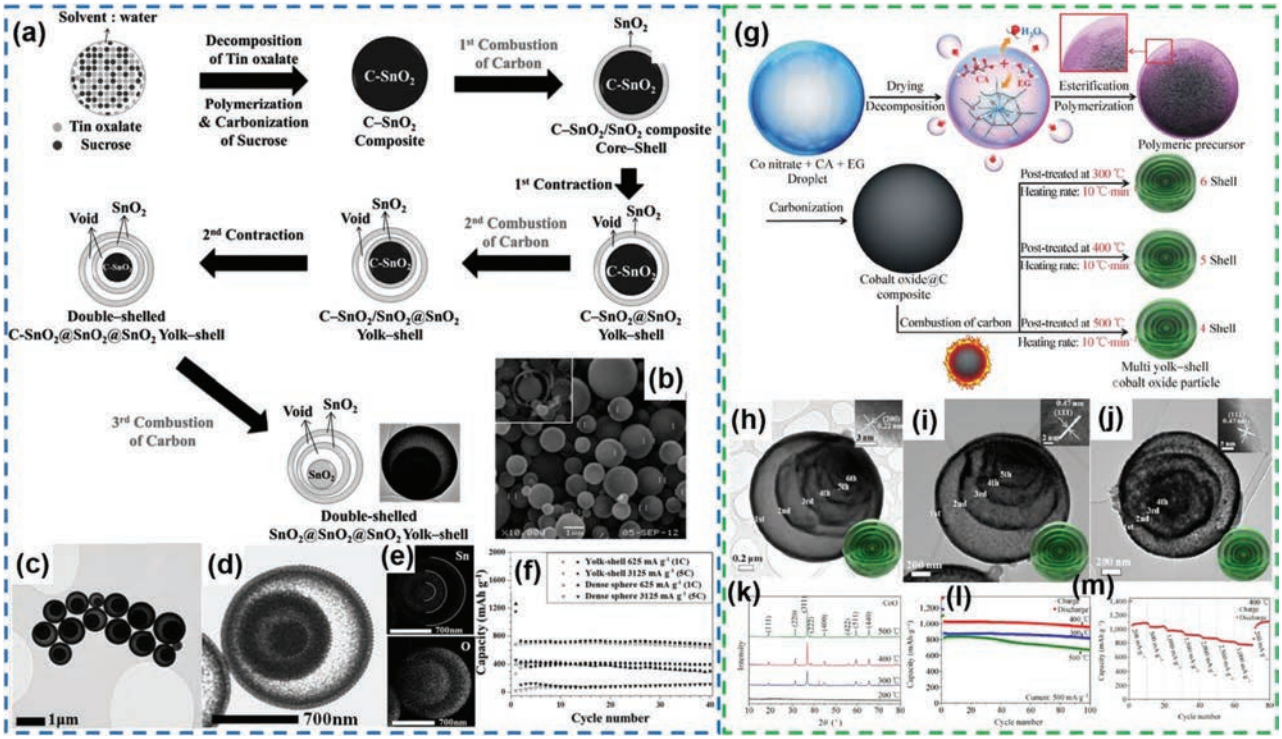

Fig. 4 (a) Schematic illustration of the synthetic process of the double-shelled SnO_2 yolk–shell-structured powder. (b) SEM image, (c) TEM image, (d) magnified TEM image, (e) elemental dot mapping images of SnO_2 yolk–shell microspheres and (f) their cycling performances. Reproduced with permission from ref. 150. Copyright 2013, Wiley-VCH. (g) Schematic illustration of the synthetic process of the yolk–shell powder employing polymeric precursors. TEM images of the cobalt oxide powders post-treated at (h) 300 °C, (i) 400 °C, and (j) 500 °C with 6, 5, and 4 shells, respectively. (k) XRD patterns, (l) cycling and (m) rate performances of yolk–shell microspheres. Reproduced with permission from ref. 136. Copyright 2014, Springer Nature.

as the anode for LIBs, the powder exhibited a stable discharge capacity of 570 mA h g^{-1} after the 100th cycle at 2000 mA g^{-1}. The authors also investigated the effect of the ratio between the metal precursor and carbon source on the final morphology. The higher the concentration of Sn oxalate, the larger the core SnO_2, eventually resulting in a dense SnO_2 particle. This indicates that the appropriate ratio between the metal salts and carbon source is another critical design factor for yolk–shell structures. Sucrose, however, could act both as a carbon source and drying agent when forming a composite with Fe nitrate. Zhou *et al.* reported scalable synthesis of multi-shelled α-Fe_2O_3 yolk–shell powder by using a mini spray-dryer.[152] Sucrose acted as a matrix that dispersed Fe nitrate and mitigated its deliquescence. The void spaces and the permeable thin shells greatly shortened the distance for Li-ion diffusion and effectively alleviated the strain during cycling, such that yolk–shell structured α-Fe_2O_3 could achieve a high and stable capacity of ~900 mA h g^{-1} over 50 cycles at 1600 mA g^{-1}. The authors also tested glucose and polyvinyl alcohol as alternative carbon sources. Glucose was likewise capable of producing a yolk–shell structure, whereas polyvinyl alcohol produced a hollow structure, indicating the importance of the compatibility between the metal salt and carbon source. Moreover, as the relative amount of sucrose to Fe nitrate increased, the product became hollow after the post-treatment, which is in agreement with the previous discussion. Park *et al.* synthesized Co_3O_4 yolk–shell microspheres with a controllable number of shells by spray drying.[136] To optimize the synthesis conditions, the authors employed various carbon sources as drying additives. Sucrose, glucose, dextrin, PVP, and citric acid all failed to form a dense spherical composite with Co nitrate or mitigated the deliquescence of Co nitrate. To solve this problem, ethylene glycol was added into the spray solution containing Co nitrate and citric acid. During the spray drying process, the esterification reaction between the carboxyl group in citric acid and the hydroxyl group in ethylene glycol occurred inside the droplet to yield organic polymers with highly viscous gel consisting of a three-dimensional network of polymers, which enabled the formation of dense and spherical powder with low deliquescence (Fig. 4g). The number of shells was controlled by post-treatment at different temperatures with the same ramping rate of 10 °C min^{-1}. After oxidation at 300, 400, and 500 °C, Co_3O_4 yolk–shell powders with 6, 5, and 4 shells were obtained, respectively. Considering the successful formation of the yolk–shell structure at 300 °C, the powders oxidized at 400 °C and 500 °C would have initially formed 6-shelled yolk–shell structured Co_3O_4. As the temperature rose past 300 °C, the kinetics of the Ostwald ripening process was favored. Consequently, the oxidation at higher temperatures resulted in the crystal growth of the outer shells

at the expense of inner shells, as evidenced by XRD patterns with increasing sharpness (Fig. 4k) and TEM images with fewer number of shells (Fig. 4h–j). When evaluated as anode materials for LIBs, the sample post-treated at 400 °C exhibited the best performance, with a discharge capacity of 958 mA h g^{-1} after the 100th cycle at 500 mA g^{-1} and a rate performance of 770 mA h g^{-1} at 3000 mA g^{-1} (Fig. 4l and m).

However, recent reports from Kang's group suggest that the formation of dense intermediate particles does not always lead to the formation of yolk–shell structures.[117,153] Partially decomposed Co nitrate–dextrin composite particles with a dense structure were initially formed during the synthesis of multiroom-structured Co_3O_4–C microspheres by spray pyrolysis (the formation mechanism of the multiroom structure is discussed further in section 3.3.1) (Fig. 5a).[117] Upon washing and retrieval of this powder with distilled water, a number of irregularly shaped nanorooms were revealed inside the particles as a result of the elimination of undecomposed dextrin (Fig. 5b). This strongly implies a phase separation between Co nitrate and dextrin inside the dried particles. The report on the synthesis of multicomponent (Mo, Ni)-metal-based multiroom structured microspheres by Park *et al.* likewise presents a similar phenomenon,[153] and most importantly, it provides great insight into why the formation of a homogeneous metal precursor-carbon source intermediate is imperative to the formation of the yolk–shell structure during the spray processes. The spray-dried metal (Mo, Ni) salt–dextrin composite formed dense particles (Fig. 5c). Based on previous observations, the most likely result after the combustion of this dried precursor powder is yolk–shell structured $NiMoO_4$ powder. In contrast to expectations, however, the oxidation of the dried precursor at 500 °C resulted in the formation of multiroom-structured $NiMoO_4$, as shown in Fig. 5d. This strongly indicates that the nanorooms generated by the decomposition of dextrin ensured oxygen penetration that allowed the combustion to take place all over the particles, instead of the surface-confined combustion and subsequent core contraction to produce the yolk–shell structure.

Melting points of the target materials should also be taken into account when designing yolk–shell structures.[154,155] Ko *et al.* introduced the two-step process for fabrication of yolk–shell structured V_2O_5 powder (Fig. 6a).[154] In this case, one-pot synthesis of yolk–shell structured V_2O_5 at temperatures between 700 °C and 1000 °C could not be achieved. The initially formed yolk–shell V_2O_5 by combustion and contraction was subjected to immediate melting since the temperature of the reactor was much higher than the melting point of V_2O_5 (690 °C), resulting in the dense V_2O_5 sphere. To overcome this problem, the authors prepared V_2O_3–C composite precursor powder under an inert atmosphere and conducted post-

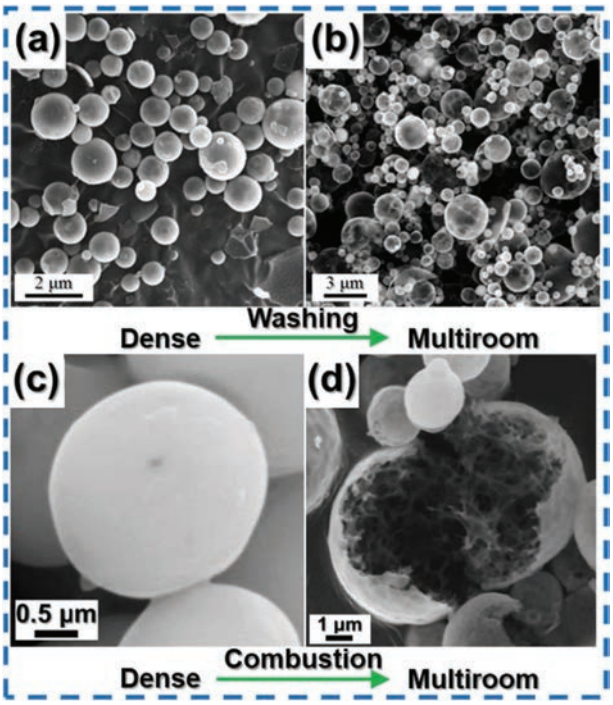

Fig. 5 SEM images of the cobalt oxide-dextrin composite microspheres prepared from the spray solution with dextrin: (a) as-prepared powder and (b) powder obtained after rinsing with distilled water. Reproduced with permission from ref. 117. Copyright 2016, Elsevier. SEM images of (c) spray-dried precursor microspheres containing dextrin and metal salts, and (d) metal oxide microspheres with empty nanorooms obtained by post-treatment under air. Reproduced with permission from ref. 153. Copyright 2017, The Royal Society of Chemistry.

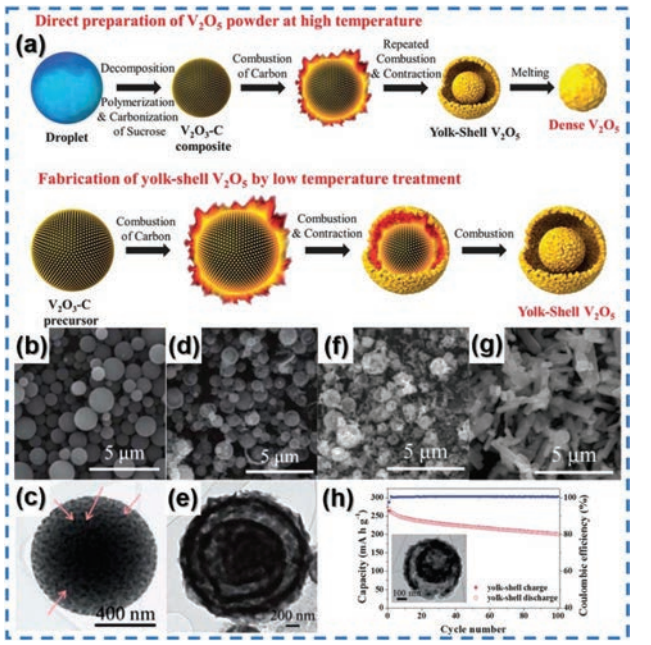

Fig. 6 (a) Schematic illustration of the synthetic process of dense and yolk–shell V_2O_5 microspheres. (b) SEM and (c) TEM images of the V_2O_3–C composite prepared by spray pyrolysis and (d) SEM and (e) TEM images of yolk–shell structured V_2O_5 microspheres. SEM images of spray-pyrolyzed powder combusted at (f) 500 °C and (g) 600 °C. (h) Cycling performance of yolk–shell structured V_2O_5 microspheres at 1 A g^{-1}. Reproduced with permission from ref. 154. Copyright 2013, The Royal Society of Chemistry.

treatment under an air atmosphere. The high preparation temperature (1000 °C) of vanadium oxide–carbon induced the carbothermal reduction of V_2O_5 to VO_x, which crystallized and successfully dispersed all over the carbon microsphere (Fig. 6b and c). Oxidation at 400 °C caused immediate combustion of VO_x–C from the surface, which produced core–shell structured VO_x–C@V_2O_5. Contraction of the VO_x–C core occurred during further heating, followed by a second step combustion of the core. After repeated combustion and contraction, multi-shelled V_2O_5 yolk–shell powder was successfully produced (Fig. 6d and e). Yolk–shell structured V_2O_5 exhibited a discharge capacity of 201 mA h g^{-1} after the 100th cycle at 1000 mA g^{-1}, when tested as the cathode material of LIBs (Fig. 6h). At higher combustion temperatures (500 °C and 600 °C), the severe crystal growth of V_2O_5 resulted in the destruction of yolk–shell morphologies (Fig. 6f and g). In a similar manner, the authors prepared yolk–shell structured MoO_3 microspheres.[155] MoO_3 has a low melting point (795 °C), which means that the one-pot synthesis of MoO_3 yolk–shell powder was not straightforward. Therefore, the MoO_x–C composite microspheres were prepared by spray pyrolysis at 900 °C under an inert atmosphere, and combusted at 400 °C to produce yolk–shell structured MoO_3. Combustion at 500 °C produced hollow structured MoO_3 as a result of the Ostwald ripening process that induced the thickening of shell MoO_3 at the expense of yolk MoO_3.

In an effort to reveal the influence of burning on the formation of a yolk–shell structure, Kang's group conducted a further in-depth study in 2017 using a metal precursor containing carbonaceous template microspheres (Fig. 7).[156] They systematically investigated the effects of the ramping rate and oxygen concentration on the morphologies and crystallite sizes of the metal oxide microspheres after post-treatment of the carbonaceous template microspheres loaded with a controlled amount of a metal precursor (Fig. 7a). In the case of carbon template microspheres with a low loading rate of the metal precursor, oxidation at 500 °C at a high oxygen concentration with a high ramping rate led to the combustion of the outer surface of the microsphere, which generated a large amount of heat that caused contraction of the core, followed by repeated combustion and contraction to produce the yolk–shell metal oxide microsphere (Fig. 7b–d). In contrast, when the oxidation process was conducted at a low oxygen concentration with a low ramping rate, inward contraction of the molten metal precursor within the carbon template occurred to produce the C–metal precursor@C core–shell intermediate. Because of the low ramping rate and oxygen concentration, decomposition of the carbon and metal precursor proceeded gradually without combustion by ignition, resulting in the filled structured metal oxide microsphere (Fig. 7e–g). As burning of the microsphere did not occur for filled structured metal oxide, its crystallite size was smaller than the yolk–shell structured metal oxide, as indicated in Fig. 7b and f. The loading rate of the metal precursor was another factor that determined the morphology. Despite burning at a high ramping rate, contraction of the microsphere did not occur when the loading rate of the metal precursor was high, producing a filled structured metal oxide microsphere with a large crystallite size. In summary, regardless of the synthetic process, formation of a yolk–shell structure should be accompanied by combustion, which involves the sudden increase of the temperature by ignition, and subsequent contraction.

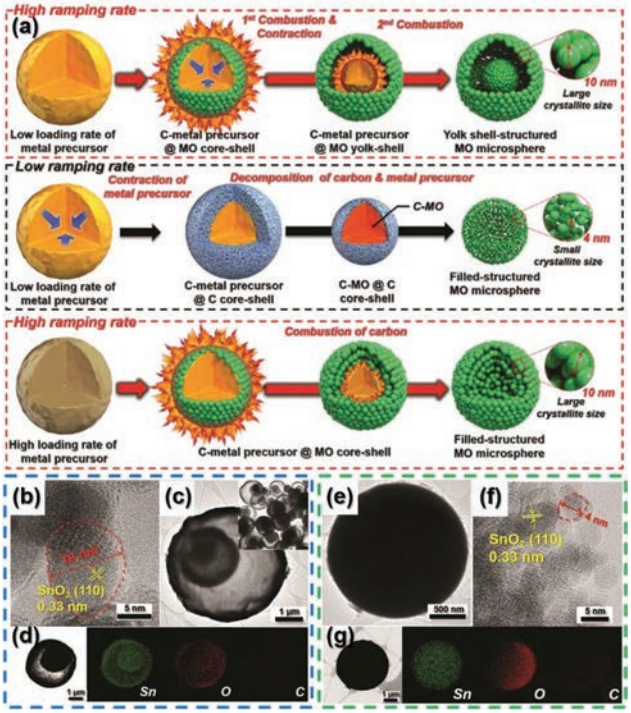

Fig. 7 (a) Schematic illustration of the synthetic process of Y-SnO_2-LC, F-SnO_2-SC, and F-SnO_2-LC from the carbonaceous template microspheres loaded with a controlled amount of metal precursor. (b) TEM image, (c) HR-TEM image, and (d) elemental dot mapping images of yolk–shell structured microspheres prepared under the conditions of low metal loading, high ramping rate, and high oxygen concentration. (e) TEM image, (f) HR-TEM image, and (g) elemental dot mapping of filled microspheres prepared under the conditions of low metal loading, low ramping rate, and low oxygen concentration. Reproduced with permission from ref. 156. Copyright 2017, The Royal Society of Chemistry.

The feasibility and versatility of the spray processes for the synthesis of various yolk–shell structured materials have been confirmed by a series of studies on other yolk–shell structured metal oxides, *e.g.* Co_3O_4, CuO, Fe_2O_3, V_2O_5, WO_3, *etc.*[118,157–163] Hong *et al.* demonstrated that yolk–shell powder with a quinary composition can be easily prepared by simple dissolution of metal salts in the precursor solution (Fig. 8a).[162] Using the same method, Choi *et al.* synthesized multicomponent yolk–shell structured powder containing ten transition metals, as shown in Fig. 8b.[163] Both studies pinpointed the advantage of the spray process for the synthesis of a yolk–shell structured material with a desired composition. For the high-performance anode in LIBs, various yolk–shell structured multicomponent metal oxide materials have been widely reported.[164–171] For instance, Leng *et al.* synthesized the hierarchical $NiCo_2O_4$ multishell yolk–shell structure.[170] The number of shells was controlled by the amount of PVP, which

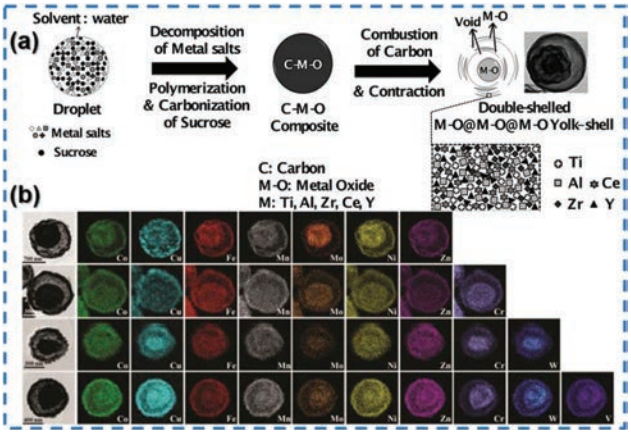

Fig. 8 (a) Schematic illustration of the synthetic process of yolk–shell composite powder with a quinary composition and (b) elemental mapping images of the yolk–shell transition metal oxide microspheres with 7 to 10 components. Reproduced with permission from ref. 162. Copyright 2013, Wiley-VCH. Reproduced with permission from ref. 163. Copyright 2014, The Royal Society of Chemistry.

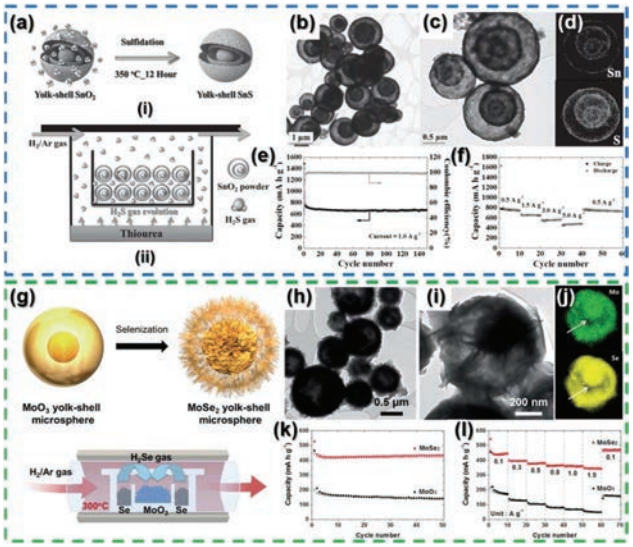

Fig. 9 (a) Schematic illustration of the synthetic process of the yolk–shell SnS microspheres from yolk–shell SnO_2 microspheres by the sulfidation process. (b and c) TEM images and (d) elemental dot mapping images of yolk–shell SnS microspheres and their (e) cycling and (f) rate performances. Reproduced with permission from ref. 172. Copyright 2013, Wiley-VCH. (g) Schematic illustration of the synthetic process of yolk–shell-structured $MoSe_2$ microspheres by the selenization process. (h) TEM image, (i) magnified TEM image, and (j) elemental dot mapping images of $MoSe_2$ yolk–shell microspheres. (k) Cycling performance of $MoSe_2$ yolk–shell powder at 0.2 A g^{-1} and (l) rate performance. Reproduced with permission from ref. 173. Copyright 2014, The Royal Society of Chemistry.

was used as a surfactant and a carbon template. When compared with the hollow $NiCo_2O_4$, multishell yolk–shell, $NiCo_2O_4$ exhibited better cycling (1144 mA h g^{-1} after 75 cycles at 400 mA g^{-1}) and rate performance (821 mA h g^{-1} at 2000 mA g^{-1}), mainly owing to the functional shells and core that guaranteed a large contact area between the electrode and the electrolyte, providing more active sites for Li. Ahn *et al.* prepared a β-$NiMoO_4$ yolk–shell by one-pot spray pyrolysis.[171] The morphologies of the samples varied depending on the synthesis temperature. At 600 °C, carbon combustion was incomplete, thus dense and amorphous $NiMoO_4$–C composite microspheres were obtained. At 800 °C and 1000 °C, carbon combustion was successfully performed to produce yolk–shell morphologies, with $NiMoO_4$ nanorod aggregation at the shell and core, by crystal growth in the sample prepared at 1000 °C. The sample prepared at 800 °C exhibited the best cycling performance due to its structural stability, maintaining the reversible capacity of 842 mA h g^{-1} after 200 cycles. Even at a high current density of 5 A g^{-1}, this sample exhibited a discharge capacity of 612 mA h g^{-1}, demonstrating excellent rate performance. Metal sulfides and selenides could also be prepared by post-treatment of the yolk–shell structured oxide precursors.[172–175] For example, Choi *et al.* prepared yolk–shell structured SnS microspheres by sulfidation of a SnO_2 precursor. H_2S gas generated from the decomposition of thiourea under a reducing atmosphere transformed SnO_2 into SnS, as shown in the scheme of Fig. 9a(i–ii).[172] The morphology of yolk–shell structured SnS was well maintained even after the sulfidation process (Fig. 9b–d). Owing to its unique morphology, the SnS yolk–shell powder showed superior Li-ion storage properties, achieving a high capacity retention of 89% after 150 cycles and delivering a discharge capacity of 480 mA h g^{-1} at a high current density of 5 A g^{-1} (Fig. 9e and f). Ko *et al.* reported the synthesis of $MoSe_2$ yolk–shell microspheres by selenization of a MoO_3 precursor.[173] In this case, selenium powder was used to produce H_2Se gas to transform MoO_3 into $MoSe_2$ (Fig. 9g). Due to the characteristic crystal growth behavior of $MoSe_2$, a microsphere comprised of $MoSe_2$ nanosheets in yolk–shell assembly was formed, as shown in Fig. 9h–j. When tested as the anode material for SIBs, $MoSe_2$ yolk–shell powder exhibited superior electrochemical properties in terms of reversible capacity (433 mA h g^{-1} after the 50th cycle at 0.2 A g^{-1}) and rate performance (345 mA h g^{-1} at 1.5 A g^{-1}), as shown in Fig. 9k and l. Employment of the yolk–shell structure in the cathode materials of LIBs was likewise reported.[176–180] Sim *et al.* synthesized yolk–shell structured $LiMnO_4$ by one-pot spray pyrolysis.[179] This material exhibited an outstanding rate capability of 116 mA h g^{-1} at 10C rate. Choi *et al.* reported single and double-shelled $LiNi_{0.5}Mn_{1.5}O_4$ yolk–shell powder, which could deliver 108 mA h g^{-1} after the 1000th cycle at 10C rate.[180] The electrochemical properties of the yolk–shell structured materials are summarized in Table 1.

3.3 Phase separation

3.3.1 Multiroom structure. In 2016, Kang's group reported for the first time the synthesis of multiroom-structured metal compound-carbon microspheres by spray pyrolysis.[117] The most remarkable feature of this novel structure is that the empty rooms (voids) inside the microsphere were not generated by wet etching of the template material, which is the most

Table 1 Morphologies and electrochemical performances of various yolk–shell structured materials synthesized *via* spray processes

Sample	Voltage window/ application	Synthesis method	Cycling performance[a]	Rate performance[b]	Ref.
3.2 Yolk–shell microspheres					
Double-shelled SnO_2 yolk–shell microspheres	~0.01–3.0 LIB anode	Spray pyrolysis	642/40th/0.625	—	150
SnO_2 yolk–shell powder	0.001–1.0 LIB anode	Spray drying	570/100th/2.0	518/5.0	151
α-Fe_2O_3 multi-shelled hollow spheres	~0.01–3.0 LIB anode	Spray drying	~1035/50th/0.4	784/3.2	152
Yolk–shell V_2O_5 powders	2.0–4.0 LIB cathode	Spray pyrolysis	201/150th/1.0	185/1.0	154
Yolk–shell MoO_3 powders	0.001–3.0 LIB anode	Spray pyrolysis	835/150th/1.0	534/5.0	155
Co_3O_4 yolk–shell powders	0.01–3.0 LIB anode	Spray pyrolysis	603/50th/1.0	548/10.0	157
Double shelled Fe_2O_3 yolk–shell	0.005–3.0 LIB anode	Spray pyrolysis	848/80th/0.3	746/5.0	158
Yolk–shell FeO_x filled with N-doped graphitic C	0.01–3.0 LIB anode	Spray pyrolysis	1071/1000th/1.0	598/10.0	159
Yolk–Shell NiO nanopowders	0.001–3.0 LIB anode	Spray pyrolysis	951/150th/0.7	824/1.0	160
Yolk–shell WO_3 particles	0.01–3.0 LIB anode	Spray pyrolysis	523/120th/0.3	—	161
Yolk–shell microspheres with 8 components	~0.01–3.0 LIB anode	Spray pyrolysis	~1067/700th/1.0	473/5.0	163
Yolk–shell $CoFe_2O_4$ powders	0.001–3.0 LIB anode	Spray pyrolysis	751/200th/1.0	681/5.0	164
Yolk–shell $CoMn_2O_4$ powders	0.01–3.0 LIB anode	Spray pyrolysis	418/40th/0.8	—	165
Yolk–shell $CoMoO_4$ particles	0.001–3.0 LIB anode	Spray pyrolysis	1065/150th/0.5	783/1.5	166
Yolk–shell $ZnCo_2O_4$ powders	0.001–3.0 LIB anode	Spray pyrolysis	753/200th/3.0	640/10.0	167
Yolk–shell CuO-Fe_2O_3 powders	0.001–3.0 LIB anode	Spray pyrolysis	1159/130th/1.0	735/5.0	168
Yolk–shell ZnO–Mn_3O_4 powders	0.001–3.0 LIB anode	Spray pyrolysis	912/100th/0.7	460/3.0	169
Hierarchical Ni–Co oxide multishell yolk–shell	0.01–3.0 LIB anode	Spray pyrolysis	1064/100th/0.4	821/2.0	170
β-$NiMoO_4$ yolk–shell spheres	0.001–3.0 LIB anode	Spray pyrolysis	1292/200th/1.0	612/5.0	171
Yolk–shell SnS powders	0.001–1.0 LIB anode	Spray pyrolysis	672/150th/1.0	480/5.0	172
Hierarchical $MoSe_2$ yolk–shell microspheres	0.001–3.0 SIB anode	Spray pyrolysis	433/50th/0.2	345/1.5	173
Yolk–shell structured $(Fe_{0.5}Ni_{0.5})_9S_8$ powders	0.01–3.0 SIB anode	Spray pyrolysis	527/100th/1.0	465/5.0	174
Yolk–shell SnS–MoS_2 powders	0.001–2.5 SIB anode	Spray pyrolysis	396/100th/0.5	238/7.0	175
Yolk–shell $Li_4Ti_5O_{12}$ powders	1.0–3.0 LIB anode	Spray pyrolysis	172/100th/0.175	—	176
Yolk–shell LiV_3O_8 powder	2.0–4.0 LIB cathode	Spray pyrolysis	192/100th/1.0	232/0.8	177
Yolk–shell $0.6Li(Li_{1/3}Mn_{2/3}O)_2{\cdot}0.4Li(Ni_{1/3}Co_{1/3}Mn_{1/3})O_2$	2.0–4.8 LIB cathode	Spray pyrolysis	194/50th/0.02	—	178
Yolk–shell $LiMn_2O_4$ powders	3.5–4.3 LIB cathode	Spray pyrolysis	127/200th/0.36	—	179
Yolk–shell $LiNi_{0.5}Mn_{1.5}O_4$ powders	3.5–5.0 LIB cathode	Spray pyrolysis	108/1000th/1.48	69/88.8	180
Double-shelled CuO yolk–shell powders	0.01–3.0 LIB anode	Spray pyrolysis	726/500th/0.5	470/2.5	118
Multi-shelled yolk–shell Co_3O_4 powders	0.001–3.0 LIB anode	Spray drying	958/100th/0.5	770/3.0	136

[a] These data were arranged in the order discharge capacity/cycle number/current density. The units of discharge capacity and current density are mA h g^{-1} and A g^{-1}, respectively. [b] These data were arranged in the order discharge capacity/highest current density.

common strategy to introduce the pore structure. Kang's group found that the liquid–liquid phase separation during the spray pyrolysis process is key to generating a multiroom structure. As discussed in section 3.2, compatibility between the metal salt and carbon source is an important factor that determines the final morphology of the product. Spray pyrolysis of the solution containing a metal salt and dextrin produced a molten composite precursor intermediate sphere, in which the liquid–liquid phase separation resulted in an inhomogeneous distribution of the metal salt and dextrin. Since the retention time of the droplet was short due to the high flow rate (25 L min^{-1}), the homogeneous mixing of the segregated chemical species would not be able to take place. Subsequent carbonization of dextrin and decomposition of the metal salt under a N_2 atmosphere *via* the evolution of a large amount of gas generated the multiroom-structured metal oxide–carbon microspheres. Previous studies suggest that the carbon microsphere cannot be produced by spray pyrolysis of the solution containing only the carbon source, even at the prolonged retention time of the droplet or higher reaction temperature.[181–184] Therefore, metal salts that can catalyze the carbonization reaction should be added to promote the formation of carbon.[183,184] Considering such characteristics of spray pyrolysis, the formation of nanorooms inside the microsphere can be regarded as a result of the decomposition of phase-separated dextrin into gas, which could not be carbonized owing to the absence of metal salts in the vicinity. Kim *et al.* synthesized Co and Mo-based multiroom-structured microspheres by spray pyrolysis at 400 °C (Fig. 10a).[185] Although the as-prepared powder had a multiroom morphology, it nevertheless contained a considerable amount of incompletely decomposed metal salts and dextrin, since the flow rate of N_2 gas during the synthesis was extremely high (40 L min^{-1}) (Fig. 10b). The oxidation of the as-prepared powder at 400 °C to produce multiroom-structured $CoMoO_4$ microspheres provided compelling evidence of the localized phase separation of dextrin along the microsphere, which the authors denoted as the formation of "dextrin islands". If the metal salts and dextrin formed a homogeneous composite throughout the wall of the microsphere, post-treatment under an air atmosphere (and thus combustion) would have resulted in the collapse and shrinkage of the internal framework, leading to the formation of hollow-structured or yolk–shell

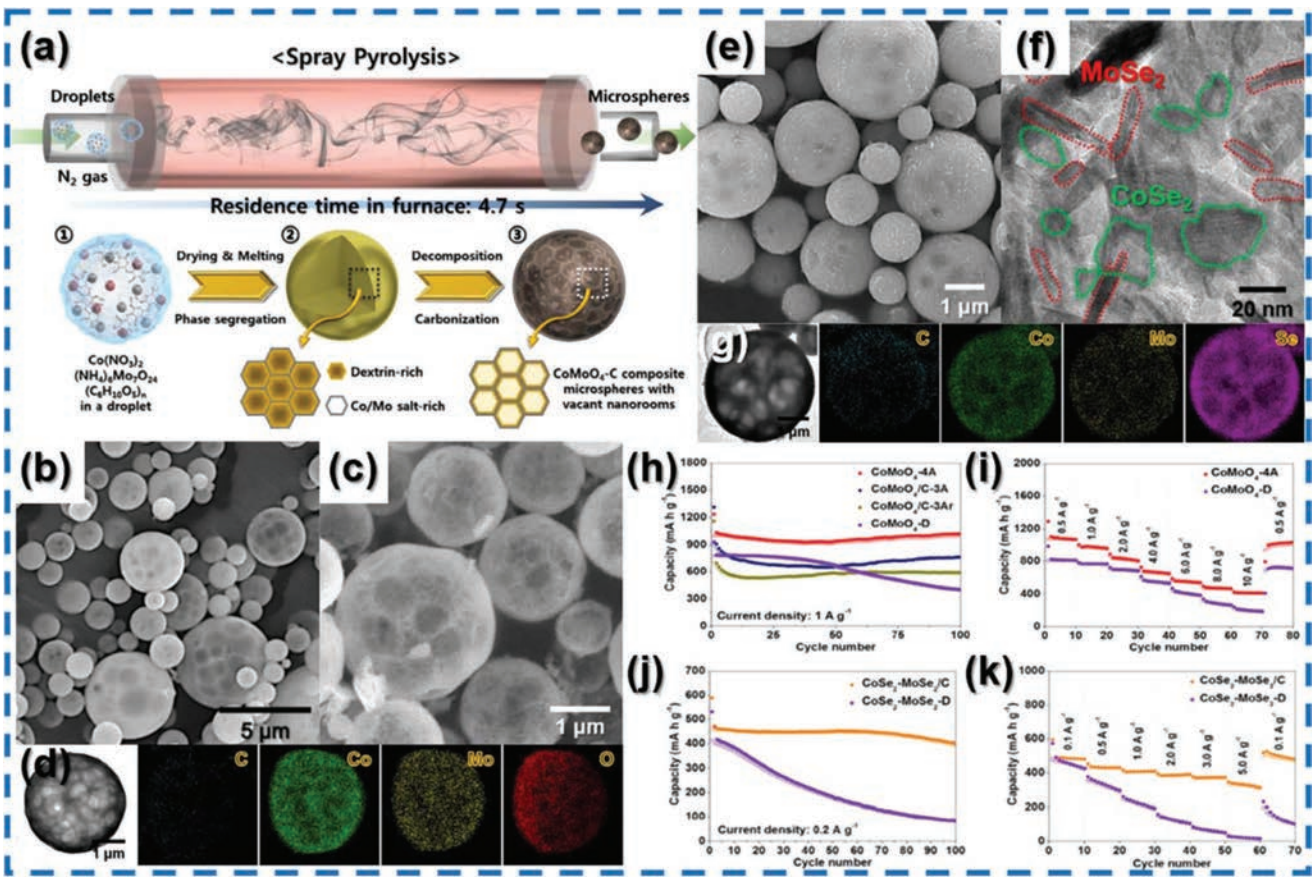

Fig. 10 (a) Schematic illustration of the synthetic process of $CoMoO_4$–carbon composite microspheres containing abundant vacant nanorooms by the spray pyrolysis process. (b) SEM image of the as-prepared $CoMoO_4$–C composite microspheres with vacant nanorooms, (c) SEM image and (d) elemental dot mapping images of the obtained nanopores after post-treatment at 400 °C under air. (e) SEM image, (f) HR-TEM image, and (g) elemental dot mapping images of $CoSe_2$–$MoSe_2$/C microspheres. (h–k) Li-Ion and Na-ion storage characteristics of the synthesized microspheres. Reproduced with permission from ref. 185. Copyright 2017, Elsevier.

structured microspheres. However, oxidation of the as-prepared powder did not bring about such outcomes. Instead, the formation of new nanopores along the internal framework of $CoMoO_4$ was observed (Fig. 10c and d). These nanopores were likely to be generated by the decomposition of dextrin-derived carbon, verifying the inhomogeneous distribution of dextrin along the microsphere. The introduction of nanorooms improved the structural stability of the microspheres and enabled the facile diffusion of Li-ions. Therefore, multiroom-structured $CoMoO_4$ microspheres delivered a stable discharge capacity of 1023 mA h g^{-1} after the 100th cycle at 1 A g^{-1}, and a superior rate performance of 409 mA h g^{-1} at 10 A g^{-1} (Fig. 10h and i). Even after selenization to form the multi-room-structured $CoSe_2$–$MoSe_2$/C microsphere, such structural merits were preserved (Fig. 10e and f), ensuring the stable discharge capacity of 399 mA h g^{-1} after the 100th cycle at 0.2 A g^{-1} and the rate performance of 317 mA h g^{-1} at 5.0 A g^{-1}, when employed as the anode material for SIBs (Fig. 10j and k).

Park *et al.* synthesized multiroom-structured multicomponent (Mo, Ni) metal sulfide and selenide as anode materials for SIBs by spray drying (Fig. 11a).[153] As in the case of spray pyrolysis, spray drying of the solution containing dextrin and Ni/Mo salts produced their composite, where dextrin is locally phase-separated from the metal salts. Calcination and subsequent sulfidation or selenization produced multiroom-structured Ni/Mo sulfide and selenide composites (Fig. 11b–d). When the calcination step was conducted in air to remove carbon, subsequent sulfidation or selenization induced the crystal growth of Ni/Mo sulfides and selenides (Fig. 11e–g). Carbon-free MoS_2–Ni_9S_8 and $MoSe_2$–NiSe–$NiSe_2$ microspheres suffered from cycling fading (Fig. 11h and j). In contrast, those with carbon exhibited stable cycling performances, demonstrating the improved structural stability by introduction of carbon. The discharge capacities of MoS_2–Ni_9S_8–C and $MoSe_2$–NiSe–C after the 80th cycle were 366 mA h g^{-1} and 386 mA h g^{-1} at 0.5 A g^{-1} with decent rate performances at 3 A g^{-1}, respectively (Fig. 11h–k). Furthermore, the synthesis of multi-room structured $NiMoO_4$ and $Ni_3V_2O_8$ has also been reported, both of which demonstrated promising electrochemical performances as anode materials for LIBs.[98,114]

3.3.2 Core–shell structure. Similar to the yolk–shell structures, core–shell structures have a core@shell configuration that consists of the inner core and outer shell. Unlike yolk–shell structures, the core and shell of core–shell structures are in intimate contact without a void space between them. For energy storage application, core–shell structured materials can improve the electrical conductivity or provide structural robustness to the active material. In addition, core–shell materials ensure high tap density and do not degrade the volumetric energy density, which is often pointed out as a drawback of hollow materials. Recently, spray processes have been introduced to synthesize a number of core–shell materials. The

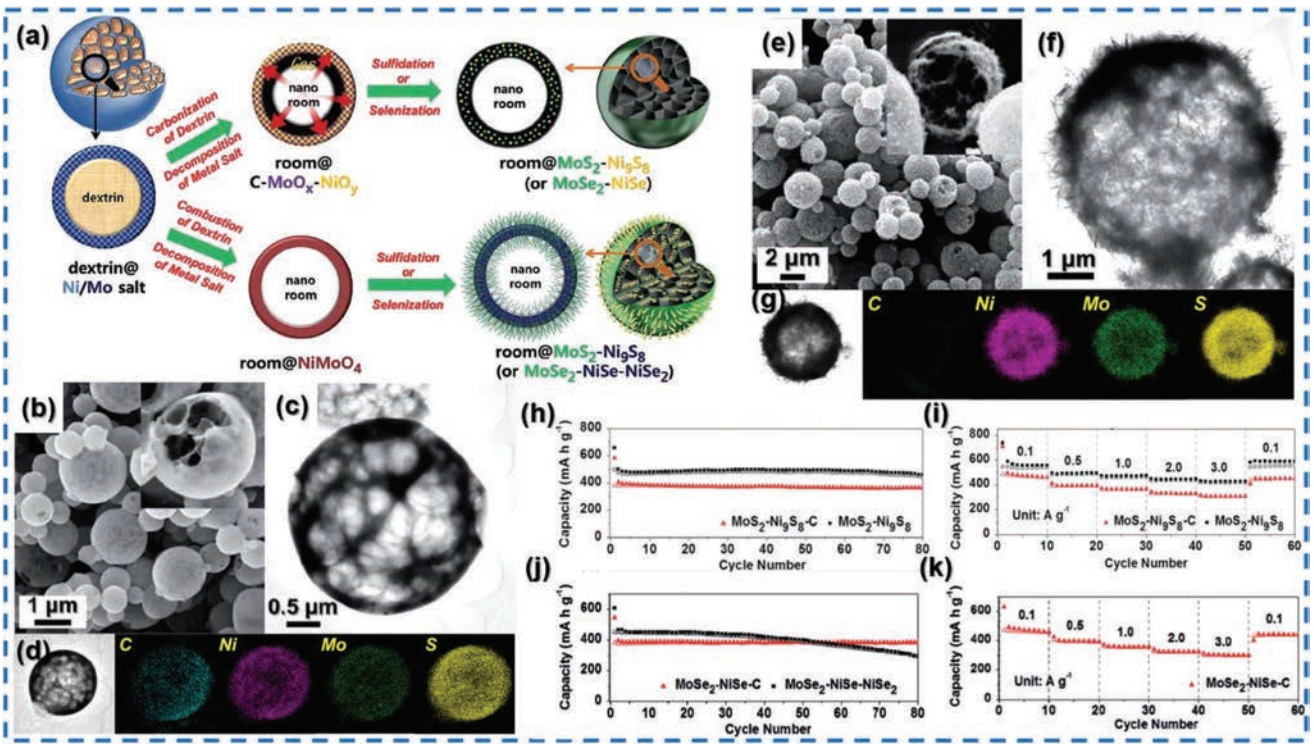

Fig. 11 (a) Schematic illustration of the synthetic process of empty nanorooms in the MoS_2–Ni_9S_8–C, $MoSe_2$–NiSe–C, MoS_2–Ni_9S_8, and $MoSe_2$–NiSe–$NiSe_2$ microspheres. (b) SEM image, (c) TEM image, (d) elemental dot mapping images of MoS_2–Ni_9S_8–C microspheres, (e) SEM image, (f) TEM image, and (g) elemental dot mapping images of MoS_2–Ni_9S_8, microspheres. (h–k) cycling and rate performances of MoS_2–Ni_9S_8–C, $MoSe_2$–NiSe–C, MoS_2–Ni_9S_8, and $MoSe_2$–NiSe–$NiSe_2$ microspheres. Reproduced with permission from ref. 153. Copyright 2017, The Royal Society of Chemistry.

most distinguishing feature of the reported studies is that the spontaneous separation of core and shell materials was achieved by delicate control of the process parameters. Hong *et al.* reported the one-pot synthesis of a core–shell structured SnO_x–C composite by spray pyrolysis (Fig. 12a).[186] Melting and phase separation of PVP in the dried droplet containing Sn oxalate and PVP took place at around 180 °C, which resulted in the migration of PVP to the outside of the dried particle. The subsequent carbonization of PVP and decomposition of Sn oxalate produced the core–shell structured SnO_x–C composite microsphere, as demonstrated in Fig. 12b–h. Compared with the dense SnO_2 microsphere, the core–shell structured SnO_x–C microsphere could effectively withstand the volume change during cycling. Therefore, core–shell structured SnO_x–C exhibited a stable discharge capacity of 1033 mA h g^{-1} after 500 cycles at a high current density of 2 A g^{-1} (Fig. 12i). Even at a higher current density (3 A g^{-1}), it could deliver a discharge capacity of 730 mA h g^{-1} (Fig. 12j). The authors adopted the same method to synthesize core–shell structured Zn_2SnO_4–C microspheres.[187] In this report, the amount of PVP was controlled to adjust the thickness of the carbon shell, demonstrating the versatility and simplicity of this method. Wang's group synthesized pomegranate-structured tin phosphide–carbon spheres for SIB anodes *via* the spray pyrolysis method.[188] After the synthesis of SnO_2/C microspheres *via* the spray pyrolysis method in the presence of sucrose and sulfuric acid in water and ethanol mixture solution, the resultant particles were milled with NaH_2PO_2 and heated at 280 °C to produce Sn_4P_3@C microspheres (Fig. 12k). During the post-treatment, Sn_4P_3 nanoparticles were aggregated at the core of the carbonaceous microspheres, as observed in the TEM image shown in Fig. 12l and m. The Sn_4P_3@C microspheres exhibited a stable cycling performance. A discharge capacity of 580 mA h g^{-1} could be achieved at the 120th cycle at 0.1 A g^{-1}, and the capacity retention measured from the 2nd cycle was 95% (Fig. 12n and o). Cho *et al.* synthesized carbon–$MoTe_2$ core–shell microspheres *via* spray pyrolysis and a subsequent tellurization step.[94] MoO_3 and a low amount of sucrose were added to the precursor spray solution and spray-pyrolyzed under a nitrogen atmosphere. Dense microspheres were then tellurized to yield the final core–shell morphology and applied as the anode in SIBs. The microspheres exhibited a discharge capacity of 241 mA h g^{-1} after 200 cycles at 1 A g^{-1}. Even at a high current density of 5 A g^{-1}, the microspheres exhibited a discharge capacity of 209 mA h g^{-1}.

3.3.3 Heterogeneous yolk–shell structures. The yolk and shell materials of yolk–shell structured materials discussed in the previous section were of identical compositions. In special cases, core and shell materials with different compositions, namely heterogeneous yolk–shell structures, can be prepared by phase separation during spray processes. Hong *et al.* reported yolk–shell structured Sn@C microspheres prepared by spray pyrolysis and post-treatment (Fig. 13a).[189] During spray pyrolysis at low temperatures, the droplet containing

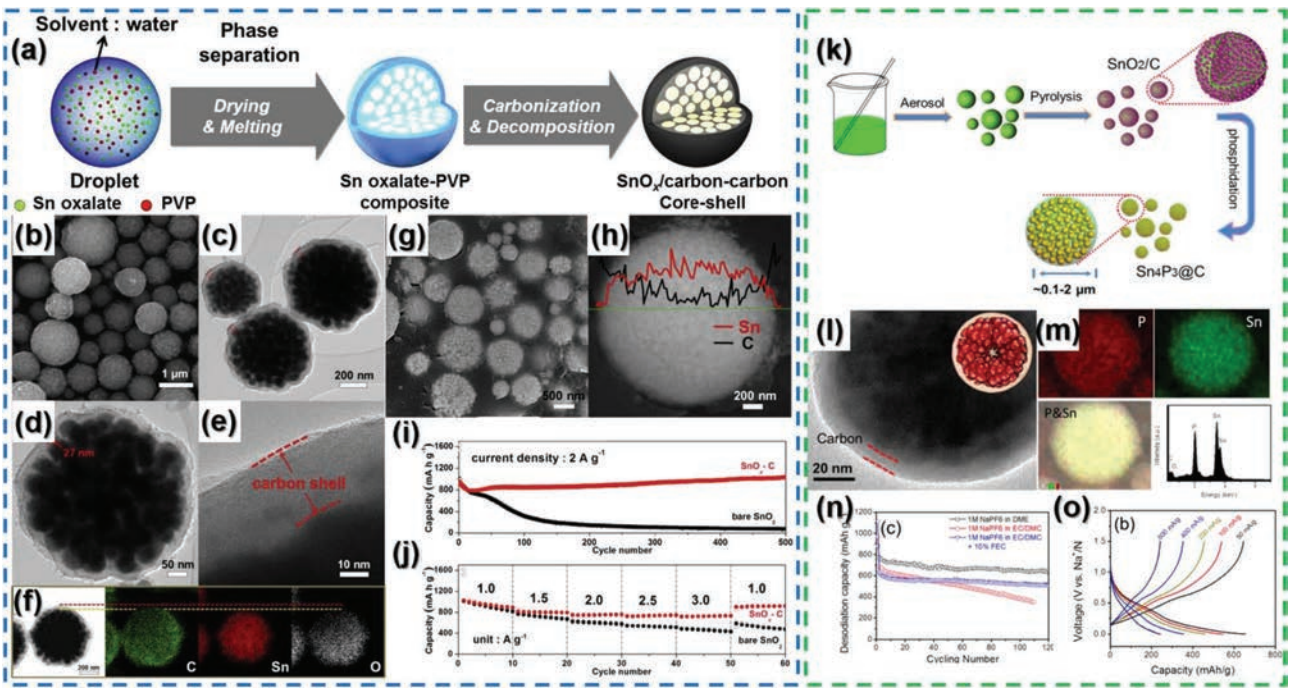

Fig. 12 (a) Schematic illustration of the synthetic process of SnO_x/carbon–carbon core–shell structured composite powder. (b) SEM image, (c–e) TEM images, and (f) elemental dot mapping images of the SnO_x/carbon composite, (g and h) SEM image and line profiles of the cross-section of the SnO_x–carbon composite powders and their (i) cycling and (j) rate performances. Reproduced with permission from ref. 186. Copyright 2015, Elsevier. (k) Schematic illustration of the synthetic process of Sn_4P_3@C pomegranates. (l) TEM image and (m) elemental dot mapping images of Sn_4P_3@C pomegranates and their (n) cycling and (o) rate performances. Reproduced with permission from ref. 188. Copyright 2017, Elsevier.

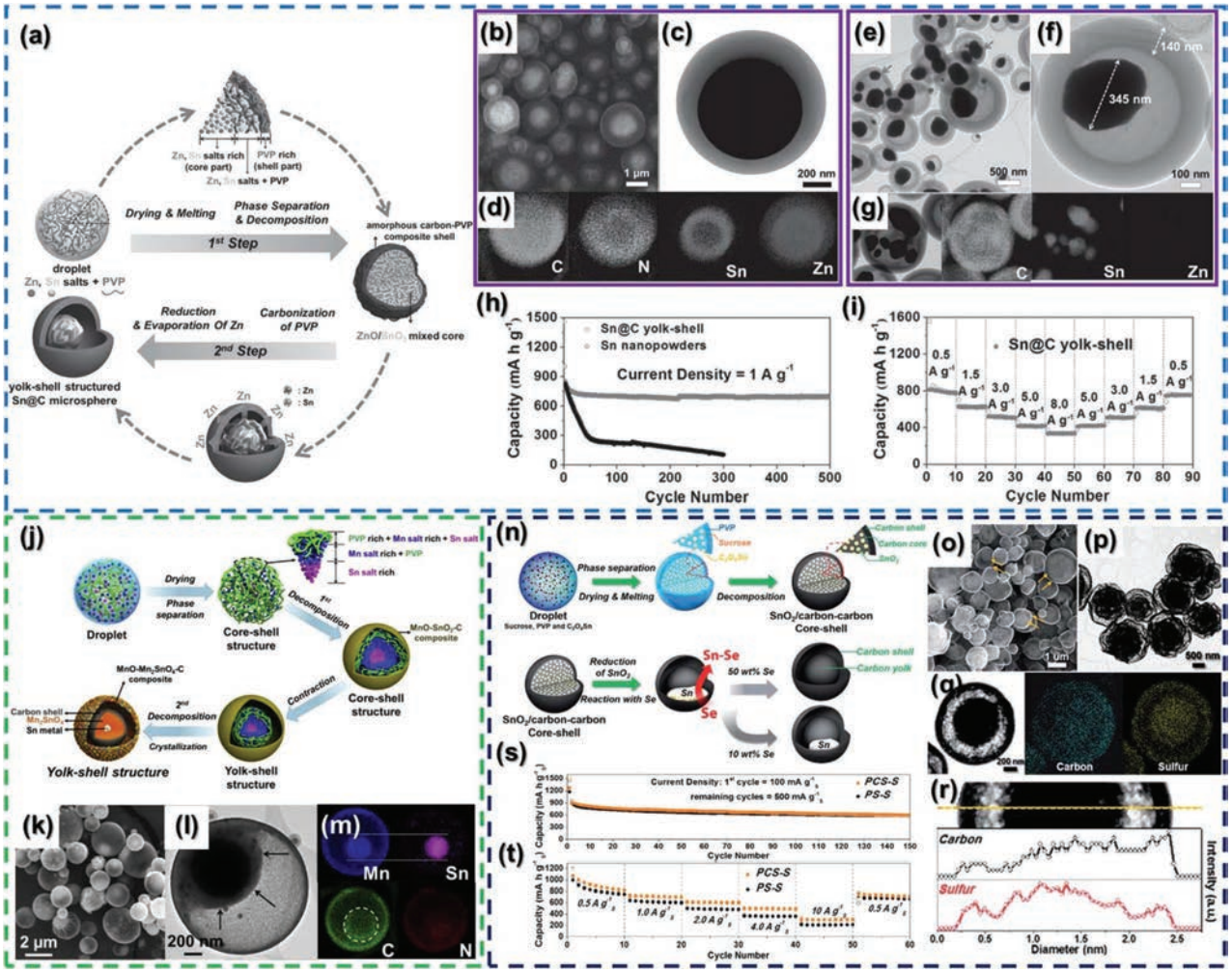

Fig. 13 (a) Schematic illustration of the synthetic process of yolk–shell Sn@C microspheres. (b) SEM image, (c) TEM image, and (d) elemental dot mapping images of SnO_2–ZnO–C composite microspheres prepared by the spray pyrolysis process. (e) TEM image, (f) magnified TEM image, and (g) elemental dot mapping images of yolk–shell Sn@C microspheres obtained after post-treatment. (h) cycling and (i) rate performances of Sn@C yolk–shell microspheres. Reproduced with permission from ref. 189. Copyright 2015, Wiley-VCH. Schematic illustration of the synthetic process of Mn–Sn–O–C composite powders with a yolk–shell structure. (k) SEM image, (l) TEM image, and (m) elemental dot mapping images of the yolk–shell powder prepared by spray pyrolysis at 700 °C. Reproduced with permission from ref. 190. Copyright 2016, Elsevier. (n) Schematic illustration of the synthetic process of the carbon–carbon yolk–shell microspheres. (o) SEM image, (p) TEM image of PCS, (q) elemental dot mapping images and line profiles of PCS-S microspheres and their (s) cycling and (t) rate performances. Reproduced with permission from ref. 191. Copyright 2017, The Royal Society of Chemistry.

Zn nitrate, Sn oxalate, and PVP dried and melted to form the core–shell powder (Fig. 13b–d). Molten metal salts (core) and PVP (shell) were separated due to a density difference, all of which hardly underwent decomposition due to the low preparation temperature. The post-treatment under a reducing atmosphere at 1000 °C led to the carbonization of PVP to form the amorphous carbon shell and the reduction of metal salts to Sn and Zn metals. As Sn and Zn have low melting temperatures, they liquefied and concentrated centrally within the carbon shell. In the meantime, the onset of Zn vaporization at around 900 °C resulted in the shrinkage of the Sn core. Resultantly, yolk–shell structured Sn@C microspheres were obtained (Fig. 13e–g). When evaluated as the anode material for LIBs, the hollow c arbon shell provided voids to buffer the large volume change of Sn during cycling, resulting in a highly stable performance over 500 cycles with a rate performance of 336 mA h g^{-1} at 8 A g^{-1}, as shown in Fig. 13h and i. Ju *et al.* reported the synthesis of a yolk–shell structured Mn–Sn–O–C composite.[190] Phase separation between the Sn salt, Mn salt, and PVP led to the formation of core–shell morphology at the initial stage, followed by the decomposition of each component to produce a yolk–shell structured Mn–Sn–O–C composite with a composition gradient (Fig. 13j–m). Yolk–shell structured carbon microspheres could also be synthesized by utilizing phase separation between two different carbon sources to induce a heterogeneous core–shell structured carbon microsphere. Hong *et al.* used two different carbon sources to induce a core–shell structured carbon microsphere.[191] Spray

pyrolysis of the solution containing sucrose, PVP, and Sn oxalate yielded a SnO_2/C–C core–shell structure (Fig. 13n). Carbon in the SnO_2/C core was mainly formed by the decomposition of carbon, and that in the shell was derived from PVP migrated to the outside of the microsphere. To obtain the yolk–shell structured carbon microsphere, the authors selenized the powder at 1000 °C to produce the Sn–Se alloy in the core that promptly evaporates at that temperature, resulting in the shrinkage of core carbon to produce yolk–shell carbon microspheres (Fig. 13o–q). The powder had plenty of micro- and mesopores, so it was utilized as a sulfur host material for Li–S batteries. The cathode with a sulfur content of 60 wt% with homogeneous inclusion could be achieved (Fig. 13r), and it exhibited a stable cycling performance, delivering 602 mA h g^{-1} after the 150th cycle at 0.5 A g^{-1} (Fig. 13s). The yolk carbon sphere increased the sulfur loading amount, and the high contact area between the electrolyte and yolk part improved the rate performance (Fig. 13t).

3.3.4 Janus structure. The Janus-structured particle has two or more distinct surfaces that have different chemical properties.[192,193] The term "Janus structure" was named after the Roman god Janus, who had two heads placed back to back. During the spray processes, Janus structures could be formed by phase separation within the composite. Choi *et al.* reported the synthesis of Janus structured SnO_2–CuO composite powder by flame spray pyrolysis (Fig. 14a).[194] The droplet

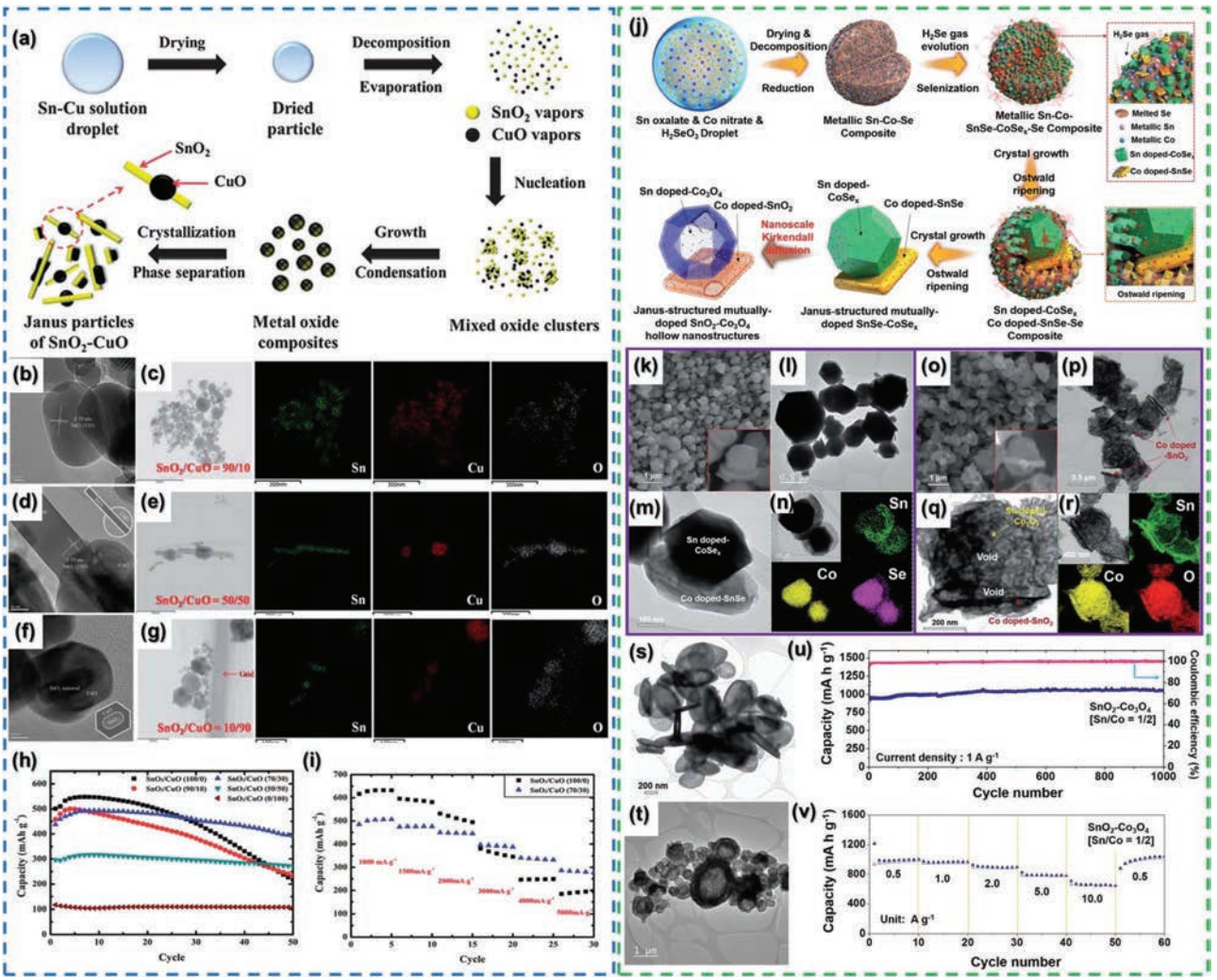

Fig. 14 (a) Schematic illustration of the synthetic process of Janus-structured SnO_2–CuO composite nanorods prepared from flame spray pyrolysis. (b–g) TEM images and elemental dot mapping images of Janus-structured (b and c) SnO_2–CuO (90/10 wt%), (c and d) SnO_2–CuO (50/50 wt%), and (f and g) SnO_2–CuO (10/90 wt%) composite nanoparticles and their (h) cycling and (i) rate performances. Reproduced with permission from ref. 194. Copyright 2013, The Royal Society of Chemistry. (j) Schematic illustration of the synthetic process of the Janus-structure powder consisting of mutually doped SnO_2 hollow nanoplates and Co_3O_4 hollow polyhedra, (k–r) SEM image, TEM images, and elemental dot mapping images of (k–n) Janus-structured mutually doped SnSe–$CoSe_x$ powder with a Sn/Co ratio of 1/2 and (o–r) SnO_2–Co_3O_4 powder formed by the nanoscale Kirkendall diffusion process. TEM images of (s) SnO_2 hollow nanoplates and (t) a Co_3O_4 hollow polyhedron formed by the nanoscale Kirkendall diffusion process. (u and v) Rate performances of Janus-structured microspheres. Reproduced with permission from ref. 195. Copyright 2017, The Royal Society of Chemistry.

containing Sn and Cu salts dried and decomposed to form oxides that immediately vaporized by the flame at temperatures exceeding 2500 °C to form SnO_2 and CuO vapors. The mixed oxide clusters condensed into nanosized metal oxide composites. Since SnO_2 and CuO do not form a solid solution, phase separation occurred and individual crystallization of SnO_2 and CuO by particle annealing and rearrangement during the late stage of the flame spray pyrolysis resulted in the formation of Janus structured SnO_2–CuO nanoparticles. As confirmed by XRD and TEM images, SnO_2 and CuO did not form a solid solution and crystallized into nanorods and nanospheres, respectively (Fig. 14b–g). When the weight ratio between SnO_2 and CuO was 70 : 30, the composite exhibited better cycling stability and rate performances compared with those of pure SnO_2 and CuO (Fig. 14h and i). Park *et al.* prepared a Janus-structured mutually doped SnO_2–Co_3O_4 hollow nanostructure by spray pyrolysis and subsequent post-treatment (Fig. 14j).[195] During the spray pyrolysis of the solution containing Sn, Co, and Se salts under a reducing atmosphere, the *in situ* selenization of Co and Sn components led to the formation of a Sn-doped $CoSe_x$/Co-doped SnSe/Se composite. The Ostwald ripening and crystal growth promoted by the high temperature of the reactor (900 °C) resulted in the formation of the Janus-structured mutually doped SnSe–$CoSe_x$ composite particle consisting of a Sn-doped $CoSe_x$ polyhedron and a Co-doped SnSe nanoplate. Further oxidation of this particle by post-treatment successfully converted it into hollow oxide nanostructures induced by nanoscale Kirkendall diffusion, which is discussed in detail in section 3.6. The morphology of the particle varied with respect to the ratio between Sn and Co precursors. The Sn component constituted a hollow nanoplate, and the Co component constituted a hollow polyhedron. The TEM images in Fig. 14k–r clearly reveal the phase separation of Sn and Co both in selenide and oxide particles. The mutual doping of Co and Sn is confirmed by the elemental mapping images in Fig. 14n and r, which exhibit the presence of trace amounts of Co and Sn at the nanoplates and polyhedra, respectively. When the spray pyrolysis was conducted with a single metal source, SnO_2 and Co_3O_4 formed hollow plates and a polyhedron-like morphology, confirming their characteristic growth behavior when constituting a Janus structure. At the Sn : Co ratio of 1 : 2, the Janus-structured SnO_2–Co_3O_4 exhibited a stable cycling performance over 1000 cycles with a reversible capacity of 1059 mA h g^{-1} at 1 A g^{-1} (Fig. 14u). It also exhibited a high reversible capacity of 666 mA h g^{-1} at a high current density of 10 A g^{-1}, demonstrating the good rate performance (Fig. 14v).

3.4 Inorganic and organic templates

3.4.1 NaCl template. NaCl-templated synthesis is an effective method for fabricating desired structures, including porous microspheres and nanoparticles. In 2002, Zachariah's group reported the synthesis of nanoporous Al_2O_3 particles by aqueous leaching of NaCl from an Al_2O_3–NaCl mixture prepared by spray pyrolysis.[196] The group found that various Al_2O_3 powders with different morphologies (nanoporous, hollow, dense, and nanoparticulate) can be obtained by controlling the amount of NaCl and the synthesis temperature. The most significant feature of NaCl-templated synthesis is that it does not require a preparation process before being used as a template. In addition, it can be readily removed by water, so its selective removal from the metal-based composite is easier and safer. Although the size and shape of the pores are not evenly aligned, this method is environmentally benign and scalable.

Recently, a number of NaCl-templated syntheses of porous materials by spray processes have been reported for use in energy storage.[197–206] Kang's group reported the synthesis of hollow Co_3O_4 and CuO nanoparticles by salt-assisted spray pyrolysis and spray drying, respectively.[197,198] For the synthesis of Co_3O_4 (Fig. 15a), the spray solutions containing Co nitrate and an excess amount of NaCl were sprayed and reduced to form Co–NaCl composite microspheres. Co nanoparticles were obtained by rinsing the NaCl matrix, where they were dispersed (Fig. 15b). Subsequent oxidation of metal nanoparticles under air produced hollow Co_3O_4 nanoparticles *via* the nanoscale Kirkendall diffusion, as shown in Fig. 15c. The sample oxidized at 500 °C showed the highest reversible capacity (775 mA h g^{-1} after 150 cycles at 1 A g^{-1}), as shown in Fig. 15d. It also exhibited a discharge capacity of 587 mA h g^{-1} at 5 A g^{-1} (Fig. 15e). The synthesis of CuO nanoparticles was achieved in a similar manner; however, the spray drying method was used instead.[198] Fan *et al.* prepared a porous Si/C anode material for LIBs by spray drying.[199] The solution containing NaCl, sucrose, and Si nanoparticle slurry was spray-dried, carbonized, and washed to obtain porous Si/C composite powder (Fig. 15f). Numerous pores in the range of hundreds of nanometers were created across the particle by washing off NaCl, as shown in the SEM image in Fig. 15g. By increasing the content of NaCl up to 40 wt%, the electrochemical performances of Si/C could be improved because of better structural stability during cycling (Fig. 15h and i). Zhang *et al.* prepared a flower-like Si/C composite by spray drying.[200] The authors used PVP as a carbon source to obtain a flower-like carbon framework, probably due to the characteristic deformation of PVP during carbonization that produces a debossed shape, as observed in the previous literature.[115,116,186,187,207] The flower-like composite exhibited an excellent cycling performance (898 mA h g^{-1} after the 200th cycle at a C/2 rate) compared with Si nanoparticles and sphere-like Si/C (prepared without NaCl), which was attributed to the partial void spaces that accommodated the volume expansion of Si during cycling. Ying *et al.* synthesized Sn/N-doped carbon microcage composites by spray drying.[201] The authors used ethylenediaminetetraacetic acid (EDTA) as the carbon and nitrogen source to obtain N-doped carbon. EDTA could also chelate the metal ions to uniformly distribute Sn in carbon. After spray drying and calcination at 700 °C under Ar, N-doped carbon/NaCl was formed, in which carbothermally-reduced Sn nanodots were embedded (Fig. 16a). The SEM and TEM images obtained after NaCl removal in Fig. 16b–d clearly show the pore structure of the Sn/N-doped carbon microcage compo-

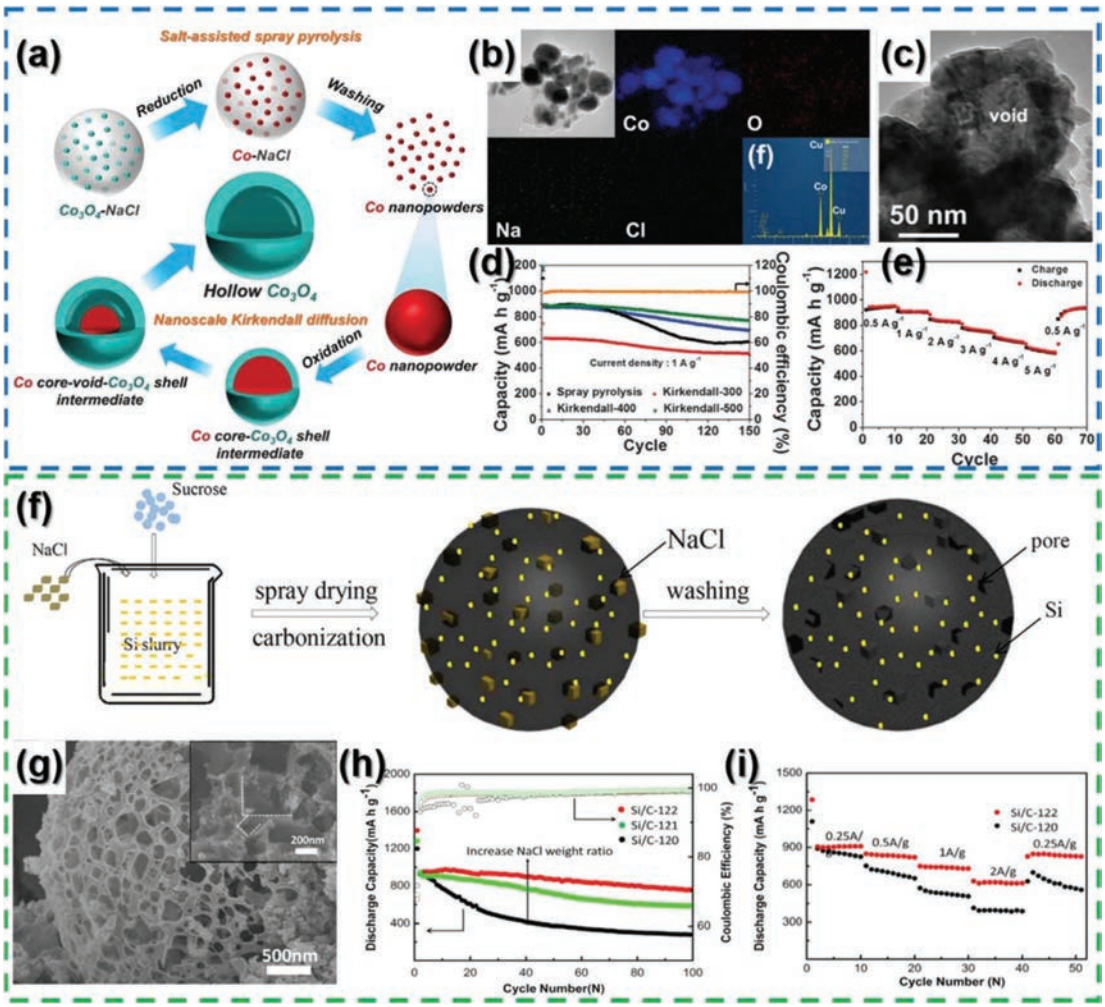

Fig. 15 (a) Schematic illustration of the synthetic process of the hollow Co_3O_4 nanopowders by salt-assisted spray pyrolysis applying nanoscale Kirkendall diffusion. (b) EDAX spectrum of the Co nanopowders obtained after the washing process. (c) TEM image of the hollow nanopowders obtained by post-treatment of metallic Co nanopowders and their (d) cycling and (e) rate performances. Reproduced with permission from ref. 197. Copyright 2015, the PCCP Owner Societies. (f) Schematic illustration of the synthetic process of the porous Si/C composite. (g) SEM image, (h) cycling and (i) rate performances of the porous Si/C composite. Reproduced with permission from ref. 199. Copyright 2016, Elsevier.

sites. Owing to the shortened ion diffusion distance, ample interior space, and ultra-small particle size of Sn, the composites maintained a reversible capacity of 472 mA h g^{-1} after 500 cycles when employed as the anode for LIBs, and 332 mA h g^{-1} after 300 cycles as the anode for SIBs (Fig. 16e and f). Qin *et al.* used NaCl to prepare a 3D N-doped porous graphene network embedded with SnSb nanocrystals (3D SnSb@N-PG) (Fig. 16g).[202] Instead of using graphene oxide nanosheets, the authors used ammonium citrate as the source of N-doped graphene, whose growth could be catalyzed by Sn^{2+} and Sb^{3+} ions. The reduction of the spray-dried precursor at 750 °C produced the SnSb alloy nanocrystals confined in NaCl cubes, followed by the formation of ultrathin N-doped graphene nanosheets catalyzed by the as-formed SnSb nanocrystals. The subsequent removal of NaCl produced 3D SnSb@N-PG, as shown in Fig. 16h–j. The open porous structure of 3D SnSb@N-PG with robustness greatly shortened the ion diffusion pathway and increased the ion diffusion rate, contributing to the extremely outstanding long-life high-rate cycling stability, namely, a capacity of 190 mA h g^{-1} at 10 A g^{-1} after 4000 cycles (Fig. 16k).

Kang's group reported the generalized synthesis of metal sulfides or selenides/carbon composite microspheres with nanorooms by spray pyrolysis for the anode materials of SIBs (Fig. 17a).[203,204] Dextrin and NaCl were used as the carbon source and porogen, respectively. After spray pyrolysis of the solution containing a metal salt, dextrin, and NaCl, porous metal oxide/carbon composite microspheres were obtained after washing off NaCl. The subsequent sulfidation or selenization could produce metal sulfides or selenides/carbon composite microspheres with nanorooms. The authors investigated the influence of the process parameters (amount of dextrin and NaCl, synthesis temperature, gas flow rate) to optimize the final morphology.[203] By changing the metal salts, Kang's

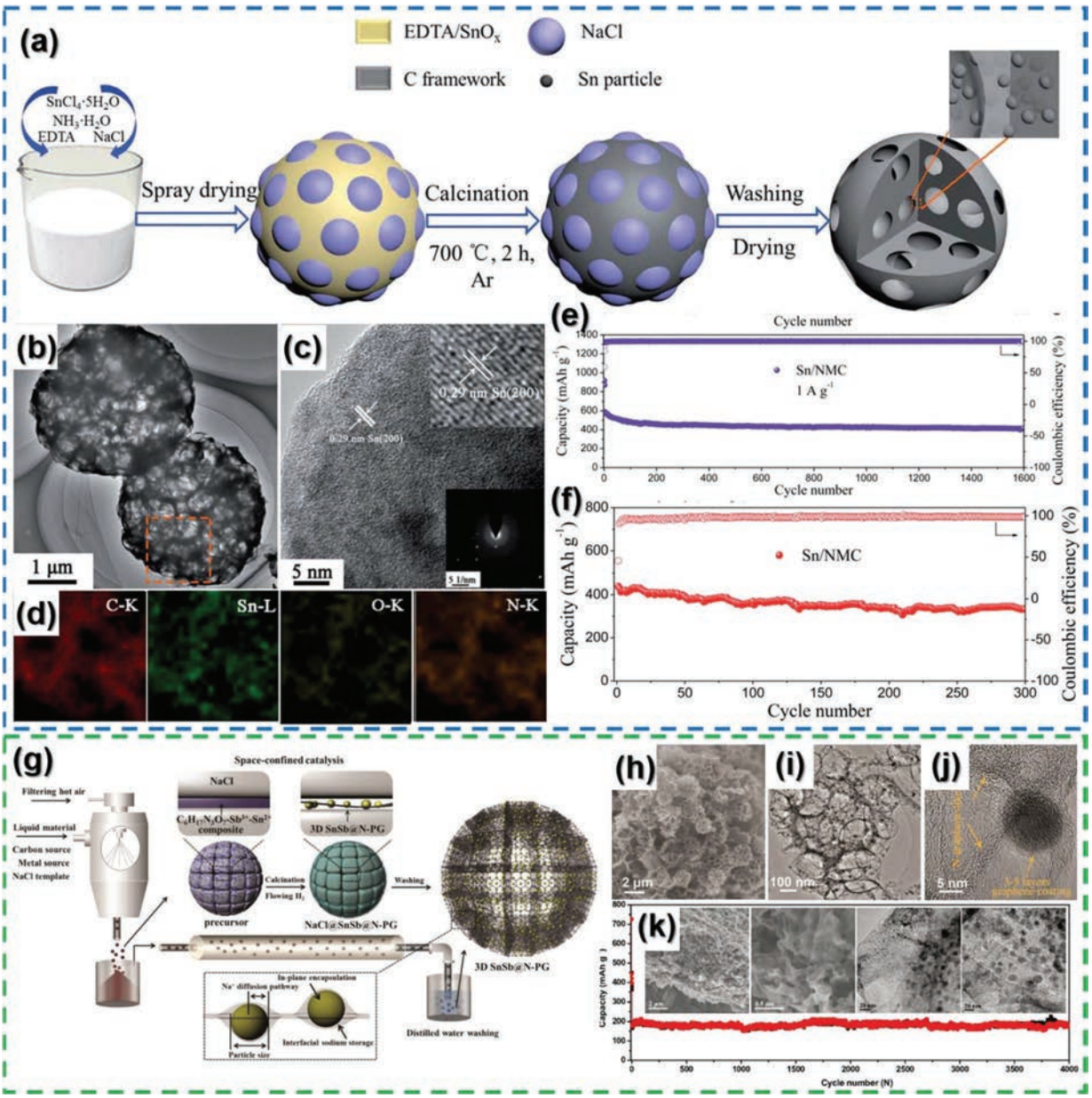

Fig. 16 (a) Schematic illustration of the synthetic process of Sn/N-doped carbon microcage composites. (b) TEM image, (c) HR-TEM image, and (d) elemental dot mapping images of Sn/N-doped carbon microcage composites and their (e) Li-ion and (f) Na-ion storage performances. Reproduced with permission from ref. 201. Copyright 2017, The Royal Society of Chemistry. (g) Schematic illustration of the top-down *in situ* synthesis of the 3D SnSb@N-PG composite. (h) SEM image, (i) TEM image, and (j) HR-TEM images of the composite microspheres and their (k) cycling performance at 10 A g^{-1}. Reproduced with permission from ref. 202. Copyright 2018, Wiley-VCH.

group showed that MoS_2, SnS, FeS_2, and $FeSe_2$-based nanostructures could be successfully synthesized, indicating the versatility of the synthetic method that suggests vast opportunities for developing other functional materials. In the case of MoS_2/C with nanorooms (MoS_2/C-NR) (Fig. 17b–d), restacking of MoS_2 nanosheets was effectively restricted by dextrin-derived carbon, as indicated by the number of MoS_2 layers observed in the TEM image in Fig. 17c. The nanorooms significantly increased the contact area with the electrolyte without compromising the structural stability. For these reasons, MoS_2/C-NR exhibited an ultrastable long-term cycling performance (385 mA h g^{-1} after the 350th cycle at 0.5 A g^{-1}) and excellent rate performance (287 mA h g^{-1} at 7.0 A g^{-1}) (Fig. 17e and f). Similarly, a hollow $FeSe_2$/graphitic carbon composite (H-$FeSe_2$/GC), which was prepared by the reduction and selenization of Fe_2O_3/carbon with nanorooms, also exhibited enhanced Na-ion storage properties.[204] The nanorooms and hollow $FeSe_2$ accommodated a large volume change during cycling. In addition, the graphic carbon framework coupled with the unique architecture of the microsphere provided a

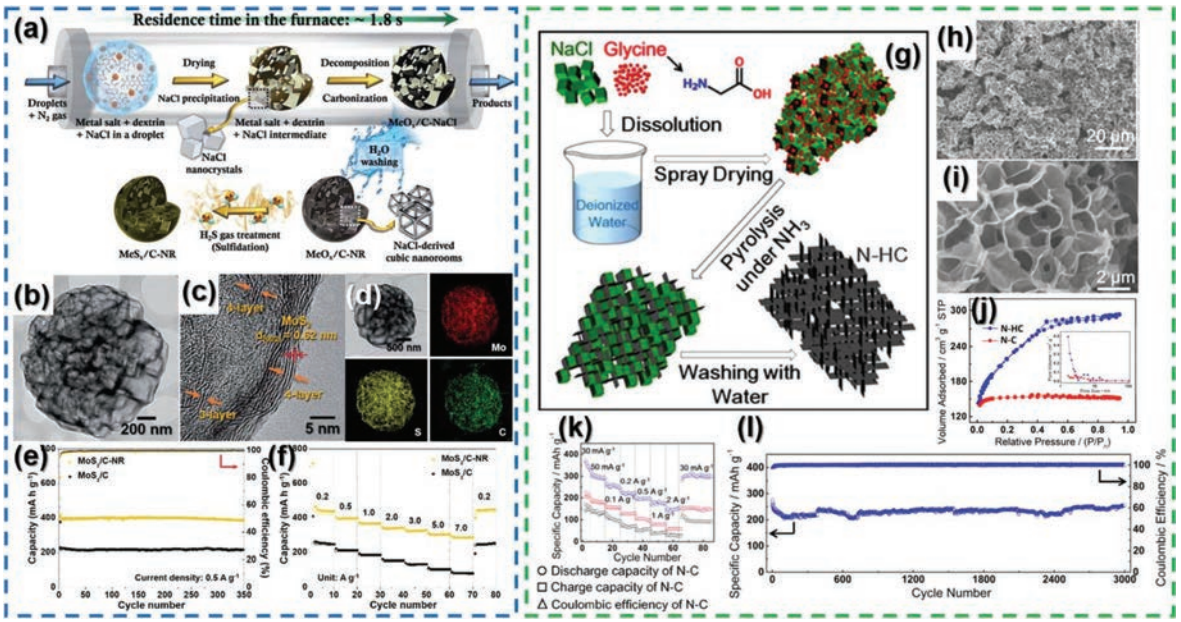

Fig. 17 (a) Schematic illustration of the synthetic process of MeS_x/C-NR microspheres *via* spray pyrolysis and subsequent treatments. (b) TEM image, (c) magnified TEM image, and (d) elemental dot mapping images of MeS_x/C-NR microspheres and their (e) cycling and (f) rate performances. Reproduced with permission from ref. 203. Copyright 2019, The Royal Society of Chemistry. (g) Schematic illustration of the synthetic process of N-HC. (h) Low and (i) high resolution SEM images, nitrogen physisorption isotherms and pore size distributions of N-HC. (k) Rate and (l) cycling performances of N-HC applied as an anode for SIBs. Reproduced with permission from ref. 206. Copyright 2018, Elsevier.

conductive channel that facilitated ion/electron transport. Consequently, H-$FeSe_2$/GC exhibited a stable discharge capacity of 510 mA h g^{-1} after 200 cycles at 0.2 A g^{-1} and a good rate capability (417 mA h g^{-1} at 5.0 A g^{-1}).

The preparation methods of N-rich hierarchically porous carbons by spray drying for use as anode materials in LIBs and SIBs have also been reported recently.[205,206] Zheng and his co-workers used glycine as both the nitrogen and carbon source.[205,206] A solution containing glycine and NaCl was spray-dried to obtain the glycine–NaCl composite, which was post-treated at 790 °C under a NH_3 atmosphere. After removing NaCl by washing, the hierarchically porous N-doped carbon (N-HC) was obtained (Fig. 17g). The abundant macropores in the honeycomb-like carbon were derived from NaCl removal (Fig. 17h and i). Even though the glycine molecule contains both N and C, the authors used NH_3 gas during post-treatment to minimize the loss of N by favoring the reverse reaction according to the Le Chatelier's principle. Therefore, the nitrogen content of N-HC (17.72 at%) was higher than the contrast sample prepared without NH_3 gas (9.98 at%). N-HC had a high specific surface area that provided sufficient contact with the electrolyte (Fig. 17j). Furthermore, as N-doping increased the electrical conductivity and capacity of carbon, N-HC displayed an excellent cycling and high rate performance when applied as the anode material for SIBs (Fig. 17k and l).

3.4.2 Polystyrene template. Polystyrene (PS) nanobeads have received great research attention because of their decomposition characteristics. Polystyrene nanobeads are readily removed during heat treatment even under an inert atmosphere, leaving spherical pores in the place of the previous PS nanobead locations.[207–215] Ko *et al.* synthesized SnO_2–carbon composite microspheres with three-dimensional ordered macroporous (3DOM) structures *via* the employment of polystyrene nanobeads (Fig. 18a).[213] An aqueous solution containing tin oxalate, dextrin, and PS nanobeads with sizes around 120 nm was spray-pyrolyzed, forming SnO_2–C 3DOM structures (Fig. 18b–d). During the spray pyrolysis process, dextrin was carbonized, tin oxalate was decomposed and formed SnO_2 nanoclusters uniformly distributed within the amorphous carbon network, while PS nanobeads decomposed into carbon dioxide and water vapor. The synthesized microspheres with macropores within showed higher discharge capacities compared to those of dense SnO_2 microspheres since the interconnected pore network provided a higher active area for electrochemical reactions. The microspheres delivered 509 mA h g^{-1} after the 1000th cycle at 1.5 A g^{-1} (Fig. 18e). A discharge capacity of 389 mA h g^{-1} was achieved at a high current density of 9 A g^{-1}, owing to the synergistic effects of the interconnected hollow nanoballs that enabled facile electrolyte penetration and shortened the lithium ion diffusion pathway. Zhao and his co-workers reported the polystyrene-template-assisted synthesis of a Li_3VO_4/C/rGO ternary composite with a honeycomb-like structure for use as an anode material in LIBs.[214] V_2O_5, $LiCO_3$, glucose, GO, and PS were added to the aqueous spray solution and spray-dried at 210 °C. The spray-dried powder was calcined at 600 °C for 10 hours under an Ar atmosphere to produce the Li_3VO_4/C/rGO ternary composite (Fig. 18f–i). The prepared microspheres exhibited 312 mA h

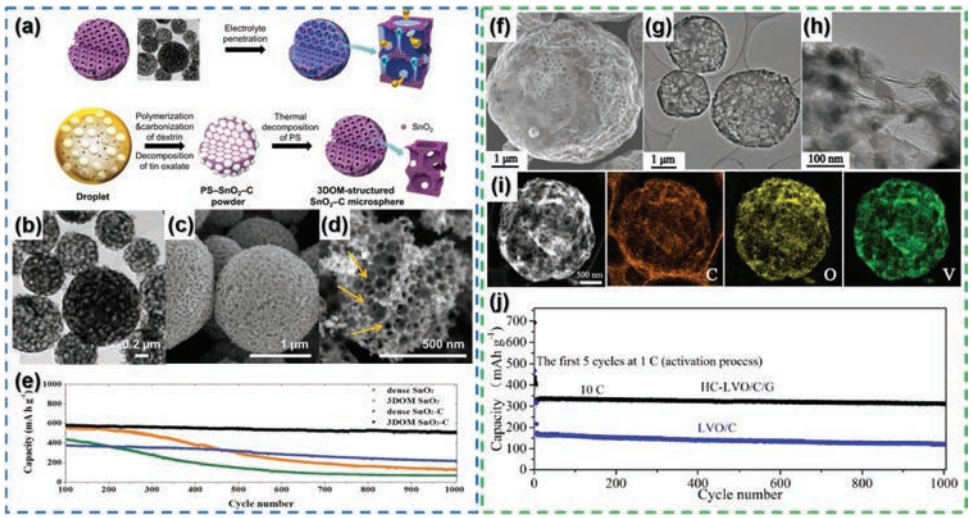

Fig. 18 (a) Schematic illustration for electrolyte penetration and Li-ion and electron transport in a 3DOM-structured material and the formation process of 3DOM-structured SnO_2–C microspheres, (b) TEM image and (c) SEM image of the microspheres, (d) SEM image of the crushed powder, and (e) cycling performance of the microspheres at 1.5 A g^{-1}. Reproduced with permission from ref. 213. Copyright 2014, Wiley-VCH. (f) SEM image and (g and h) TEM image of the HC-LVO/C/G composite, (i) elemental dot mapping images, and (j) cycling performance of the microspheres at 10C rate. Reproduced with permission from ref. 214. Copyright 2017, Elsevier.

g^{-1} even after 1000 cycles at 10C rate (Fig. 18j). These microspheres also exhibited a great rate performance. A stable capacity of 80 mA h g^{-1} could be achieved at an extremely high current density of 100C. Ko *et al.* proposed the one-pot synthesis of ant-cave-structured MoO_3–carbon microballs by the use of PS nanobeads in the spray pyrolysis process.[215] Spraying of an aqueous solution containing PS nanobeads, molybdenum salt, and sucrose at a high temperature of 900 °C under an Ar atmosphere yielded MoO_x–C microspheres with an ant-cave-like structure (Fig. 19). Due to the high temperature of 900 °C, partial melting and sintering of MoO_x species destroyed the once-spherical nanovoids and nanochannels inside the MoO_x–C microspheres (Fig. 19b and c). Consequently, one atomized droplet containing PS nanobeads, sucrose, and Mo salt was transformed into one MoO_x–C microsphere with an ant-cave-structure *via* one-pot spray pyrolysis. When applied as the anode material for LIBs, the ant-cave-structured MoO_x–C microspheres exhibited superior Li-ion storage properties compared with well-faceted crystal structured MoO_3 and spherical-like MoO_3 powders. The ant-cave-structured microspheres exhibited a high discharge capacity of 733 mA h g^{-1} after 300 cycles at 2 A g^{-1} (Fig. 19d). The high discharge capacity of 679 mA h g^{-1} could be obtained at 3 A g^{-1}, which is attributed to the unique structure with interconnected nanopores (Fig. 19e). Cho and his co-workers developed a strategy for the synthesis of coral-like yolk–shell-structured nickel oxide/carbon composite microspheres (Fig. 19f).[207] Nickel nitrate, PVP, and PS nanobeads were dissolved/dispersed in aqueous solution and spray-pyrolyzed at 700 °C under a nitrogen atmosphere at a flow rate of 10 L min^{-1}. The spray-pyrolyzed product was annealed at 250 °C for 1 hour under an air atmosphere to transform Ni into the NiO phase and control the amount of carbon in the structure. PS nanobeads were decomposed at a temperature higher than 500 °C and generated numerous mesopores. At a spray pyrolysis temperature of 600 °C and higher, the inner part of the material was thermally contracted, resulting in the hollow space between the yolk and the shell. The SEM and TEM images (Fig. 19g–i) of the coral-like yolk–shell-structured nickel oxide/carbon composite microspheres clearly revealed the mesoporous yolk and shell, and the void space in between. The yolk–shell structured NiO/C microspheres exhibited a stable cycling performance until 1000 cycles at 2 A g^{-1} (Fig. 19j). The anode exhibited 389 mA h g^{-1} at a high current density of 10 A g^{-1}, which is attributed to the existence of numerous interconnected mesopores that provided facile electrolyte accessibility and shortened the Li-ion diffusion length.

3.4.3 Metal salt derivative templates. Using metal salt derivatives (metal a nd metal oxides) as templates is a common and simple method to produce porous particles. Suslick's and Skrabalak's groups reported various porous particles obtained by the selective removal of metal salt derivatives from composite microspheres prepared by spray processes.[181–183,216–220] The most significant feature of this method is that the pore structures (pore size, pore volume, and specific surface area) of the microspheres are tunable by adjusting the concentration of the template materials. Therefore, a large number of recently reported porous microspheres by spray processes have been applied as sulfur and selenium hosts for cathode materials of Li–S and Li–Se batteries, respectively, since their electrochemical properties are closely dependent on the pore structure.[221–227]

Sohn *et al.* reported the synthesis of hierarchical porous spherical carbon (PSC) by using silica as the pore template.[221] After the spray pyrolysis of the solution containing colloidal silica, tetraethyl orthosilicate (TEOS), and phenol resin, the

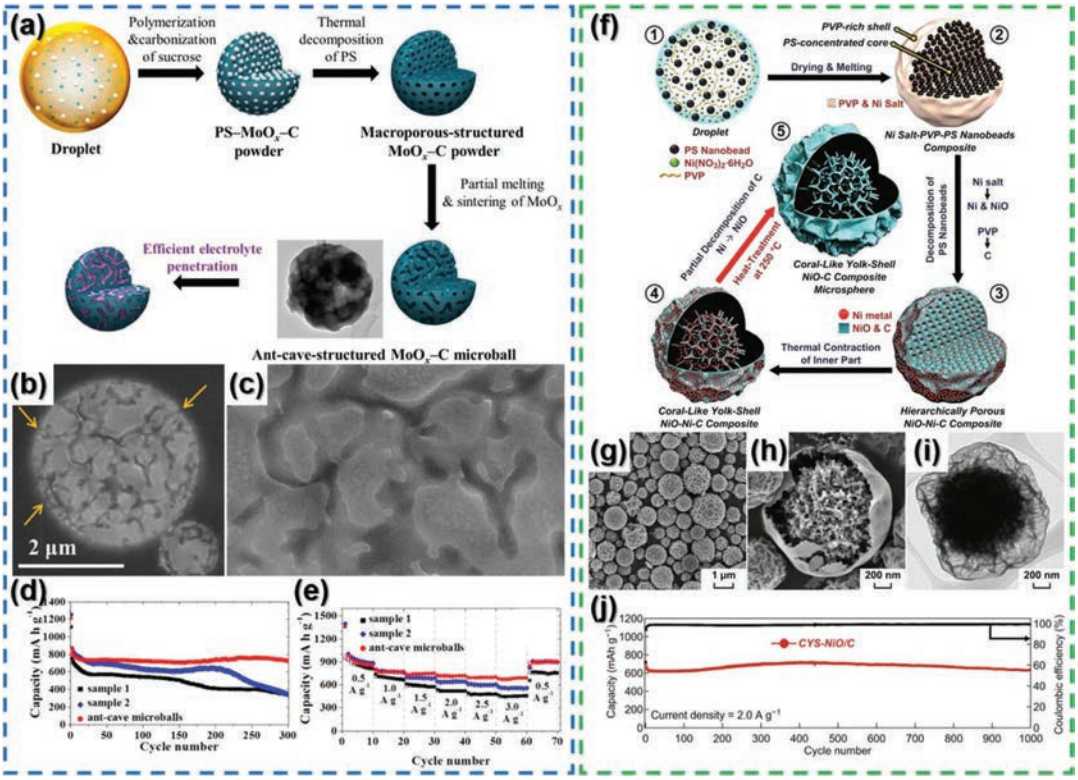

Fig. 19 (a) Schematic illustration of the synthetic process of ant-cave-structured molybdenum oxide-C microballs, (b) low and (c) high resolution SEM images of the microballs, (d) cycling performance at 2 A g^{-1}, and (e) rate performance. Reproduced with permission from ref. 215. Copyright 2013, American Chemical Society. (f) Schematic illustration of the synthetic process of the coral-like yolk–shell structured NiO/C composite microspheres, and the corresponding (g and h) SEM images, (i) TEM image, and (j) cycling performance at 2 A g^{-1}. Reproduced with permission from ref. 207. Copyright 2019, Springer Nature.

produced composite powder was carbonized at 900 °C and etched with HF to obtain PSC. The authors used two different silica sources for hierarchical porosity: colloidal silica for mesopores and TEOS for micropores. By optimizing the ratio between colloidal silica and TEOS, PSC could achieve a BET surface area as high as 2640 m^2 g^{-1} and a pore volume of 2.13 cm^3 g^{-1} with a sulfur loading of 60 wt%. By the 50th cycle, PSC showed a capacity of 690 mA h g^{-1} at the 0.1C rate. Other studies on the use of silica templates during spray processes for the synthesis of host materials for sulfur and selenium have also been reported.[222–224] Shi *et al.* proposed the use of layer double oxide (LDO) as a pore template and catalyst for graphene growth (Fig. 20a).[225] The authors prepared nanosized MgAl-layered double hydroxides (MgAl-LDHs) by co-precipitation. MgAl-LDHs were re-dispersed in water to form a colloidal solution, which was spray-dried to produce macroporous MgAl-LDH nanoparticle-aggregated microspheres. MgAl-LDHs were converted into MgAl-LDOs during calcination at 950 °C, which catalyzed the growth of the graphene layer under a CH_4 gas flow. Etching of MgAl-LDOs produced graphene microspheres (GMS) consisting of interconnected 20–50 nm-sized graphene nanocages, as shown in Fig. 20b–d. When employed as the sulfur host for the Li–S battery cathode, GMS could accommodate 78 wt% of sulfur content (Fig. 20e–h). Endowed with a hierarchically porous architecture and high electric al conductivity, flexible GMS paper exhibited an areal capacity of 2.01 mA h cm^{-2} over 80 cycles, corresponding to a 75.3% capacity retention (Fig. 20i). It also exhibited a high rate capacity retention of 46.7% at 1.35 mA cm^{-2} (Fig. 20j).

Furthermore, Kang's group reported the synthesis of mesoporous graphitic carbon–TiO_2 composite microspheres by spray drying (Fig. 20k).[226] The precursor solution containing Fe nitrate, TiO_2, and maltodextrin was spray-dried to form a dense precursor composite. Subsequent heat treatment under a reducing atmosp here resulted in the formation of Fe nanocrystals, which could catalyze the partial graphitization of carbon formed by maltode xtrin. In contrast, TiO_2 maintained its original phase after the heat treatment. Removal of Fe nanocrystals by HCl produced mesopores (Fig. 20l and m), in which nearly 60 wt% of sulfur could be infiltrated (Fig. 20n and o). Graphitic carbon provided enhanced electrical conductivity, and TiO_2 nanocrystals could effectively trap lithium polysulfides during cycling. As a result, the microsphere exhibited a discharge capacity of 599 mA h g^{-1} after 500 cycles at 1C rate, with a decent rate performance of 516 mA h g^{-1} at 5C rate (Fig. 20p and q). The same group also reported the synthesis of micro–mesoporous carbon microspheres using vanadium oxide as the pore template (Fig. 20r).[227] Spray pyrolysis of the

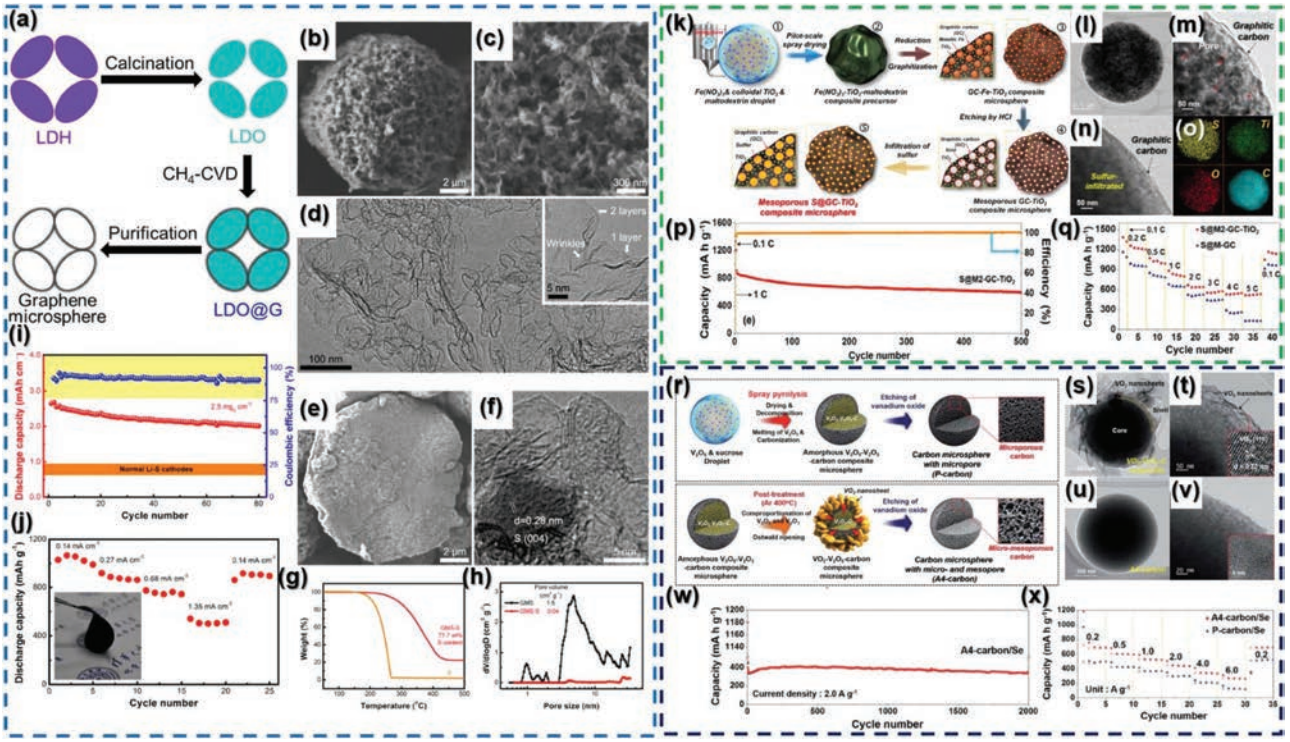

Fig. 20 (a) Schematic illustration of the synthetic process of GMSs. (b and c) SEM images of GMSs showing 3D interconnected graphene networks, and (d) TEM image of GMSs with few-layer graphene walls. (e) The cross-sectional SEM image, (f) HRTEM image, (g) N_2 thermogravimetric profile, and (h) the pore size distribution of GMS-S composites and their (i) cycling and (j) rate performances. Reproduced with permission from ref. 225. Copyright 2015, Elsevier. (k) Schematic illustration of the synthetic process of sulfur-infiltrated mesoporous graphitic carbon–TiO_2 composite microspheres. (l and m) TEM images of mesoporous graphitic carbon–TiO_2 microspheres, and the corresponding (n) TEM and (o) elemental dot mapping images obtained after sulfur infiltration. (p) Cycling and (q) rate performances when tested as a cathode for Li–S batteries. Reproduced with permission from ref. 226. Copyright 2017, Elsevier. (r) Schematic illustration of the synthetic process of carbon microspheres with a bimodal pore size distribution of micro- and mesopores by spray pyrolysis. TEM images of VO_2–V_2O_5–C composite microspheres (s and t) before and (u and v) after the etching process. (w) Cycling and (x) rate performances of micro–mesoporous carbon–selenium composites. Reproduced with permission from ref. 227. Copyright 2018, The Royal Society of Chemistry.

solution containing V_2O_5 and sucrose under a N_2 atmosphere produced amorphous V_2O_5–V_2O_3–carbon composite microspheres. The carbothermal reduction of V_2O_5 at a high temperature of 900 °C resulted in the partial formation of V_2O_3 nanocrystals. The etching of vanadium oxides by nitric acid produced microporous carbon microspheres. However, when an additional post-treatment was conducted, the crystal growth of VO_2 nanosheets by Ostwald ripening occurred (Fig. 20s and t), resulting in the formation of micro- and mesopores in the carbon microspheres after the etching process (Fig. 20u and v). The presence of both micro- and mesopores in the carbon microspheres enabled the faster conversion reaction of Se_n with Li. Thus, the micro–mesoporous carbon–selenium composite exhibited an enhanced capacity and rate performance compared with those of microporous carbon microspheres (Fig. 20w and x).

3.4.4 Other templates. Template materials other than metals or metal oxides are also utilized to obtain desired nanostructured materials for rechargeable batteries.[228–230] Jung *et al.* synthesized hierarchical porous carbon microspheres (HPC) as the host material for the Li–S battery cathode (Fig. 21a).[228] The authors used sucrose sodium carbonate as a carbon source and pore template, respectively. As discussed in section 3.3.1, spray pyrolysis of the solution containing only the carbon source cannot yield carbon microspheres.[181–184] Sodium carbonate can act as a base catalyst for the carbonization of sucrose, as it produces composite microspheres with carbon. Meso- and macropores were produced by removing precipitated sodium carbonate and its byproducts (sodium bicarbonate and sodium oxide), all of which are water-soluble (Fig. 21b–e). The remarkable feature of HPC was that a rich amount of micropores was generated along the carbon shell (Fig. 21f and g). As the solvent evaporated from the outer surface of the droplet, the solvent in the core continuously migrated outward through capillary force. In the meantime, chelated $C_{12}H_{21}O_{11}^{-}Na^{+}$ dissolved in the solvent migrated together toward the shell of the droplet. Consequently, micropores were formed by washing out the nanosized Na salt from the carbonized chelated compound, as well as by the formation of various gases generated during the carbonization of sucrose. When applied as the cathode material for Li–S batteries, micropores in the carbon shell served as a barricade to

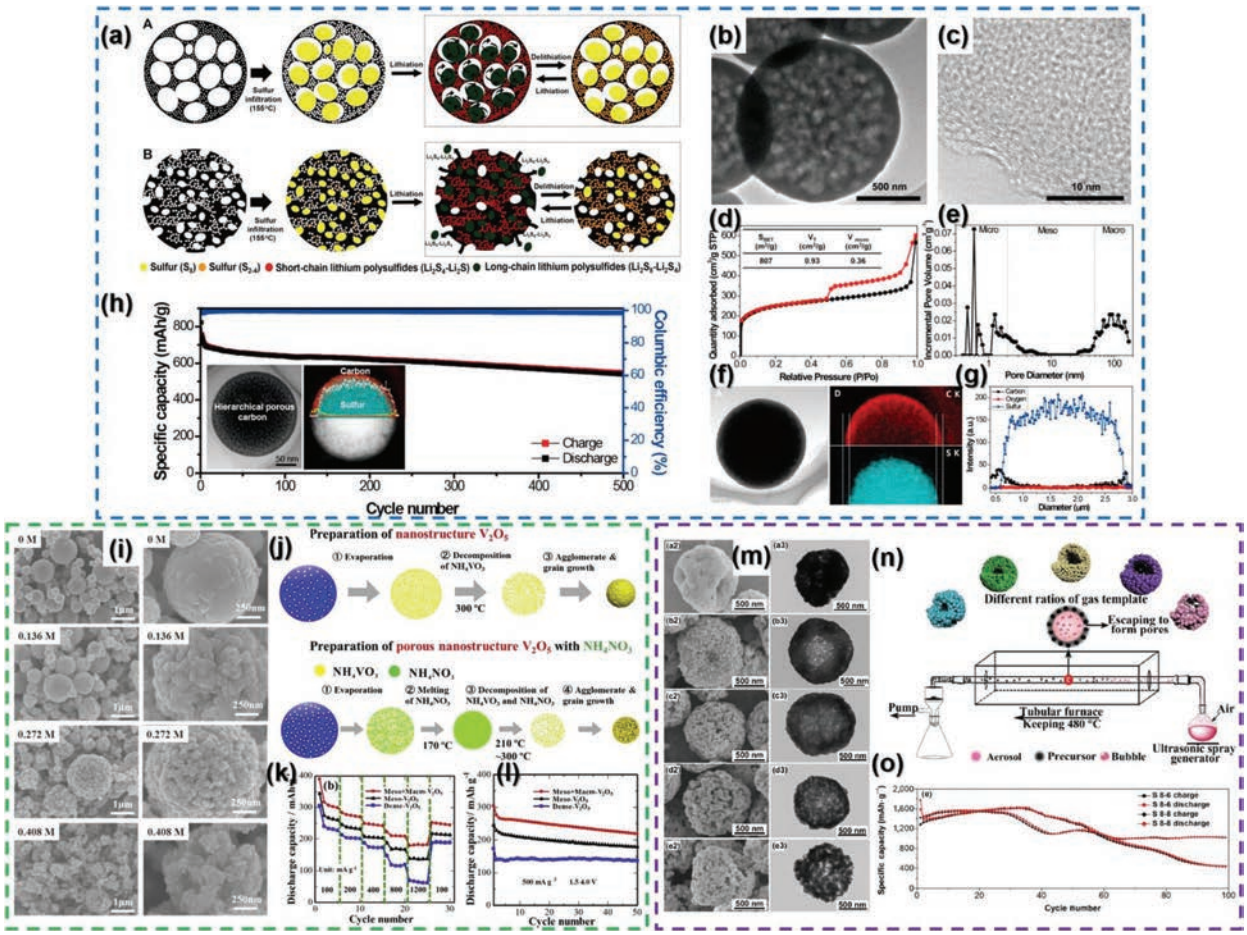

Fig. 21 (a) Schematic illustration of the electrode structures and their electrochemical processes where hierarchical porous carbon particles have micropores in the outer shell, surrounding the inner meso- and macropores. The structures enable the formation of soluble long-chain lithium polysulfides and their dissolution is suppressed by the outer micropores. (b) TEM image of the HPC sphere, (c) HRTEM image of the outer shell, (d) N_2 adsorption–desorption isotherms, and (e) the pore size distribution. (f) TEM and STEM images, (g) line profile of the HPC-S sphere, (h) cycling performance of HPC-S applied as a cathode for Li–S batteries. Reproduced with permission from ref. 228. Copyright 2014, American Chemical Society. (i) SEM images of the V_2O_5 microspheres synthesized by spray pyrolysis with different NH_4NO_3 concentrations. (j) Schematic illustration of the particle formation with and without NH_4NO_3 additive in the spray pyrolysis process. (k) Cycling and (l) rate performances of the V_2O_5 microspheres. Reproduced with permission from ref. 229. Copyright 2016, Elsevier. (m) SEM and TEM images of the microspheres synthesized at $Co(NO_3)_2{\cdot}6H_2O$/$CO(NH_2)_2$ mass ratios of 8 : 0, 8 : 2, 8 : 4, 8 : 6, and 8 : 8. (n) Schematic illustration for spray pyrolysis and the formation of porous hollow Co_3O_4 microspheres and (o) cycling performance of the synthesized Co_3O_4 microspheres. Reproduced with permission from ref. 230. Copyright 2018, Springer Nature.

suppress the dissolution of long-chain lithium polysulfides. Consequently, HPC preserved 539 mA h g^{-1} after 500 cycles at 2.4C rate, which corresponded to the capacity retention of 77% (Fig. 21h). Kong *et al.* introduced ammonium nitrate (NH_4NO_3) as a gaseous template to control the porosity of V_2O_5 particles (Fig. 21j).[229] NH_4NO_3 decomposes at 210 °C into N_2, H_2O, and O_2 gases. Therefore, vigorous evolution of gases owing to the decomposition of NH_4NO_3 resulted in the formation of porous V_2O_5 particles. As observed in the SEM images in Fig. 21i, a precursor solution with 0.272 M of NH_4NO_3 produced meso- and macroporous V_2O_5 particles, in clear contrast to the particles prepared without NH_4NO_3. The introduction of meso- and macropores in V_2O_5 significantly enhanced the rate performance (180 mA h g^{-1} at 1.2 A g^{-1}) as the anode material in LIBs, which was much higher than that of dense V_2O_5 (70 mA h g^{-1}) (Fig. 21k). The cycling performances of the samples are compared in Fig. 21l. A similar effect was observed when urea was used as the gaseous template. Du *et al.* investigated the effect of urea concentration in the Co nitrate spray solution on the pore structure of the resultant Co_3O_4 microspheres (Fig. 21n).[230] As the concentration of urea increased, the morphology of Co_3O_4 gradually changed from a depressed to a perfectly spherical form, and the size of the pores became larger, as shown in Fig. 21m. Such an outcome was attributed to the supporting force owing to the escaping gas evolved from the decomposition of urea, inverting the depression of the microsphere and enlarging the pore sizes. The optimized porous hollow Co_3O_4 microspheres exhibited a capacity of 1013 mA h g^{-1} after the 100th cycle at 0.2C rate (Fig. 21o).

3.5 Application of colloidal particles

Unlike the strategy of including nanosized particles that are later removed as templates in the spray solution, which is explained in section 3.4, this approach utilizes the colloidal particles that are included in the final products. The general colloidal particles are either active materials with high theoretical capacities or carbonaceous materials with high electrical conductivity and ability to alleviate the volume change of electrode materials. Through this approach, pre-designable particles with a wider range of functionalities could be spray-processed to obtain microspheres with desired properties.

3.5.1 Si. Silicon exhibits a high theoretical capacity of 4200 mA h g^{-1}, which is more than ten times the theoretical capacity of the conventional graphite anode (372 mA h g^{-1}).[231–233] However, silicon materials suffer largely from volume expansion up to 400% during lithiation and delithiation processes.[233,234] The extraordinarily large volume change results in pulverization, contact loss of active materials from the current collector, and unstable solid-electrolyte-interphase (SEI) formation.[233,234] Choi's group demonstrated that the encapsulation of silicon nanoparticles in carbon effectively buffers volume changes.[232] Silicon nanoparticle–carbon core–shell nanofibers were prepared by electrospinning and subsequent heat treatment under an Ar atmosphere, and the nanofiber showed stable cycling performance for up to 300 cycles when cycled at 3C rate. This strategy can be adopted for use in spray processes, where monodispersed silicon nanoparticles can be confined within carbonaceous materials.

Several groups have reported on the synthesis of silicon nanoparticle–carbon composite microspheres for fully utilizing the high capacities of silicon anodes and enhancing the cycle life by the spray processes.[235–238] Guo's group synthesized watermelon-inspired Si/C microspheres with hierarchical buffer structures by the facile spray drying process (Fig. 22a).[237] Nanosized silicon nanoparticles (Fig. 22b) were successfully encapsulated in the C-coated shell, flake graphite, and carbon shell, making up watermelon-like dense microspheres. The carbon-coated silicon nanospheres (Fig. 22c) were spray-dried, and the resultant microspheres are shown in the SEM images in Fig. 22d and e. The size of the dense structured microspheres varied to a large extent, which enabled the formation of an electrode layer with a close-packed structure filled with microspheres with different sizes, increasing the tap density and ultimately the energy density. When applied as the anode in the LIB, the watermelon-like microspheres exhibited highly stable structural stability, as the volume expansion of nanosized silicon was effectively buffered with the carbon-

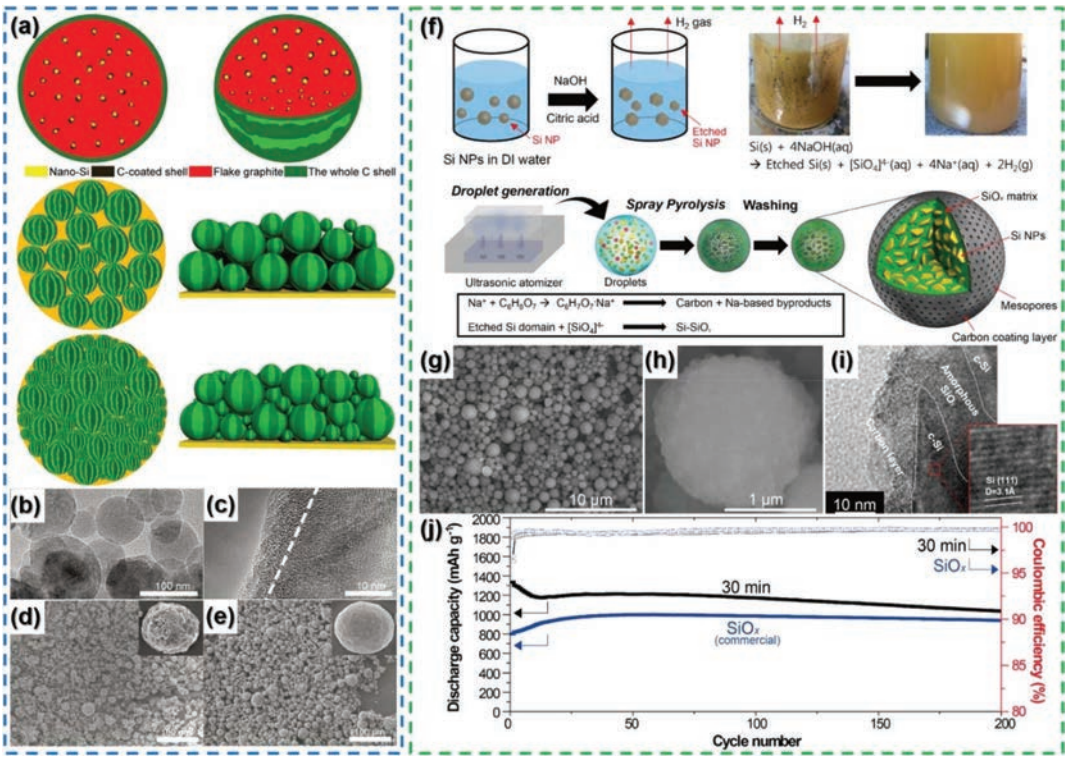

Fig. 22 (a) Schematic illustration of the watermelon-inspired Si/C microspheres and the packing model of Si/C anodes with single size distribution and optimized size distribution, (b) TEM image of nano-Si particles, (c) HRTEM image of carbon-coated nano-Si, and SEM images of Si/C with (d) low tap density and with (e) high tap density. Reproduced with permission from ref. 237. Copyright 2016, Wiley-VCH. (f) Schematic illustration of the synthetic process of the Si–SiO_x–C composite microspheres using one-step spray pyrolysis. (g) SEM image and (h) the magnified SEM image of the composite microsphere, (i) HRTEM image showing that etched Si NPs are embedded in the SiO_x matrix, and (j) cycling performance of the Si–SiO_x–C composite and commercial SiO_x. Reproduced with permission from ref. 238. Copyright 2017, American Chemical Society.

aceous materials surrounding them. 80% of the original charge capacity was retained after 250 cycles at 55 °C, which indicates excellent cycling performance even under severe conditions. Furthermore, 80% of the original capacity is maintained when the current density is varied from 0.2 to 5C rate. Lee *et al.* exploited the spray pyrolysis technique to synthesize a Si–SiO_x–C composite for use as the anode in LIBs (Fig. 22f).[238] Si nanoparticles were first etched with NaOH, then spray-pyrolyzed, resulting in Si nanoparticles embedded in a SiO_x matrix coated with carbon (Fig. 22g and h). The SEM image shown in Fig. 22g reveals dense microspheres of different sizes, which is beneficial from the perspective of energy density. The TEM image shown in Fig. 22i verifies the existence of Si, amorphous SiO_x, and carbon. Si–SiO_x–C exhibited a higher capacity for 200 cycles in comparison with commercial SiO_x due to the nanosized silicon particles encapsulated in the microspheres. The reversible capacities of Si–SiO_x–C at the 1st and the 200th cycle were 1334 and 1035 mA h g^{-1}, whereas the commercial SiO_x delivered 800 and 938 mA h g^{-1}, respectively (Fig. 22j).

3.5.2 Ceramic nanoparticles. Taniguchi's group synthesized spherical particles comprised of nanosized particles and proved their excellency when used as cathode materials in the LIB system.[239] In their research in 2002, $LiMn_2O_4$ and $LiM_{1/6}Mn_{11/6}O_4$ (M = Co, Al, Ni) microspheres composed of nanoparticles were prepared from an aqueous solution containing $LiNO_3$, $Mn(NO_3)_2$, $Co(NO_3)_2$, and $Al(NO_3)_3$, and the atomized droplets were pyrolyzed at 800 °C. Due to the high preparation temperature, the crystal growth of nanoparticles comprising microspheres was observed and the cathode material showed a capacity retention of 85% after 30 cycles at 0.2 mA cm^{-2}. In light of this superstructure, small predesigned nanoparticles could be sprayed, enabling the synthesis of superstructures consisting of designed particles homogeneously distributed within microspheres.[240–250] Jia *et al.* used spray pyrolysis to synthesize robust carbonaceous architectures consisting of Fe_3O_4 nanoparticles, which were prepared in advance through a co-precipitation method (Fig. 23a).[240] The merits of a robust architecture consisting of nanocrystals encapsulated in carbon include a short Li-ion diffusion length due to the fine size of the Fe_3O_4 building blocks, three-dimensional interconnected channels between the closely packed particles, and effective electron transport along the entire carbon network (Fig. 23b and c). The discharge capacity of the

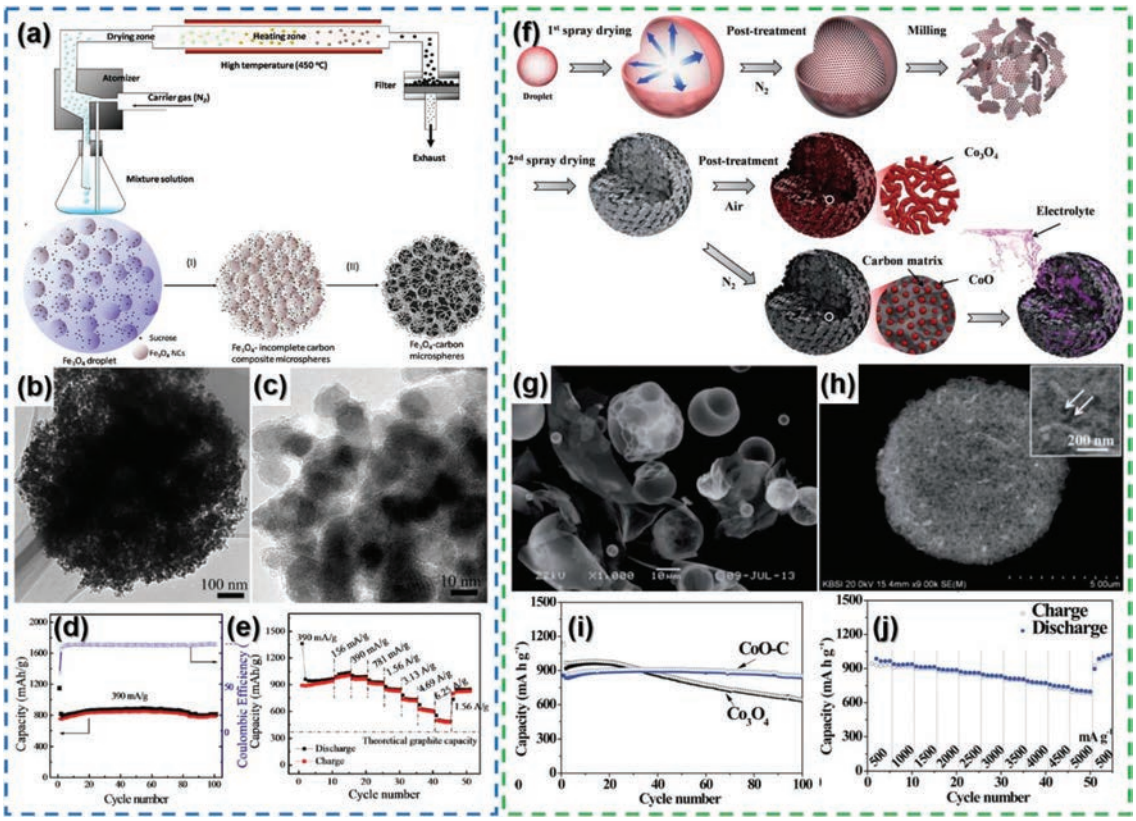

Fig. 23 (a) Schematic illustration of the synthetic process of Fe_3O_4/carbon nanocomposite particles, (b) TEM and (c) HR-TEM images of the hierarchically porous Fe_3O_4/C composite microspheres, (d) cycling and (e) rate performances of the microspheres. Reproduced with permission from ref. 240. Copyright 2012, American Chemical Society. (f) Schematic illustration of the synthetic process of mesoporous cobalt oxide powders with and without carbon. SEM images of (g) the precursor powder collected after the 1st spray drying and (h) CoO–carbon composite microspheres obtained after the 2nd spray drying. (i) Cycling and (j) rate performances of the synthesized microspheres. Reproduced with permission from ref. 241. Copyright 2014, The Royal Society of Chemistry.

microspheres was 840 mA h g^{-1} after 100 cycles at 390 mA h g^{-1} (Fig. 23d). The rate capability of the synthesized microspheres was tested at various current densities from 0.39 A g^{-1} to 6.25 A g^{-1}, where the discharge capacity of 482 mA h g^{-1} was achieved at a high current density of 6.25 A g^{-1}, which far exceeds the theoretical capacity of graphite (Fig. 23e). Kim *et al.* reported the two-step spray drying process to fabricate meso- and macroporous Co_3O_4 and CoO–carbon composite powders for use as anodes in LIBs (Fig. 23f).[241] The first spray drying process yielded powders several tens of micrometers in size due to the poor gas penetration (Fig. 23g), which were then ball-milled to produce Co_3O_4 nanoparticles. The particles were re-dispersed in aqueous solution and spray-dried for the second time, yielding meso- and macroporous microspheres (Fig. 23h). The discharge capacities of meso- and macroporous Co_3O_4 and CoO–carbon composite microspheres after 100 cycles at 1400 mA g^{-1} were 644 mA h g^{-1} and 855 mA h g^{-1} (Fig. 23i), respectively. CoO–carbon composite microspheres provided a discharge capacity of 698 mA h g^{-1} at 5 A g^{-1} (Fig. 23j).

3.5.3 Reduced graphene oxide. Reduced graphene oxide (rGO) has been applied to numerous applications because of its unique characteristics.[251–253] In particular, rGO has been extensively studied for hybridization with electrode materials for LIBs and SIBs, as well as Li–S and Li–O_2 batteries due to its high electrical conductivity.[253–255] Conventional amorphous carbon additives, including carbon black and carbon coatings, exhibit relatively lower electrical conductivities when compared with highly crystalline rGO. rGO offers an effective matrix that plays the role of a conducting backbone, which not only provides high electrical conductivity, but also serves as a mechanical buffer that alleviates the volume change of active materials.[256] Graphene is comprised of sp^2 bonded carbon arranged in a hexagonal two-dimensional lattice, ensuring notably high electrical conductivity and exhibiting a high surface/mass ratio.[256,257] rGO has been combined with various materials including CuO, TiO_2, GeO_x, WO_3, *etc.*, which enhanced the electrochemical properties of the composite microspheres employed as the electrode materials for rechargeable batteries.[112,258–280]

Luo *et al.* significantly improved the electrochemical properties of silicon nanoparticles by encapsulating them in graphene sheets *via* spray pyrolysis (Fig. 24a).[277] The microspheres exhibited a crumpled morphology due to the evaporation-induced capillary force,[281] and silicon nanoparticles were encapsulated in the graphene sheets (Fig. 24b and c). The cycling performance of silicon nanoparticles encapsulated in graphene nanosheets and bare silicon nanoparticles exhibited a clear difference. The capacity retention of Si–rGO after 250 cycles was 83% (a discharge capacity of 940 mA h g^{-1} was deli-

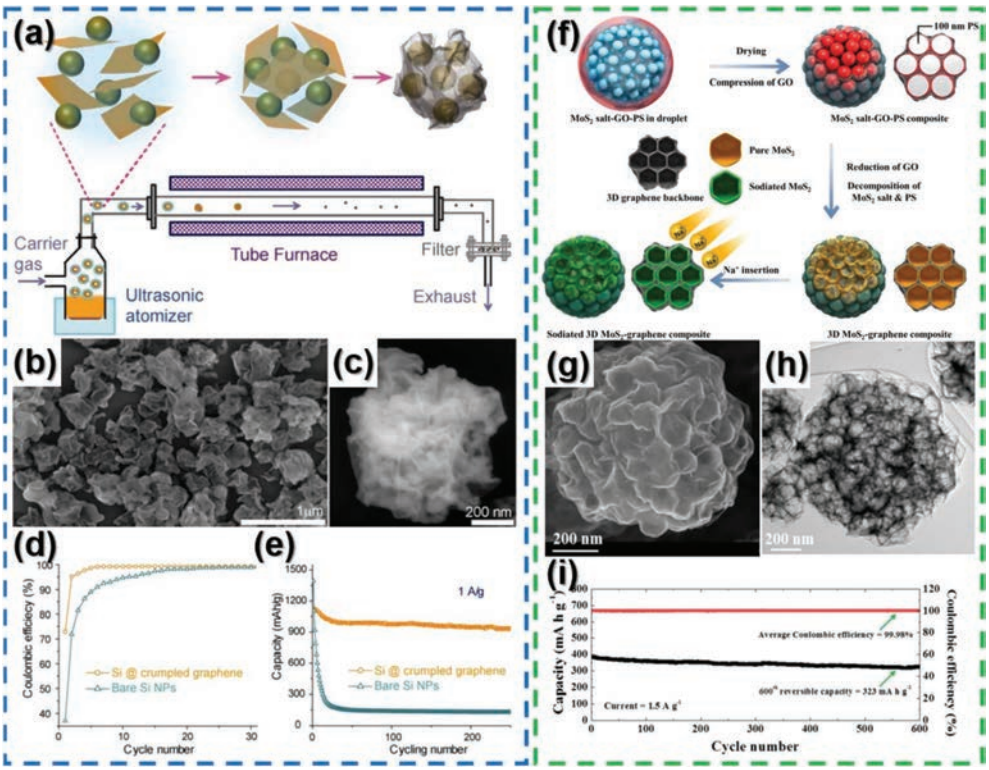

Fig. 24 (a) Schematic illustration of the synthetic process of aerosol-assisted capillary assembly of crumpled-graphene-wrapped Si nanoparticles. (b) Low and (c) high resolution SEM images of the graphene-wrapped Si, (d) coulombic efficiency and (e) cycling performance of the composite in comparison with the unwrapped Si at 1 A g^{-1}. Reproduced with permission from ref. 277. Copyright 2012, American Chemical Society. (f) Schematic illustration of the synthetic process of the 3D MoS_2-graphene composite microsphere, (g) SEM and (h) TEM images of the microspheres and (i) cycling performance at 1.5 A g^{-1}. Reproduced with permission from ref. 280. Copyright 2015, Wiley-VCH.

vered at the 250th cycle), whereas the discharge capacity of bare Si nanoparticles dropped to ~150 mA h g^{-1} (Fig. 24d). Unprotected silicon nanoparticles exhibited a rapid capacity decrease due to the loss of electrical connectivity owing to a continuous SEI layer growth. Kim *et al.* reported on the silicon–graphene composites from the silicon sludge waste and graphene oxide *via* the aerosol process and studied the relationship between the amount of rGO and the electrochemical performance.[279] The charge capacities of Si–rGO electrodes were 1626, 960, and 700 mA h g^{-1} for the GO contents of 0.1, 0.2, and 0.4 wt%, respectively. In perspective of the cycle retention until the 50th cycle, Si–rGO electrodes with 0.4 wt% GO content exhibited the most stable cycling performance over those with a lower GO content. Choi *et al.* demonstrated the formation of three-dimensional ordered mesoporous (3DOM) microspheres enwrapped with rGO nanosheets by spray pyrolysis (Fig. 24e–g).[280] $(NH_4)_2MoS_4$, polystyrene, and graphene oxide nanosheets were dissolved in the spray solution, where $(NH_4)_2MoS_4$ played the role of directly fabricating MoS_2 without other sulfur sources, and polystyrene was removed by decomposition under an inert atmosphere. The void spaces that originated from polystyrene, in addition to the rGO matrix, effectively buffered volume expansion, and the Na-ion diffusion length was decreased significantly. Consequently, the 3D MoS_2–graphene composite exhibited a high discharge capacity of 323 mA h g^{-1} for the 600th cycle when cycled at 1.5 A g^{-1} (Fig. 24h). The electrochemical properties of the rGO-composited materials prepared by spray processes are summarized in Table 2.[112,258–280]

3.5.4 Carbon nanotubes. Carbon nanotubes (CNTs) are 1-dimensional tubular graphitic carbon tubes with low density, high tensile strength, and high electrical conductivity.[282,283] CNT has attracted much research attention to be used as a 1D electron transport matrix that can be adopted for use in the electrode materials of rechargeable batteries.[284] Furthermore, the CNT network effectively functions as a mechanical buffer and embedded-in current collector.[285] Wei and his co-workers developed flexible $Li_4Ti_5O_{12}$/CNT LIB anodes by dispersing CNTs in the spray solution containing sucrose, lithium acetate, and tetra-*n*-butyltitanate and performing a subsequent spray drying (Fig. 25a–c).[286] A discharge capacity of 143 mA h g^{-1} could be achieved even at a high current density of 100C, due to the existence of the CNT matrix that significantly improved the Li-ion storage kinetics (Fig. 25d). The CNT network enabled facile Li-ion diffusion and electron transport along the 1-D CNT with high electrical conductivity. The anode material showed ultralong cyclability up to 8000 cycles at 1 A g^{-1}, with a capacity decay of less than 0.0014% per cycle, which verified the role of entangled CNTs that alleviated the volume change during cycling (Fig. 25e). Moon's group reported on the synthesis of macroporous CNT particles (M-CNTPs) by including polystyrene and CNTs in the spray solution and performing a subsequent spray drying process (Fig. 25f–i).[287] The polystyrene template was removed by heat treatment under an inert atmosphere, and M-CNTPs were subsequently impregnated with sulfur. Capillary action promoted sulfur penetration inside the microspheres due to the presence of macropores (Fig. 25i). The well-developed micropores in the agglomerated CNTs contained sulfur during cycling in a stable manner, leading to excellent electrochemical properties when applied as a sulfur host in in Li–S batteries (Fig. 25j and k). A similar structure was developed by Kim *et al.*, where Mn and Co nitrate were further added to the above solution to synthesize MnCoO–CNT microspheres *via* one-pot spray pyrolysis (Fig. 26a–f).[288] The homogeneously distributed CNTs enhanced the electrical conductivity and electrocatalytic activity, and nanopores that originated from polystyrene effectively accommodated Li_2O_2 and allowed high air permeability. Another study by Choi *et al.* reported the synthesis of fullerene-like $MoSe_2$ nanoparticle-embedded CNT balls for use in SIBs.[289] In the spray solution, acid-treated CNTs, PS nanobeads, and ammonium molybdate were added and spray-pyrolyzed at 700 °C under an Ar atmosphere. A complete thermal decomposition of ammonium molybdate and PS nanobeads occurred during the spray pyrolysis process, resulting in the formation of MoO_2 nanocrystal-embedded CNT balls with well-distributed nanovoids. MoO_2 nanocrystals reacted with hydrogen selenide (H_2Se) gas in the subsequent selenization step, resulting in the formation of a fullerene-like $MoSe_2$/CNT composite ball. When applied as the anode material for SIBs, the microspheres exhibited stable cycling performance, and a discharge capacity of 296 mA h g^{-1} could be obtained after 250 cycles at 0.2 A g^{-1}. Oh *et al.* synthesized hierarchical yolk–shell structured CNT–(NiCo)O/C microspheres from the spray pyrolysis process and employed them as the anode material in LIBs (Fig. 26g).[290] Nickel nitrate, cobalt nitrate, PVP, PS, and acid-treated CNTs were added to the spray solution and spray-pyrolyzed at 700 °C under a N_2 atmosphere. PVP has a tendency to migrate outward due to the phase separation from metal salts and produced an amorphous carbon shell. CNTs coalesced with PS nanobeads and underwent thermal contraction, leading to a skeleton-like porous yolk (Fig. 26h–j). The elemental dot mapping images of the microspheres show that the elements were well-distributed within the microsphere (Fig. 26k). The microspheres exhibited a discharge capacity of 598 mA h g^{-1} after 1000 cycles at a high current density of 5 A g^{-1} (Fig. 26l). Notably, a high discharge capacity of 294 mA h g^{-1} was obtained at an extremely high current density of 50 A g^{-1}, which is attributed to the high electrical conductivity of the skeleton yolk with interconnected mesopores and the presence of CNTs (Fig. 26m). The electrochemical properties of CNT–composite materials prepared from spray processes are listed in Table 2.[286–298]

3.6 Kirkendall diffusion

The Kirkendall effect, which was named after the scientist Ernest Kirkendall who discovered this process, basically refers to a mutual diffusion process that occurs at the interface of two metals when heated to a temperature that enables the metals' atomic diffusion.[299] Kirkendall reported that the mutual diffusion of zinc and copper resulted in the formation of empty lattice sites (vacancies) that originated from the

Table 2 Morphologies and electrochemical performances of nanostructured materials containing rGO or CNTs prepared from spray processes

Sample	Voltage window/ application	Synthesis method	Cycling performance[a]	Rate performance[b]	Ref.
3.5.3 Reduced graphene oxide					
Sb nanoparticle-embedded hollow carbon/rGO hybrid microspheres	0.001–2.5 SIB anode	Spray pyrolysis	320/500th/0.5	323/3.0	112
FeS–rGO composite powder with a crumpled structure	0.001–3.0 SIB anode	Spray pyrolysis	547/50th/0.5	340/6.0	258
WS_2-decorated 3D rGO microspheres	0.001–3.0 SIB anode	Spray pyrolysis	334/200th/0.2	287/0.9	259
$Ni_3Co_6S_8$–rGO composite powder	0.001–3.0 SIB anode	Spray pyrolysis	498/100th/0.5	361/5.0	260
MOF-derived N-doped porous carbon polyhedra anchored on crumpled graphene balls	1.0–3.0 Li–Se cathode	Spray pyrolysis	462/1000th/0.3375	409/3.375	261
Mesoporous WSe_2–rGO composite particles	0.001–3.0 SIB anode	Spray pyrolysis	238/100th/0.5	165/5.0	262
$MoSe_2$ Embedded CNT–rGO composite microspheres	0.001–3.0 SIB anode	Spray pyrolysis	393/200th/1.0	96/30.0	263
$FeTe_2$-decorated rGO hybrid microspheres	0.001–3.0 SIB anode	Spray pyrolysis	293/80th/0.2	257/3.0	264
V_2O_5–graphene ball composite	2.0–4.0 LIB cathode	Spray pyrolysis	214/100th/1.0	200/1.5	265
3D porous graphene–SnO_2 composite microspheres	0.001–3.0 LIB anode	Spray pyrolysis	1009/500th/2.0	660/9.0	266
Ni/NiO–graphene composite powder	0.001–3.0 LIB anode	Spray pyrolysis	863/300th/1.5	~685/3.0	267
WO_3–rGO composite powder	0.001–3.0 LIB anode	Spray pyrolysis	546/300th/0.1	438/0.5	268
SnO_2 flake/rGO/carbon composite powder	0.001–3.0 LIB anode	Spray pyrolysis	844/175th/1.0	~593/3.0	269
Graphene–MnO composite powder	0.001–3.0 LIB anode	Spray pyrolysis	701/130th/0.5	726/1.0	270
Crumpled graphene–MoO_3 composite powder	0.001–3.0 LIB anode	Spray pyrolysis	975/100th/1.0	845/3.0	271
Amorphous GeO_x-coated rGO balls with a sandwich structure	0.001–1.2 LIB anode	Spray pyrolysis	758/700th/2.0	450/9.0	272
Mesoporous CuO–rGO composite powder	0.001–3.0 LIB anode	Spray drying	676/200th/2.0	554/3.0	273
TiO_2–rGO nanocomposite hollow spheres	1.0–3.0 LIB anode	Spray drying	146/200th/0.94	109/3.74	274
Fe_3O_4-decorated hollow graphene balls	0.001–3.0 LIB anode	Spray pyrolysis	1050/300th/2.0	540/30.0	275
Ge nanoparticle-dispersed rGO balls	0.001–3.0 LIB anode	Spray pyrolysis	7483/200th/1.0	375/5.0	276
Crumpled graphene-encpasulated Si nanoparticles	0.02–2.0 LIB anode	Spray pyrolysis	940/200th/1.0	~554/4.0	277
$CoSe_x$–rGO composite powder	0.001–3.0 SIB anode	Spray pyrolysis	420/50th/0.3	357/1.0	278
Si–Graphene composite	0.005–2.0 LIB anode	Spray pyrolysis	~1335/50th/0.2	—	279
3D MoS_2–graphene microspheres	0.001–3.0 SIB anode	Spray pyrolysis	323/600th/1.5	234/10.0	280
3.5.4 Carbon nanotubes					
$Li_4Ti_5O_{12}$/CNT composite particles	1.0–2.8 LIB anode	Spray pyrolysis	~92/8000th/1.0	108/10.0	286
Spherical macroporous CNT particles	1.5–2.8 Li–S cathode	Spray drying	901/100th/0.836	—	287
Macroporous $(Mn_{1/3}Co_{2/3})O$–CNT microspheres	2–4.35 Li–O_2 cathode	Spray pyrolysis	245 cycles/500[c]	0.43/0.21[d]	288
Fullerene-like $MoSe_2$ nanoparticle-embedded CNT balls	0.001–2.5 SIB anode	Spray pyrolysis	296/250th/1.0	255/5.0	289
Hierarchical yolk–shell CNT–(NiCo)O/C microspheres	0.001–3.0 LIB anode	Spray pyrolysis	598/1000th/1.0	294/50.0	290
3D network GeO_x/MWCNT composite spheres	0.01–3.0 LIB anode	Spray pyrolysis	975/100th/0.5	365/10.0	291
Hollow Li_3VO_4/C/CNT composites	1.5–4.3 LIB cathode	Spray drying	272/500th/5.92	109/29.6	292
Hollow Fe_2O_3/CNT microspheres	0.001–3.0 LIB anode	Spray pyrolysis	1307/300th/1.0	703/15.0	293
Hollow $NiCo_2O_4$/CNT microspheres	0.001–3.0 LIB anode	Spray pyrolysis	1673/200th/1.0	639/20.0	294

Table 2 *(Contd.)*

Sample	Voltage window/ application	Synthesis method	Cycling performance[a]	Rate performance[b]	Ref.
Perforated SnO_2–CNT composite microspheres	0.001–3.0 LIB anode	Spray pyrolysis	$1108/250^{th}/1.5$	671/13.0	295
CNT–Zn_2GeO_4 composite microspheres	0.001–3.0 LIB anode	Spray pyrolysis	$762/350^{th}/1.5$	361/16.0	296
Multiroom-structured $(Ni_xFe_{1-x})_3Se_4$–GC–CNT hybrid microspheres	0.001–3.0 SIB anode	Spray pyrolysis	$455/100^{th}/0.3$	403/6.0	297
$CoSe_2$@NC-NR/CNT microspheres	0.001–3.0 SIB anode	Spray pyrolysis	$555/100^{th}/0.2$	517/5.0	298

[a] These data were arranged in the order discharge capacity/cycle number/current density. The units of discharge capacity and current density are mA h g^{-1} and A g^{-1}, respectively. [b] These data were arranged in the order discharge capacity/highest current density. [c] In the case of Li–O_2 batteries, values in this column correspond to lifespan/cutoff capacities [mA h g^{-1}]. [d] In the case of Li–O_2 batteries, the values in this column correspond to overpotential charge/discharge [V].

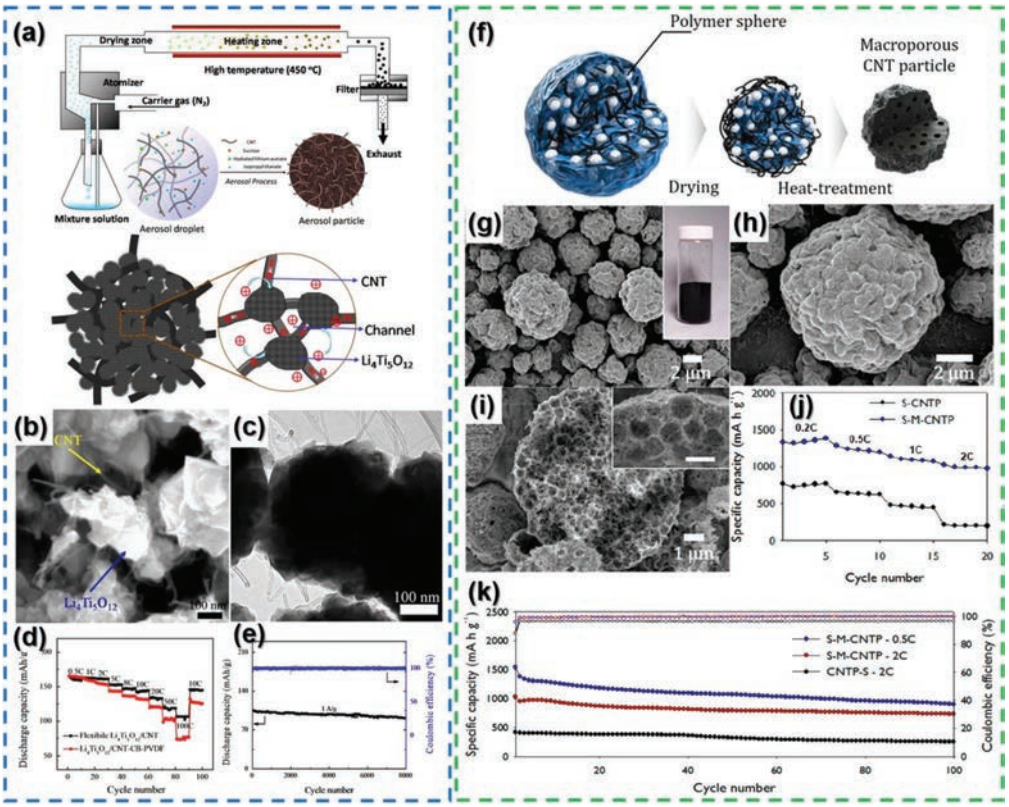

Fig. 25 (a) Schematic illustration of the synthetic process of nanostructured $Li_4Ti_5O_{12}$/CNT composites. (b) SEM and (c) TEM images of the composite, (d) cycling performance at 1 A g^{-1} and (e) rate performance of the $Li_4Ti_5O_{12}$/CNT composite microspheres. Reproduced with permission from ref. 286. Copyright 2014, Elsevier. (f) Schematic illustration of the synthetic process of M-CNTPs. (g) Low and (h) high-magnification SEM images of the M-CNTPs, and (i) cross-sectional SEM image of a cracked M-CNTP. (j) Rate and (k) cycling performances of the M-CNTPs applied as a cathode for Li–S batteries. Reproduced with permission from ref. 287. Copyright 2018, American Chemical Society.

diffusion of lattice atoms and the consequent movement of the initial interface, since the intrinsic diffusivity of Zn is higher than that of Cu at 785 °C. A study by Alivisatos *et al.* demonstrated that directional material flow occurs not only between metals, but also at the solid/gas interface, leading to void formation during metal sulfide growth.[300] During the sulfidation of cobalt, the outward flow of cobalt species in the cobalt sulfide shell triggered the vacancy supersaturation, leading to the formation of holes in the center. The two mechanisms were revealed to prevail in the formation of hollow structures: diffusion of metal ions along the filaments connecting unreacted cores and shells by surface diffusion and anchoring of the core to the wall of the shell in an asymmetrical manner.[301] In the first case, metal ions diffuse along the filaments toward the shell by surface diffusion.[302,303] Filaments become thinner as the void spaces become larger as

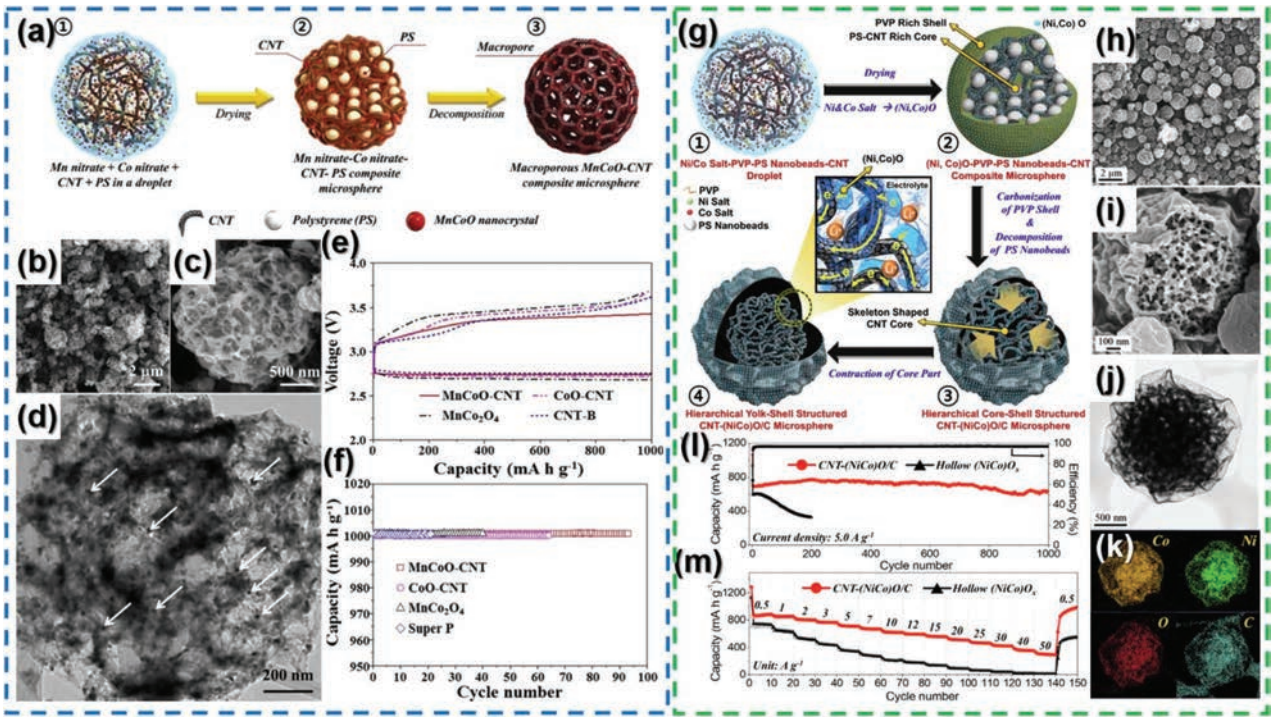

Fig. 26 (a) Schematic illustration of the synthetic process of the macroporous MnCoO–CNT composite microsphere. (b and c) SEM, (d) HRTEM images of the prepared microspheres, (e) initial discharge–charge profiles of the microspheres applied as a Li–O_2 battery cathode at 0.2 A g^{-1}, and (f) cycling performance with a restriction of the capacity to 1 A h g^{-1}. Reproduced with permission from ref. 288. Copyright 2017, Elsevier. (g) Schematic illustration of the synthetic process of the hierarchical yolk–shell structured CNT–(NiCo)O/C microsphere, (h) low and (i) high resolution SEM images, (j) TEM image, and (k) elemental dot mapping images of the microspheres and their (l) cycling and (m) rate performances. Reproduced with permission from ref. 290. Copyright 2019, Elsevier.

the reaction proceeds, and ultimately the filaments and the core vanish, and a hollow nanoparticle is consequently formed. If the core is anchored to the shell, a single void is formed between the core and the shell.[304,305] Since the shell and the core are adjacent to each other, the core species diffuses outward, forming a hollow morphology.

Some reports revealed that yolk–shell structures can also be synthesized from the Kirkendall effect.[306,307] The reason for the formation of the yolk–shell structure by the Kirkendall effect is presumably due to the incomplete diffusion of core species to the outer shell. Cho *et al.* studied the effect of synthesis temperature on the formation of nanofibers comprising the yolk–shell and hollow nanospheres by the electrospinning process.[308] The Sn–C composite nanofiber was oxidized at 400 °C and 500 °C, and the resultant fibers consisted of Sn@void@SnO_2 yolk–shells and hollow SnO_2 nanospheres, respectively. Insufficient heat applied to a nanosphere that undergoes the Kirkendall diffusion process could result in incomplete core species diffusion and thus in an unreacted core and reacted shell. It has been suggested that the breakage of filament that connects the shell and the core also results in yolk–shell structures.[301] Anderson *et al.* proposed that without a clear outward diffusion path for metal atoms, inward diffusion could be favored, leading to the formation of yolk–shell particles.[301]

The Kirkendall effect can be applied to microspheres obtained from spray processes, leading to the formation of hollow nanoparticles as well as hollow, core–shell, and yolk–shell nanoparticle aggregates formed from spray processes, and subsequent post heat treatment that triggers the nanoscale Kirkendall effect and their respective formation mechanisms are introduced in this section.

3.6.1 Hollow nanosphere aggregates. Cho *et al.* synthesized hollow microspheres consisting of hollow-structured NiO nanospheres *via* the spray pyrolysis process and demonstrated the application of the nanoscale Kirkendall effect (Fig. 27a).[115] An aqueous solution containing nickel nitrate and PVP was atomized by the use of ultrasonic power and subsequent pyrolysis, resulting in a debossed structure and decomposition of nickel nitrate, and formation of nickel oxide. The NiO-PVP composite microspheres were converted into Ni–C composite microspheres after the reduction heat treatment. The hollow morphology was obtained due to the Ostwald ripening process during oxidation, where larger crystals grow larger at the expense of nearby smaller crystals.[309] Crystal growth occurred from the outermost part of the spray-pyrolyzed microsphere, since they were firstly exposed to the heat energy. Larger NiO nanoparticles at the surface grew by devouring smaller nanocrystals, and due to the mass transport, the void space inside the microsphere was generated, and a hollow microsphere was

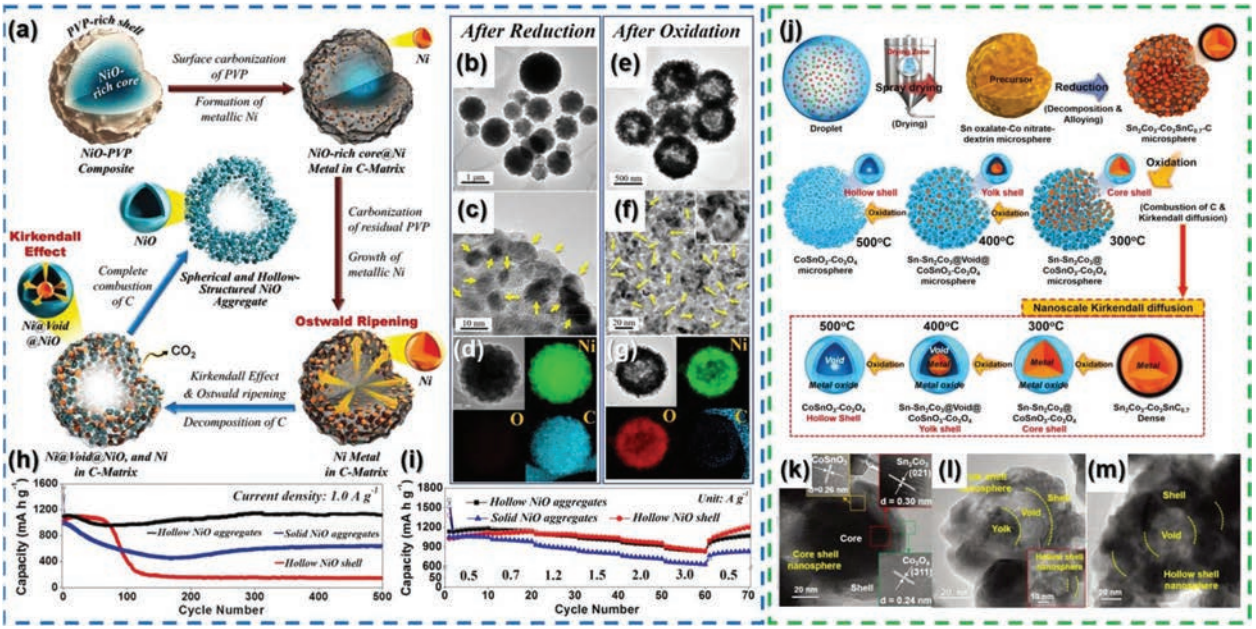

Fig. 27 (a) Schematic illustration of the synthetic process of the spherical and hollow-structured NiO aggregate. TEM, HR-TEM images, and elemental dot mapping images of (b–d) Ni–C composite powder and (e–g) hollow NiO aggregates. (h) Cycling performance of the microspheres at 1 A g^{-1} and (i) rate performance. Reproduced with permission from ref. 115. Copyright 2015, The Royal Society of Chemistry. (j) Schematic illustration of the synthetic process of the porous microspheres containing core–shell, yolk–shell, and hollow nanospheres. Magnified TEM images of the (k) core–shell, (l) yolk–shell, and (m) hollow nanospheres constituting the microspheres. Reproduced with permission from ref. 310. Copyright 2018, Wiley-VCH.

formed. During the reduction heat treatment, Ni metal growth was inhibited due to the carbon matrix surrounding the Ni metals (Fig. 27b–d). During the oxidation process, the nano-sized Ni metal was transformed into hollow NiO nanoparticles due to the difference in the diffusion rates between Ni cations and oxygen anions (Fig. 27e–g). Hollow microspheres consisting of hollow-structured NiO nanospheres exhibited improved cycling and rate performances in comparison with hollow NiO microspheres and solid NiO aggregates (Fig. 27h and i). Cho *et al.* synthesized micron-size spherical aggregates composed of hollow Fe_2O_3 nanospheres using spray pyrolysis.[93] Iron nitrate and sucrose were dissolved in the spray solution and spray-pyrolyzed to yield dense carbonaceous microspheres comprised of ultrasmall FeO_x nanocrystals. The subsequent reduction and oxidation step transformed the spray-pyrolyzed precursor into a Fe_2O_3 hollow nanosphere aggregate. The microspheres exhibited a stable performance until 100 cycles at 3 A g^{-1}, and the discharge capacity achieved was 854 mA h g^{-1} for the 100th cycle. In terms of the rate performance, the discharge capacity of 505 mA h g^{-1} could be delivered at a high current density of 10 A g^{-1}. Park *et al.* controlled the size of Co_3O_4 nanospheres, comprising the hollow microspheres by varying the reduction temperature, and a subsequent oxidation process.[116] The size of the hollow nanospheres constituting the hollow microspheres increased as the reducing heat treatment temperatures became higher. Thereby, it was confirmed that the size of the nanospheres could be tailored with ease. Another report by Park *et al.* suggested the possible formation of microspheres consisting of a core–shell, yolk–shell, and hollow nanospheres by increasing oxidation temperatures in a stepwise manner (Fig. 27j).[310] An oxidation temperature of 300 °C resulted in core–shell structured nanospheres due to the insufficient heat energy that restricted the Co and Sn species from diffusing outward and forming the oxide shell (Fig. 27k). Upon increasing the heat treatment temperature to 400 °C, microspheres comprising yolk–shell spheres could be obtained, since the heat energy was sufficiently high for some of the core part to diffuse outward, whereas it was insufficient for the core to completely diffuse to the shell part (Fig. 27l). Microspheres oxidized at 500 °C revealed hollow nanoparticle building blocks due to the complete diffusion of the core to the shell part (Fig. 27m). The initial discharge capacities of the samples showed similar values, and the discharge capacities of microspher es oxidized at 300, 400, and 500 °C after 200 cycles at 1 A g^{-1} were 1265, 987, and 569 mA h g^{-1}, respectively. The discharge capacity of the microspheres consisting of core–shell primary nanoparticles at 10 A g^{-1} was 608 mA h g^{-1}.

To further improve the electrochemical properties of hollow nanoparticle-aggregated microspheres, the nanostructures were composited with carbon materials including graphitic carbon, rGO, and N-doped carbon.[311–315] Park *et al.* synthesized microspheres consisting of hollow nanosphere-graphitic carbon composites by the spray drying process.[313] Iron nitrate and dextrin were dissolved in the aqueous spray solution and spray-dried to yield the Fe nitrate-dextrin precursor

microsphere. The precursor powder went through a reduction process at a high temperature of 900 °C, resulting in the formation of an iron metal and graphitic carbon shells. Graphitization of carbon species occurred at a relatively lower temperature, due to the presence of metallic Fe nanoparticles that decreased the activation energy of transformation from amorphous to graphitic carbon. The subsequent oxidation at 350 °C removed the remaining amorphous carbon materials and yielded hollow nanosphere aggregate-graphitic carbon composite microspheres. The prepared electrode material exhibited stable cycling performance for 1000 cycles for 3 A g^{-1}. In perspective of the rate performance, the Fe_2O_3–graphitic carbon composite exhibited around two times the discharge capacity compared to dense Fe_2O_3 microspheres at an extremely high current density of 30 A g^{-1}, owing to the additional electrical conductivity of graphitic carbon that enabled faster electron transport. Park *et al.* conducted research on the formation of nanobubble Co_3O_4-decorated rGO spheres, and their application as anode materials in the LIBs (Fig. 28a).[314] Colloidal graphene oxide nanosheets and cobalt nitrate were dissolved in an aqueous solution and were spray-pyrolyzed to obtain CoO_x–rGO micro-spherical precursor powder (Fig. 28b and c). The powder underwent a reduction step and a final oxidation step to produce hollow Co_3O_4 nanospheres decorated on the rGO microsphere. The hollow nanospheres were closely packed on the rGO sheets, as can be seen in the TEM images in Fig. 28d and e. As a result, nanobubble Co_3O_4-decorated rGO spheres exhibited enhanced cycling and rate performances (Fig. 28f and g). Recently, Kang's group reported the synthesis of a yolk–shell structure composed of N-doped carbon coated hollow $NiMoO_4$ nanospheres (Y-$NiMoO_4$-H@C) (Fig. 29a).[315] After the formation of yolk–shell-structured

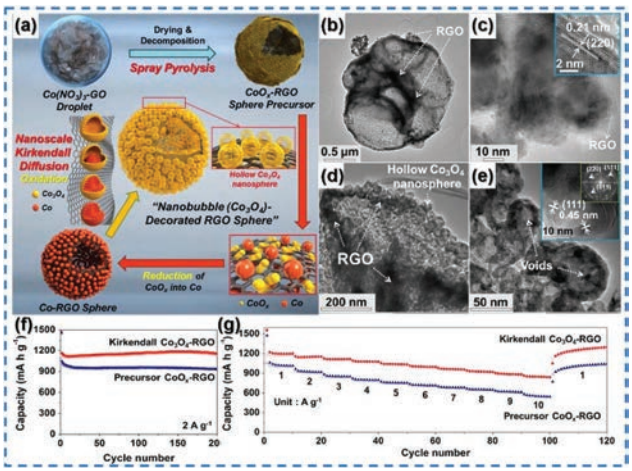

Fig. 28 (a) Schematic illustration of the synthetic process of the nanobubble (Co_3O_4)-decorated rGO sphere by the nanoscale Kirkendall diffusion process. Low and high resolution TEM images of (b and c) Co metal-decorated rGO spheres and (d and e) Co_3O_4-nanobubble rGO spheres, (f) cycling performance and (g) rate performance of the prepared microspheres. Reproduced with permission from ref. 314. Copyright 2015, Elsevier.

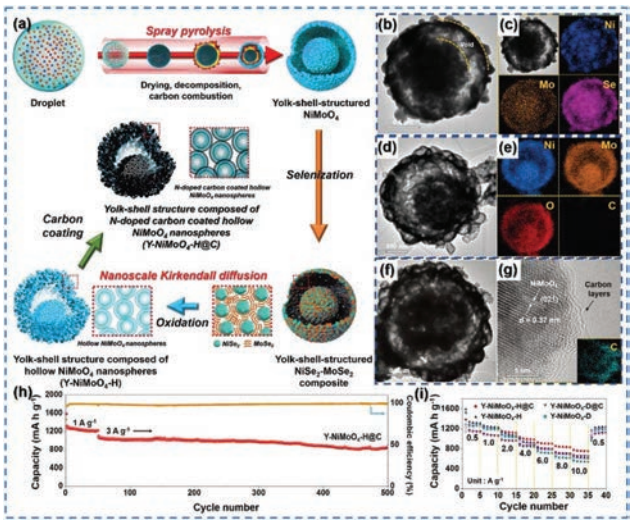

Fig. 29 (a) Schematic illustration of the synthetic process of the yolk–shell structure composed of N-doped carbon coated hollow $NiMoO_4$ nanospheres. TEM images and elemental dot mapping images of (b and c) $NiSe_2$–$MoSe_2$ composite microspheres and (d and e) the yolk–shell structure composite of hollow $NiMoO_4$ nanospheres. (f) TEM image, (g) HR-TEM image and elemental dot mapping image of the carbon-coated microspheres, (h) cycling and (i) rate performances of the prepared microspheres. Reproduced with permission from ref. 315. Copyright 2019, The Royal Society of Chemistry.

$NiMoO_4$ *via* the carbon combustion mechanism, the selenization process led to the formation of yolk–shell structured $NiSe_2$–$MoSe_2$ composite microspheres (Fig. 29b and c). During the final oxidation step, $NiSe_2$–$MoSe_2$ nanospheres were transformed into hollow $NiMoO_4$ nanospheres by the nanoscale Kirkendall diffusion (Fig. 29d and e). The nanostructure was then coated with polydopamine, and Y-$NiMoO_4$-H@C could be synthesized (Fig. 29f and g). The microspheres exhibited a stable cycling performance up to 500 cycles at 3 A g^{-1} and showed an improvement of rate capability when compared with their dense and carbon-free counterparts (Fig. 29h). The hollow structure and N-doped carbon coating effectively buffered the volume expansion during cycling, and N-doped carbon provided supplementary electrical conductivity to the microspheres, leading to an excellent electrochemical performance when employed as the anode in the LIB (Fig. 29i).

3.6.2 Hollow nanoplate aggregates. Remarkably, non-spherical hollow nanoplates and their aggregates can be fabricated by Kirkendall diffusion.[316–318] Park *et al.* synthesized hollow SnO_2 nanoplates with an aspect ratio unequal to unity *via* spray pyrolysis (Fig. 30a).[316] An aqueous solution containing Sn oxalate, selenous acid (H_2SeO_3), and PVP was spray-pyrolyzed at 900 °C under a 10% H_2/Ar gas atmosphere. During the pyrolysis process under a reducing atmosphere, Sn oxalate and H_2SeO_3 were decomposed, and thus Sn–Se–C composite microspheres were formed. Sn and Se underwent the alloying process, and dense SnSe nanoplates were formed resulting from the crystal growth in the favorable crystallographic direction. The nanoplates grew increasingly larger by consuming

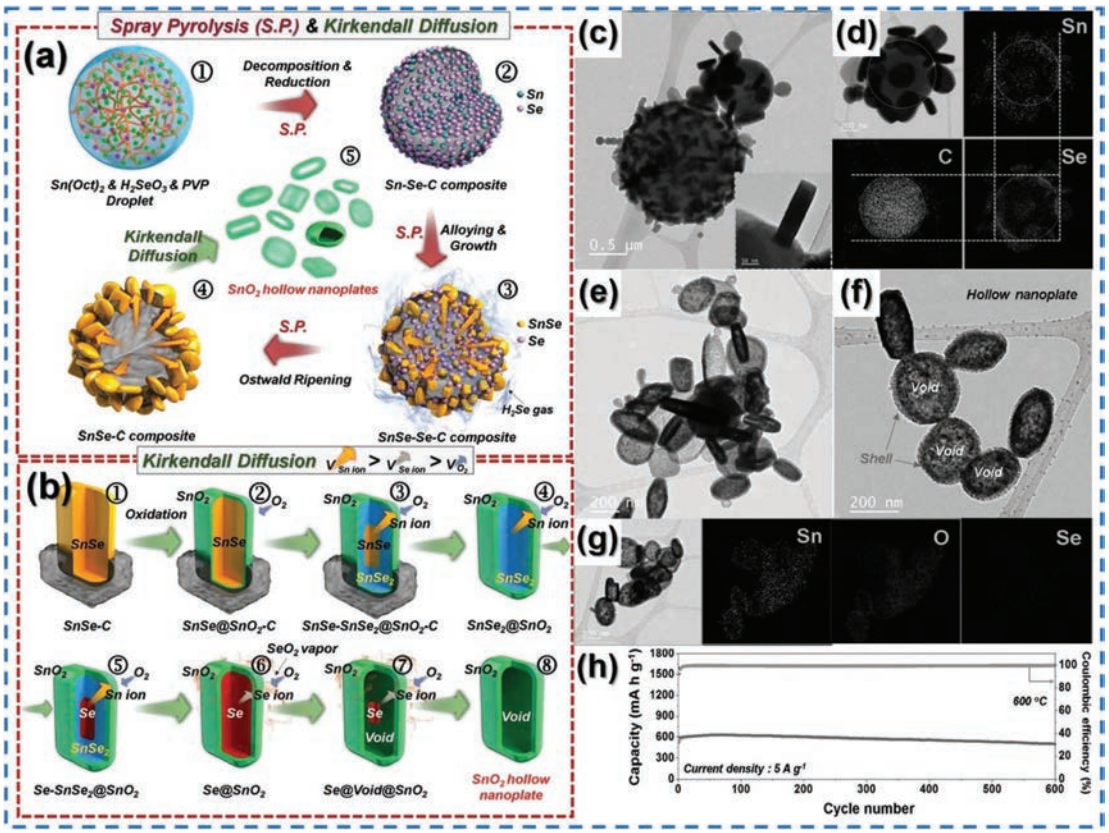

Fig. 30 Schematic illustration of the synthetic process of (a) hollow-structured SnO_2 nanoplates *via* the spray pyrolysis process and thermal oxidation in an air atmosphere and (b) SnO_2 hollow nanoplates *via* Kirkendall diffusion. TEM images and elemental dot mapping images of the (c and d) SnSe–C composite and (e–g) SnO_2 hollow nanoplates. (h) Cycling performance of the nanoplates at 5 A g^{-1}. Reproduced with permission from ref. 316. Copyright 2016, Wiley-VCH.

the nearby SnSe nanoplates, and carbon microspheres embedded with SnSe nanoplates were formed (Fig. 30c and d). Oxidation of the microspheres led to the combustion of carbon surrounding the SnSe nanoplates, and voids were formed due to the nanoscale Kirkendall diffusion (Fig. 30b). Ultimately aggregate-free hollow nanoplates could be obtained. A brief explanation for the formation of hollow SnO_2 nanoplates is given as follows: first, a thin SnO_2 shell was formed as a consequence of the reaction with the outermost Sn ions and oxygen. As the SnO_2 shell becomes thicker, Sn ions located at the core are consumed, producing the $SnSe@SnSe_2@SnO_2$ arrangement. This could be attributed to the diffusion speed of the Sn ion, Se ion, and O_2 gas, where the diffusion speed increases in the following order of O_2 gas, Se ion, and Sn ion. After the Sn ions completely react with oxygen, the Se species left in the core vaporize as SeO_2 gas, and a void is formed inside the SnO_2 shell. Oxidation of the nanoplates at 400 °C produced core–shell structured $SnSe_x@SnO_2$ nanoplates. Upon increasing the calcination temperature to 600 °C, hollow SnO_2 nanoplates could be obtained (Fig. 30e–g). When employed as the anode material in the LIB, a cycling stability up to 600 cycles at 5 A g^{-1} could be observed (Fig. 30h), and a discharge capacity of 267 mA h g^{-1} was delivered at an extremely high current density of 30 A g^{-1} due to the unique morphological characteristics. This strategy was applied to synthesize hierarchically structured SnO_2 microspheres comprised of hollow SnO_2 nanoplates.[317,318] A study by Park *et al.* exploited the use of Sn oxalate, sucrose, and polystyrene dissolved in aqueous solution to prepare 3DOM SnO_x–C composite microspheres resulting from the decomposition of the polystyrene well-distributed within.[318] The sulfidation of the microspheres yielded the 3DOM SnS_x–C composite, where dense SnS_x nanoplates and nanocrystals were embedded in the carbonaceous microspheres. Oxidation of the microspheres yielded hierarchically structured SnO_2 microspheres comprised of hollow SnO_2 nanoplates and SnO_2 nanocrystals comp rising the framework.

3.6.3 Hollow nanospheres. Won *et al.* reported on the synthesis of hollow nanospheres *via* flame spray pyrolysis.[319,320] First, nickel nitrate and TEOS were dissolved in the spray solution, and then they were flame spray-pyrolyzed, producing $NiO@SiO_2$ core–shell nanoparticles *via* phase separation.[319] The powder was then reduced under a H_2/Ar atmosphere to produce $Ni@SiO_2$ core–shell nanospheres. During the oxidation of $Ni@SiO_2$, Ni cations with a radius of 83 pm diffused outward, whereas the oxygen anions with a radius of 140 pm diffused inward, producing a void space within the nanoparticles. Owing to the void space that buffers the volume change during charging and discharging processes, the

capacity retention after 100 cycles at 0.5 A g^{-1}, measured from the second cycle, was 100.4%, whereas the filled NiO@SiO_2 nanoparticles had a capacity retention of only 41.7%. Cho *et al.* also prepared hollow SnO_2 nanospheres by spray drying of the aqueous solution containing Sn oxalate and PVP.[321] The spray-dried powder with a hollow interior due to the formation of a gas-impermeable layer during the process was then reduced under a H_2/Ar atmosphere, resulting in metallic Sn encapsulated in the carbon matrix. Oxidation of the Sn–C composite led to the formation of aggregate-free SnO_2 hollow nanospheres by the combustion of the amorphous carbon matrix and the nanoscale Kirkendall diffusion. The initial charge capacity of hollow SnO_2 nanospheres measured at the initial cycle was 680 mA h g^{-1}, while that of dense SnO_2 showed a similar value. After 300 cycles at 2 A g^{-1}, the discharge capacities of hollow and dense SnO_2 nanoparticles were 643 and 280 mA h g^{-1}, respectively, which proved their effectiveness at introducing a hollow space within the nanoparticles.

3.7 Other formation mechanisms

In this section, other formation mechanisms are introduced, including nanoparticle-embedded carbon microspheres, nanoparticles, and a cutting-edge strategy for the synthesis of nanostructure materials prepared *via* the spray process including N-doped CNT growth on spray-pyrolyzed microspheres. Primarily, various nanoparticle-embedded carbon composites such as pitaya-structured pyrite have been mainly synthesized by the liquid solution process for use as the anode for LIBs and SIBs, since this type of structure permits a high volumetric density owing to its spherical shape.[322,323] Secondly, examples of nanoparticles formed from spray processes are introduced. Finally, a new strategy that is capable of growing CNTs on the synthesized hollow, yolk–shell, and multiroom structured microspheres prepared from spray processes is introduced.

3.7.1 Pitaya-like structure. Synthesis of the aforementioned type of pitaya-like microsphere is possible by simple spray pyrolysis or drying and subsequent heat treatment.[324–326] Spray processes are considered ideal for the synthesis of this type of structure owing to the ease of its fabrication. Alloying type materials, like Sn and Sb, have been favored since the synthesis of electrode materials requires only one-step heat treatment. Wang's group synthesized uniform nano-Sn/C composite spheres for use in the LIB anode (Fig. 31a).[325] First, an ethanol-based solution containing tin chloride and PVP underwent the spray pyrolysis process under a 5% H_2/Ar gas atmosphere. The synthesized spheres were post-treated at 900 °C to yield nanosized Sn particles encapsulated in carbon microspheres. The Ostwald ripening of the once-small nanoparticles resulted in the formation of individual particles encapsulated within the carbonaceous microspheres. The TEM image of the synthesized microspheres shown in Fig. 31b reveals that Sn nanoparticles are homogeneously encapsulated in the carbon matrix. The first discharge capacity of the nano-Sn/C composite at 0.2 A g^{-1} was 710 mA h g^{-1}, which is close to the theoretical capacity of 756 mA h g^{-1}. This is attributed to the highly uniform nano-Sn nanospheres encapsulated in the carbon matrix that can fully utilize the Sn nanoparticles that can store Li-ions and resultantly achieve high discharge capacities. The TEM image of the microsphere after 50 cycles at 0.2 A g^{-1} shows no sign of structural destruction (Fig. 31c). The discharge capacity was almost the same as the initial capacity even after 130 cycles at 200 mA g^{-1}, which is attributed to the carbon matrix that effectively buffers the volume changes during the lithiation/delithiation processes (Fig. 31d). Chen's group also synthesized nano-Sb@C microspheres through the spray pyrolysis method using an ethanol solution containing resorcinol, formaldehyde, and $SbCl_3$ under an Ar atmosphere.[326] The spray-pyrolyzed particles were heat treated under an Ar atmosphere at 800 °C to yield nanoparticles for the nano-Sb@C composite with a similar morphology, which are employed as the anode material for SIBs (Fig. 31e and f). The nano-Sb@C composite microspheres exhibited a discharge capacity of 385 mA h g^{-1} after 500 cycles, and a capacity retention of 88% was achieved (Fig. 31g).

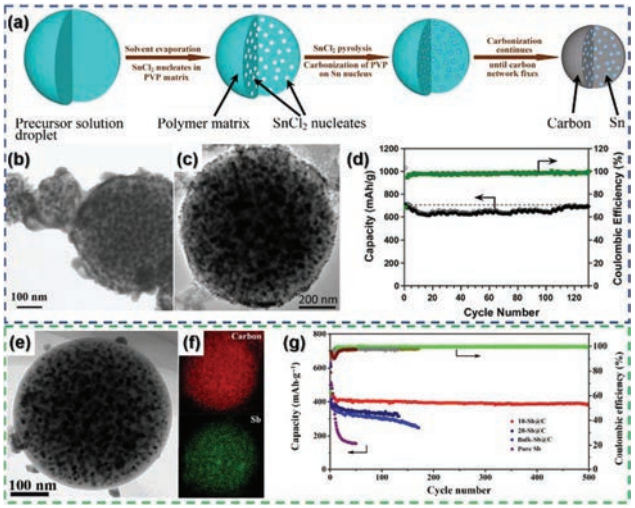

Fig. 31 (a) Schematic illustration of the synthetic process of ultrasmall nano-Sn dispersed carbon spheres. TEM images of nano-Sn/C composite particles (b) before cycling and (c) after 50 cycles. (d) Cycling performance of the microspheres at 0.2 A g^{-1}. Reproduced with permission from ref. 325. Copyright 2013, American Chemical Society. (e) TEM and (f) elemental dot mapping images of Sb/C composite microspheres and (g) their cycling performance at 0.1 A g^{-1}. Reproduced with permission from ref. 326. Copyright 2015, Springer Nature.

3.7.2 Nanoparticle formation. Some difficulties arise in the production of nanoparticles from spray pyrolysis and spray drying processes, and several methods have been proposed for their synthesis.[327–337] The most studied method is the synthesis of microspheres, or the ballooning of sprayed products, followed by the ball-milling process.[328–330] As mentioned earlier, microspheres with a desired composition can be formed by the spray processes. The synthesized particles are ball-milled to produce nanoparticles with a narrow size distribution and desired composition. Taniguchi and his coworkers demonstrated that $LiMnPO_4$ precursor microspheres

with a hollow morphology and a thin shell prepared from spray solution can be pulverized into $LiMnPO_4$/C nanoparticles by ball-milling $LiMnPO_4$ microspheres with acetylene black (Fig. 32a and b).[331] These nanoparticles were applied as the cathode for LIBs, and exhibited a stable performance over 100 cycles at current densities of 0.2, 0.5, and 1C. The discharge capacity retentions after 100 cycles were 80% and 92% at 0.2 and 0.5C rate, respectively (Fig. 32c). The nanoparticles also exhibited an excellent rate capability, and a discharge capacity of 65 mA h g^{-1} could be obtained at 10C rate (Fig. 32d).

Flame spray pyrolysis is used to facilitate the synthesis of nanoparticles owing to its powder formation mechanism.[332–337] The atomized droplets with a desired composition evaporate and undergo nucleation and growth, resulting in nanosized particles with a dense morphology.[332–337] Most of the particles prepared by spray pyrolysis or spray drying exhibit spherical morphologies, but those prepared by flame spray pyrolysis have unique morphologies depending on the surface energies and crystal growth behaviors of the materials.[338–348] Stark's group synthesized cubic BaF_2 nanoparticles by flame spray pyrolysis,[343] whereas Pratsinis and his co-workers synthesized nanorods by doping of In to ZnO, whose aspect ratio was not equal to unity.[344] Kim *et al.* likewise synthesized nanoparticles with various shapes and employed them as electrode materials in LIBs (Fig. 32e–j).[345] A high temperature of flame of >2500 °C and the subsequent quenching process led to the formation of various metastable polymorphs, which are difficult to obtain by general preparation methods that involve long reaction times at low temperatures. CoO_x–FeO_x composite nanoparticles were fabricated at various Co/Fe mole ratios, and nanoparticles with a Co : Fe ratio of 2 : 1 exhibited the highest capacity of 1101 mA h g^{-1} after 120 cycles at 1 A g^{-1} (Fig. 32k). Choi *et al.* synthesized core–shell structured NiO@TiO_2 nanoparticles by flame spray pyrolysis and employed them as anode materials in LIBs.[346] Mixed polygonal shapes including hexahedra, octahedra, dodecahedra, and triangular prisms were observed. The phase separation of the nucleated composite resulted in the formation of the NiO_2@TiO_2 core–shell structure, and the prepared particles exhibited a stable cycling performa nce for 80 cycles at 0.3 A g^{-1}. The discharge capacity of the NiO@TiO_2 composite nanoparticles for the 80th cycle was 970 mA h g^{-1}. Choi *et al.* synthesized $ZnMn_2O_4$ nanoparticles from flame spray pyrolysis and employed them as the anode material in LIBs.[347] The synthesized nanoparticles did not aggregate and exhibited a discharge capacity of 600 mA h g^{-1} after 40 cycles at 0.3 A g^{-1}. Park *et al.* prepared ultrafine TiO_2-doped MoO_3 nanoparticles by one-pot flame spray pyrolysis (Fig. 32l–n).[348] 5 wt% TiO_2-doped MoO_3 nanoplates were employed as the anode material for LIBs and exhibited a stable cycling performance until 200 cycles at 0.5 A g^{-1} (Fig. 32o). The reversible discharge capacities of TiO_2-doped MoO_3 nanoparticles at 0.2 A g^{-1} and 1 A g^{-1} were 1424 mA h g^{-1} and 978 mA h g^{-1}, respectively (Fig. 32p).

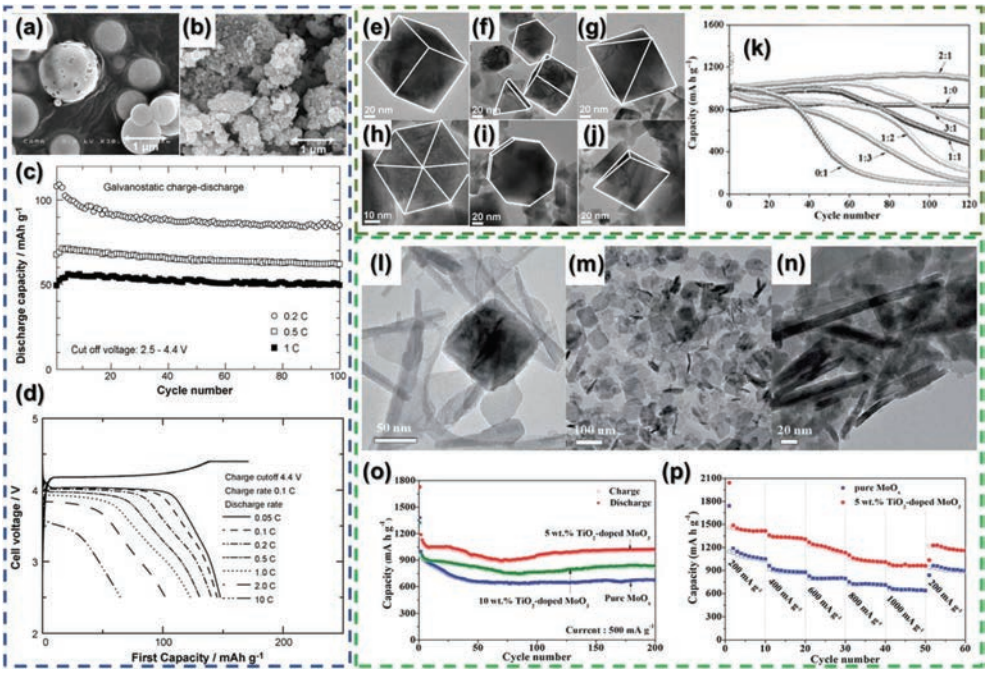

Fig. 32 (a) SEM image of (a) the $LiMnPO_4$ synthesized by spray pyrolysis and (b) the $LiMnPO_4$/C nanocomposite obtained after wet ball-milling. (c) Cycling and (d) rate performances of the $LiMnPO_4$/C nanocomposite. Reproduced with permission from ref. 331. Copyright 2010, Elsevier. TEM images of single- and multi-component nanoparticles with Co/Fe mole ratios of (e) 1 : 0, (f) 3 : 1, (g) 2 : 1, (h) 0 : 1, (i) 1 : 3, and (j) 1 : 2. (k) The cycling performances of the various samples at 1 A g^{-1}. Reproduced with permission from ref. 345. Copyright 2014, Wiley-VCH. TEM images of (l) pure MoO_x, (m) 5 wt% TiO_2-doped MoO_3, (n) 10 wt% TiO_2-doped MoO_3 nanoparticles and their (o) cycling and (p) rate performances. Reproduced with permission from ref. 348. Copyright 2014, The Royal Society of Chemistry.

3.7.2 N-doped CNT growth. Recently, three-dimensional hierarchically structured materials have received much attention, as they provide a large surface area and several advantages of individual building blocks, leading to unprecedented physicochemical properties.[349–354] Kang's group reported on the synthesis of hierarchical microspheres grafted with N-doped CNTs and their application in Li–S and Li–O_2 batteries (Fig. 33).[351–354] As the first example, hierarchical hollow microspheres grafted with Co nanoparticle-embedded bamboo-like N-doped CNT bundles were synthesized from the spray pyrolysis process and subsequent heat treatment (Fig. 33a).[351] Co_3O_4–MgO hollow microspheres were synthesized by the one-pot spray pyrolysis process from an aqueous spray solution containing cobalt nitrate and magnesium nitrate. The microspheres were put in an alumina boat and placed onto another large alumina boat containing dicyandiamide powder. After the large crucible was covered with the alumina cap, it was placed in a quartz tube and underwent heat treatment at 400 °C for 3 h and at 800 °C for 1 h, consecutively. During the post-treatment with dicyandiamide at 400 °C, cobalt oxide is reduced to cobalt metal, whereas magnesium oxide maintains its phase owing to its high thermal stability. The growth of Co metal particles is noticeably restricted by the presence of nearby MgO. Upon increasing the heat treatment temperature to 800 °C, dicyandiamide was decomposed and formed CH_x and NH_3 gases, resulting in the growth of bamboo-like N-doped CNTs on the interior and exterior of the hollow microspheres. This direct synthetic method for fabricating N-doped CNTs represents one of the general approaches.[355] The direct synthesis of N-doped CNTs can be described as the simultaneous occurrence of tube formation and N-doping during heat treatment under a NH_3 atmosphere.[355,356] Metal catalysts including cobalt, nickel, and iron are required to promote carbon precursor decomposition and tubular morphology formation.[355,356] Subsequently, MgO was etched with HCl and a porous shell was formed. This approach was applied to not only hollow microspheres, but also to yolk–shell and multiroom structures.[352,353] Oh *et al.*

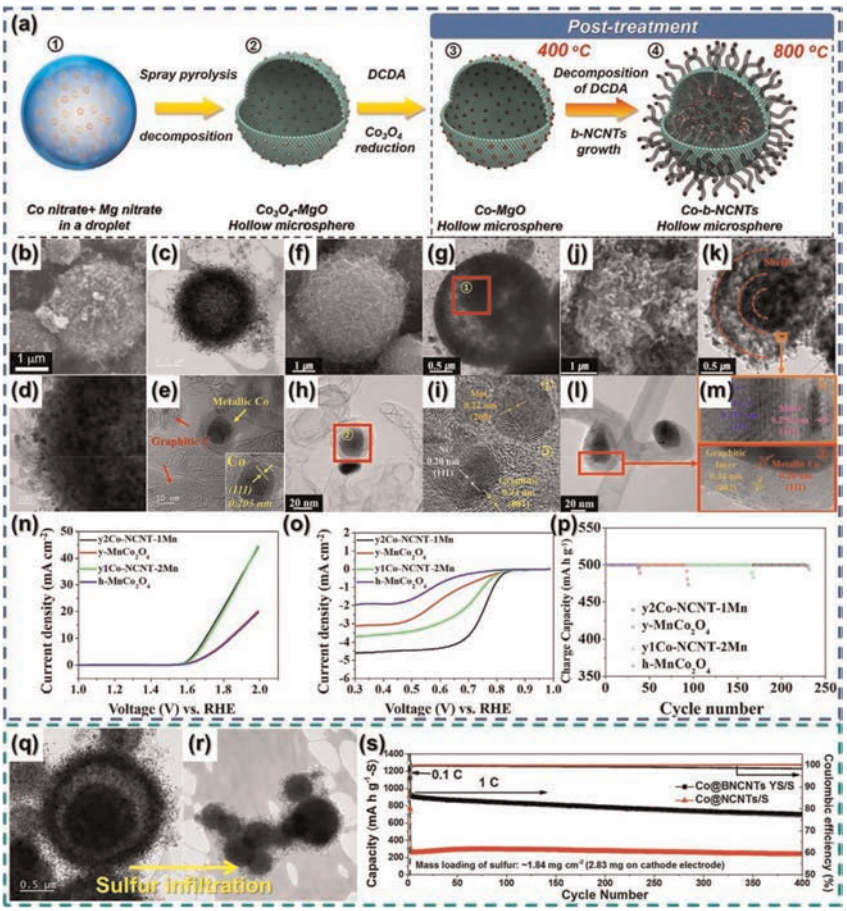

Fig. 33 (a) Schematic illustration of the synthetic process of Co–b-NCNT hollow microspheres. SEM image, TEM images, magnified TEM images, and HR-TEM images of (b–e) hollow, (f–i) multiroom, (j–m) yolk–shell microspheres prepared from N-CNT growth mechanism. (n) Oxygen evolution reaction (OER), (o) oxygen reduction reaction (ORR) polarization profiles, and (p) cycling performance of the microspheres. TEM images of Co@BNCNT YS microspheres. Reproduced with permission from ref. 351. Copyright 2017, Elsevier. Reproduced with permission from ref. 352. Copyright 2018, Elsevier. Reproduced with permission from ref. 353. Copyright 2019, Elsevier. (q) Before and (r) after sulfur infiltration, and their (s) cycling performance when applied as the cathode for Li–S batteries. Reproduced with permission from ref. 354. Copyright 2017, Wiley-VCH.

synthesized Co-encapsulated N-doped CNT-grown yolk–shell structured MnO–Mn_4N and Ni-embedded N-doped CNT-grown multiroom-structured MoC–C composite microspheres for use as cathode catalysts in Li–O_2 batteries.[352,353] The SEM and TEM images of the synthesized N-doped CNT-grown hollow, yolk–shell, and multiroom structures are shown in Fig. 33b–m. The advantages of architecting these types of microspheres when employed in Li–O_2 batteries include: (1) CNT growth leads to an increase in the specific surface area of the microspheres, and the N-doping itself acts as active sites, thus the total number of catalytic active sites is increased. (2) From the use of nanostructured microspheres as templates for CNT growth, the penetration of Li and O_2 gas is facilitated due to the existence of the porous shell. This ultimately leads to the formation and decomposition of Li_2O_2 inside the nanostructured microspheres. (3) During the heat treatment step using dicyandiamide, materials with phases that possess electrocatalytic activity such as MoC and Mn_4N are generated. C and N originate from the carbon and nitrogen source (CH_x and NH_3 gas) in dicyandiamide. (4) Li_2O_2 formed during electrochemical reactions is an insulating material. N-doped CNT supplements the electrical conductivities of these materials and thus enhances the electrochemical properties of the cathode material. Because of the aforementioned merits, N-doped CNT-grown microspheres exhibited improved electrochemical properties including the electrocatalytic activities for the oxygen reduction reaction and the oxygen evolution reaction, and a prolonged cycle life (Fig. 33n–p). Park *et al.* synthesized the Co-containing N-doped CNT-grown yolk–shell structure and used it as the sulfur host for Li–S batteries (Fig. 33q and r).[354] The microspheres exhibited high discharge capacities owing to the improvement of sulfur utilization by the formation of ultrafine S nanocrystals loaded within CNT-grafted microspheres, which can be converted into short-chain lithium polysulfides. A stable cycling performance until 400 cycles was observed at 1C rate, and 752 mA h g^{-1} was achieved at 2C rate (Fig. 33s). Excellent electrochemical properties can be attributed to the hierarchical CNT-grafted microspheres that offer sufficient space for sulfur loading and a strong chemical affinity of N-doped CNTs and the Co metal with sulfur.

4. Conclusions

In this review, the synthesis of nanostructured electrode materials *via* spray processes and their formation mechanisms were discussed in detail. As can be ascertained in this study, spray processes are powerful tools for the synthesis of innumerable electrode materials with distinct morphologies and functionalities for conventional LIBs as well as next-generation SIBs, Li–S, Li–Se, and Li–O_2 batteries. We classified the formation mechanisms of nanostructures prepared by spray processes into seven different categories. First, the influence of metal precursors and organic additives on the formation of nanostructured microspheres *via* spray processes was explained. Second, the formation mechanism of the yolk–shell structure was described by the ignition and combustion of spray-pyrolyzed or dried microspheres from a precursor solution containing a metal salt and carbon precursor. Next, the formation mechanisms for unique-structured microspheres synthesized from phase segregation, including multiroom, core–shell, yolk–shell, and Janus structures were investigated in detail. The inclusion of inorganic/organic templates in the spray solution resulted in the formation of nanovoids within the microspheres by the simple removal of template materials. Colloidal particles could be added to the spray solution to yield a superstructure consisting of pre-designed particles, Si nanospheres, and carbonaceous materials with high electrical conductivity, including rGO and CNTs. The nanoscale Kirkendall effect has been applied to the spray-processed products in the synthesis of microspheres consisting of nanosized hollow spheres and plates. Other formation mechanisms of nanostructures including pitaya-like structures, N-doped CNT-grown nanostructured microspheres, and nanoparticles were introduced in the final section. As is well known, spray processes are powerful methods for preparing materials with homogeneous compositions and controlled stoichiometry. The homogeneous morphologies of the synthesized particles are attributed to the reactions taking place in each atomized droplet. The spray processes yielded various novel nanostructures with desired morphologies and enhanced electrochemical characteristics when employed as electrode materials for various types of rechargeable batteries. However, there are still several issues and challenges to overcome. Unlike liquid-phase synthesis, it is often not straightforward for spray processes to precisely control the certain physicochemical properties of the final product. For example, pore (or void) sizes and their distribution in the internal structure cannot be tailored accurately since the pyrolysis step involves a number of sequential or simultaneous physical and chemical processes. In addition, crystallization and growth of metal compounds occur promptly owing to the short retention time at high temperature, limiting the preferential growth toward a certain crystallographic direction and phase control that may be crucial for promoting certain electrochemical properties. Therefore, it would be very promising to investigate the chemical interactions between the precursors in the droplet during pyrolysis by means of both experimental and theoretical approaches to get a glimpse of underlying formation mechanisms of the nanostructures. Integration of spray processes with other synthetic methods is another promising way to design advanced nanostructured materials. By doing so, the aforementioned disadvantages of spray processes would be compensated to a significant extent. We firmly believe that the continued search for new mechanisms and the synthesis of highly efficient electrode materials by spray processes could help resolve the challenges arising from energy demands.

Conflicts of interest

There are no conflicts to declare.

Acknowledgements

This work was supported by the National Research Foundation of Korea (NRF) grant funded by the Korea government (MSIP) (No. 2017R1A2B2008592).

References

1 P. G. Bruce, B. Scrosati and J. M. Tarascon, *Angew. Chem., Int. Ed.*, 2008, **47**, 2930–2946.
2 Y. G. Guo, J. S. Hu and L. J. Wan, *Adv. Mater.*, 2008, **20**, 2878–2887.
3 M. R. Lukatskaya, B. Dunn and Y. Gogotsi, *Nat. Commun.*, 2016, **7**, 12647.
4 N. W. Li, Y. X. Yin, S. Xin, J. Y. Li and Y. G. Guo, *Small Methods*, 2017, **1**, 1700094.
5 H.-M. Cheng and F. Li, *Science*, 2017, **356**, 582–583.
6 X. Zhang, X. Cheng and Q. Zhang, *J. Energy Chem.*, 2016, **25**, 967–984.
7 X. Li, Y. Chen, H. Huang, Y.-W. Mai and L. Zhou, *Energy Storage Mater.*, 2016, **5**, 58–92.
8 Y. Xu, M. Zhou and Y. Lei, *Adv. Energy Mater.*, 2016, **6**, 1502514.
9 B. Y. Guan, X. Y. Yu, H. B. Wu and X. W. D. Lou, *Adv. Mater.*, 2017, **29**, 1703614.
10 Y. Yang, C. Han, B. Jiang, J. Iocozzia, C. He, D. Shi, T. Jiang and Z. Lin, *Mater. Sci. Eng., R*, 2016, **102**, 1–72.
11 Y. Sun, N. Liu and Y. Cui, *Nat. Energy*, 2016, **1**, 16071.
12 K.-N. Jung, J. Kim, Y. Yamauchi, M.-S. Park, J.-W. Lee and J. H. Kim, *J. Mater. Chem. A*, 2016, **4**, 14050–14068.
13 Z. Li, H. B. Wu and X. W. D. Lou, *Energy Environ. Sci.*, 2016, **9**, 3061–3070.
14 X. Guo, S. Zheng, G. Zhang, X. Xiao, X. Li, Y. Xu, H. Xue and H. Pang, *Energy Storage Mater.*, 2017, **9**, 150–169.
15 X. Liu, J. Q. Huang, Q. Zhang and L. Mai, *Adv. Mater.*, 2017, **29**, 1601759.
16 L. J. Fu, H. Liu, C. Li, Y. P. Wu, E. Rahm, R. Holze and H. Q. Wu, *Prog. Mater. Sci.*, 2005, **50**, 881–928.
17 D. Jugović and D. Uskoković, *J. Power Sources*, 2009, **190**, 538–544.
18 S. Balaji, D. Mutharasu, N. Sankara Subramanian and K. Ramanathan, *Ionics*, 2009, **15**, 765–777.
19 K. Zhang, M. Park, L. Zhou, G. H. Lee, W. Li, Y. M. Kang and J. Chen, *Adv. Funct. Mater.*, 2016, **26**, 6728–6735.
20 K. Zhang, M. Park, L. Zhou, G. H. Lee, J. Shin, Z. Hu, S. L. Chou, J. Chen and Y. M. Kang, *Angew. Chem., Int. Ed.*, 2016, **55**, 12822–12826.
21 Q. Wang, W. Zhang, C. Guo, Y. Liu, C. Wang and Z. Guo, *Adv. Funct. Mater.*, 2017, **27**, 1703390.
22 C. Guo, W. Zhang, Y. Liu, J. He, S. Yang, M. Liu, Q. Wang and Z. Guo, *Adv. Funct. Mater.*, 2019, 1901925.
23 L. Shen, Y. Wang, F. Wu, I. Moudrakovski, P. A. van Aken, J. Maier and Y. Yu, *Angew. Chem., Int. Ed.*, 2019, **58**, 7238–7243.
24 J. M. Kim, D. Ko, J. Oh, J. Lee, T. Hwang, Y. Jeon, W. H. Antink and Y. Piao, *Nanoscale*, 2017, **9**, 15582–15590.
25 J. Choi, W.-S. Kim and S.-H. Hong, *Nanoscale*, 2018, **10**, 4370–4376.
26 N. Ye, T. Yan, Z. Jiang, W. Wu and T. Fang, *Ceram. Int.*, 2018, **44**, 4521–4537.
27 Y. Ma, P. Liu, Q. Xie, G. Zhang, H. Zheng, Y. Cai, Z. Li, L. Wang, Z.-Z. Zhu, L. Mai and D.-L. Peng, *Nano Energy*, 2019, **59**, 184–196.
28 S. Wang, Y. Fang, X. Wang and X. W. Lou, *Angew. Chem.*, 2019, **131**, 770–773.
29 N. Semagina and L. Kiwi-Minsker, *Catal. Rev.*, 2009, **51**, 147–217.
30 E. González, J. Arbiol and V. F. Puntes, *Science*, 2011, **334**, 1377–1380.
31 Y. Zhu, T. Mei, Y. Wang and Y. Qian, *J. Mater. Chem.*, 2011, **21**, 11457–11463.
32 J. Lai, W. Niu, R. Luque and G. Xu, *Nano Today*, 2015, **10**, 240–267.
33 L. Yu, X. Y. Yu and X. W. Lou, *Adv. Mater.*, 2018, **30**, 1800939.
34 Y. Lu, H. Fan, A. Stump, T. L. Ward, T. Rieker and C. J. Brinker, *Nature*, 1999, **398**, 223–226.
35 J. H. Bang and K. S. Suslick, *Adv. Mater.*, 2010, **22**, 1039–1059.
36 C. Boissiere, D. Grosso, A. Chaumonnot, L. Nicole and C. Sanchez, *Adv. Mater.*, 2011, **23**, 599–623.
37 A. B. D. Nandiyanto and K. Okuyama, *Adv. Powder Technol.*, 2011, **22**, 1–19.
38 D. S. Jung, Y. N. Ko, Y. C. Kang and S. B. Park, *Adv. Powder Technol.*, 2014, **25**, 18–31.
39 B. Vertruyen, N. Eshraghi, C. Piffet, J. Bodart, A. Mahmoud and F. Boschini, *Materials*, 2018, **11**, 1076.
40 Y. Liang, H. Tian, J. Repac, S.-C. Liou, J. Chen, W. Han, C. Wang and S. Ehrman, *Energy Storage Mater.*, 2018, **13**, 8–18.
41 Y. Lu, N. Zhang, Q. Zhao, J. Liang and J. Chen, *Nanoscale*, 2015, **7**, 2770–2776.
42 Y. Zhu, S. H. Choi, X. Fan, J. Shin, Z. Ma, M. R. Zachariah, J. W. Choi and C. Wang, *Adv. Energy Mater.*, 2017, **7**, 1601578.
43 P. Nie, G. Xu, J. Jiang, H. Dou, Y. Wu, Y. Zhang, J. Wang, M. Shi, R. Fu and X. Zhang, *Small Methods*, 2018, **2**, 1700272.
44 J. Leng, Z. Wang, J. Wang, H.-H. Wu, G. Yan, X. Li, H. Guo, Y. Liu, Q. Zhang and Z. Guo, *Chem. Soc. Rev.*, 2019, **48**, 3015–3072.
45 D. Hong, Y. Yamada, M. Sheehan, S. Shikano, C.-H. Kuo, M. Tian, C.-K. Tsung and S. Fukuzumi, *ACS Sustainable Chem. Eng.*, 2014, **2**, 2588–2594.
46 H.-M. Jeong, J.-H. Kim, S.-Y. Jeong, C.-H. Kwak and J.-H. Lee, *ACS Appl. Mater. Interfaces*, 2016, **8**, 7877–7883.
47 J. K. Kim, G. D. Park, J. H. Kim, S. K. Park and Y. C. Kang, *Small*, 2017, **13**, 1700068.
48 Z. Ye, J. Yang, B. Li, L. Shi, H. Ji, L. Song and H. Xu, *Small*, 2017, **13**, 1700111.

49 S.-Y. Jeong, J.-W. Yoon, T.-H. Kim, H.-M. Jeong, C.-S. Lee, Y. C. Kang and J.-H. Lee, *J. Mater. Chem. A*, 2017, **5**, 1446–1454.
50 H. Li, S. Ci, M. Zhang, J. Chen, K. Lai and Z. Wen, *ChemSusChem*, 2017, **10**, 4756–4763.
51 B.-Y. Kim, J.-W. Yoon, J. K. Kim, Y. C. Kang and J.-H. Lee, *ACS Appl. Mater. Interfaces*, 2018, **10**, 16605–16612.
52 T. Supasai, N. Henjongchom, I.-M. Tang, F. Deng and N. Rujisamphan, *Solar Energy*, 2016, **136**, 515–524.
53 J. Liu, Y. Lu, X. Cui, Y. Geng, G. Jin and Z. Zhai, *Sens. Actuators, B*, 2017, **248**, 862–867.
54 J. K. Kim, S.-K. Park and Y. C. Kang, *J. Alloys Compd.*, 2018, **763**, 652–661.
55 H. Jia, R. Jiang, W. Lu, Q. Ruan, J. Wang and J. C. Yu, *J. Mater. Chem. A*, 2018, **6**, 4783–4792.
56 S.-K. Park, J. K. Kim and Y. C. Kang, *ACS Sustainable Chem. Eng.*, 2018, **6**, 12706–12715.
57 J. S. Cho, D. S. Jung, S. K. Hong and Y. C. Kang, *J. Electroceram.*, 2009, **23**, 236–241.
58 S. K. Hong, H. Y. Koo, D. S. Jung and Y. C. Kang, *Appl. Phys. A*, 2006, **85**, 63–68.
59 J. H. Kim, H. Y. Koo, Y. N. Ko, J. H. Yi, Y. C. Kang, H. M. Lee and J. Y. Yun, *J. Ceram. Soc. Jpn.*, 2009, **117**, 1311–1316.
60 T. Li, X. Li, Z. Wang, H. Guo and Y. Li, *J. Mater. Chem. A*, 2015, **3**, 11970–11975.
61 S. H. Ju and Y. C. Kang, *J. Power Sources*, 2009, **189**, 185–190.
62 S. H. Ju, H. C. Jang and Y. C. Kang, *J. Power Sources*, 2009, **189**, 163–168.
63 B. Fan, X. Chen, A. Hu, Q. Tang, H. Fan, Z. Liu and K. Xiao, *RSC Adv.*, 2016, **6**, 79971–79977.
64 T. Li, X. H. Li, Z. Wang, H. Guo, Q. Hu and W. Peng, *Electrochim. Acta*, 2016, **209**, 456–463.
65 T. Li, X. Li, Z. Wang, H. Guo, W. Peng and K. Zeng, *Mater. Lett.*, 2015, **159**, 39–42.
66 H. Y. Koo, J. H. Kim, S. K. Hong, J. M. Han, Y. N. Ko, Y. C. Kang, S. H. Kang and S. B. Cho, *Met. Mater. Int.*, 2010, **16**, 941–946.
67 M. Kundu, G. Karunakaran, E. Kolesnikov, V. E. Sergeevna, S. Kumari, M. V. Gorshenkov and D. Kuznetsov, *J. Ind. Eng. Chem.*, 2018, **59**, 90–98.
68 C. Zhong, J.-Z. Wang, S.-L. Chou, K. Konstantinov, M. Rahman and H.-K. Liu, *J. Appl. Electrochem.*, 2010, **40**, 1415–1419.
69 X. Yin, Z. Wang, J. Wang, G. Yan, X. Xiong, X. Li and H. Guo, *Mater. Lett.*, 2014, **120**, 73–75.
70 C.-H. Lu, T.-Y. Wu, H.-C. Wu, M.-H. Yang, Z.-Z. Guo and I. Taniguchi, *Mater. Chem. Phys.*, 2008, **112**, 115–119.
71 B. Shao and I. Taniguchi, *Electrochim. Acta*, 2014, **128**, 156–162.
72 H. Y. Koo, S. K. Hong, S. H. Ju, I. S. Seo and Y. C. Kang, *J. Non-Cryst. Solids*, 2006, **352**, 3270–3274.
73 K. Y. Jung, J. H. Lee, H. Y. Koo, Y. C. Kang and S. B. Park, *Mater. Sci. Eng., B*, 2007, **137**, 10–19.
74 Y. Li, X. Li, Z. Wang, H. Guo and T. Li, *J. Alloys Compd.*, 2017, **696**, 836–843.
75 S. H. Ju, H. C. Jang, M.-J. Lee and Y. C. Kang, *J. Ceram. Process. Res.*, 2010, **11**, 138–143.
76 Y. N. Ko, S. H. Choi and Y. C. Kang, *ACS Appl. Mater. Interfaces*, 2016, **8**, 6449–6456.
77 G. D. Park, Y. N. Ko and Y. C. Kang, *Sci. Rep.*, 2014, **4**, 5785.
78 H. Y. Koo, D. R. Ko, S. H. Lee, S. M. Lee, Y. C. Kang and J.-H. Lee, *J. Alloys Compd.*, 2010, **503**, 260–265.
79 S. H. Ju, H. Y. Koo, S. K. Hong, E. B. Jo and Y. C. Kang, *J. Power Sources*, 2007, **174**, 598–602.
80 D. S. Jung, H. Y. Koo and Y. C. Kang, *J. Ceram. Process. Res.*, 2010, **11**, 425–431.
81 S. H. Lee, H. Y. Koo, J. H. Kim, Y. N. Ko, J. H. Yi, Y. C. Kang, H. M. Lee and J. Y. Yun, *Electron. Mater. Lett.*, 2010, **6**, 81–86.
82 K. M. Yang, Y. J. Hong, S. H. Choi, B. K. Park and Y. C. Kang, *Int. J. Electrochem. Sci.*, 2013, **8**, 1026–1040.
83 M. M. Rahman, S.-L. Chou, C. Zhong, J.-Z. Wang, D. Wexler and H.-K. Liu, *Solid State Ionics*, 2010, **180**, 1646–1651.
84 J. Liu, T. E. Conry, X. Song, M. M. Doeff and T. J. Richardson, *Energy Environ. Sci.*, 2011, **4**, 885–888.
85 M. H. Kim, D. S. Jung, Y. C. Kang and J. H. Choi, *Ceram. Int.*, 2009, **35**, 1933–1937.
86 D. S. Jung, S. K. Hong and Y. C. Kang, *J. Ceram. Soc. Jpn.*, 2008, **116**, 141–145.
87 K. H. Lee, B.-Y. Kim, J.-W. Yoon and J.-H. Lee, *Chem. Commun.*, 2019, **55**, 751–754.
88 Y. S. Jang, J. H. Kim, J. K. Lee and Y. C. Kang, *Int. J. Electrochem. Sci.*, 2013, **8**, 6807–6817.
89 A. Langrock, Y. Xu, Y. Liu, S. Ehrman, A. Manivannan and C. Wang, *J. Power Sources*, 2013, **223**, 62–67.
90 L. Yuan, K. Konstantinov, G. X. Wang, H. K. Liu and S. X. Dou, *J. Power Sources*, 2005, **146**, 180–184.
91 J. K. Kim, G. D. Park, J. H. Kim, J. H. Kim and Y. C. Kang, *Ceram. Int.*, 2017, **43**, 5534–5540.
92 W. Cho, J. H. Song, J.-H. Kim, G. Jeong, E. Y. Lee and Y.-J. Kim, *J. Appl. Electrochem.*, 2012, **42**, 909–915.
93 J. S. Cho, Y. J. Hong, J.-H. Lee and Y. C. Kang, *Nanoscale*, 2015, **7**, 8361–8367.
94 J. S. Cho, H. S. Ju, J.-K. Lee and Y. C. Kang, *Nanoscale*, 2017, **9**, 1942–1950.
95 J.-W. Yoon, J.-S. Kim, T.-H. Kim, Y. J. Hong, Y. C. Kang and J.-H. Lee, *Small*, 2016, **12**, 4229–4240.
96 G. D. Park, J. H. Kim and Y. C. Kang, *Mater. Charact.*, 2016, **120**, 349–356.
97 K. M. Jeon, J. S. Cho and Y. C. Kang, *J. Power Sources*, 2015, **295**, 9–15.
98 J.-S. Park, J. S. Cho and Y. C. Kang, *J. Power Sources*, 2018, **379**, 278–287.
99 J. H. Kim, J.-H. Lee and Y. C. Kang, *Electrochim. Acta*, 2014, **137**, 336–343.
100 J. H. Kim, H. Y. Koo, D. S. Jung, Y. N. Ko and Y. C. Kang, *Ceram. Int.*, 2010, **36**, 1171–1176.

101 S. H. Lee, H. Y. Koo, S. M. Lee and Y. C. Kang, *Ceram. Int.*, 2010, **36**, 611–615.
102 B. Ebin, G. Lindbergh and S. Gürmen, *J. Alloys Compd.*, 2015, **620**, 399–406.
103 N. Zhang, X. Han, Y. Liu, X. Hu, Q. Zhao and J. Chen, *Adv. Energy Mater.*, 2015, **5**, 1401123.
104 H. Y. Koo, D. S. Jung, S. H. Ju, S. K. Hong and Y. C. Kang, *Mater. Lett.*, 2006, **60**, 3091–3095.
105 S. H. Ju and Y. C. Kang, *Mater. Chem. Phys.*, 2008, **107**, 328–333.
106 D. Y. Kim, S. H. Ju, H. Y. Koo, S. K. Hong and Y. C. Kang, *J. Alloys Compd.*, 2006, **417**, 254–258.
107 H. Y. Koo, S. K. Hong, J. M. Han and Y. C. Kang, *J. Alloys Compd.*, 2008, **457**, 429–434.
108 D. S. Jung, S. H. Lee, J. M. Han, H. J. Hwang, J.-H. Lee and Y. C. Kang, *J. Ceram. Soc. Jpn.*, 2008, **116**, 969–974.
109 D. S. Jung, S. K. Hong, S. H. Ju, H. Y. Koo and Y. C. Kang, *Jpn. J. Appl. Phys.*, 2006, **45**, 116–120.
110 D. S. Jung, H. Y. Koo, S. H. Lee and Y. C. Kang, *Jpn. J. Appl. Phys.*, 2009, **48**, 116503.
111 S. K. Hong, D. S. Jung, S. H. Ju, H. Y. Koo and Y. C. Kang, *J. Mater. Sci.: Mater. Electron.*, 2006, **17**, 341–346.
112 J.-S. Park and Y. C. Kang, *Chem. Eng. J.*, 2019, **373**, 227–237.
113 G. Jian, Y. Xu, L.-C. Lai, C. Wang and M. R. Zachariah, *J. Mater. Chem. A*, 2014, **2**, 4627–4632.
114 J.-S. Park, J. S. Cho and Y. C. Kang, *J. Alloys Compd.*, 2019, **780**, 326–333.
115 J. S. Cho, J. M. Won, J.-H. Lee and Y. C. Kang, *Nanoscale*, 2015, **7**, 19620–19626.
116 J.-S. Park, J. S. Cho, J. H. Kim, Y. J. Choi and Y. C. Kang, *J. Alloys Compd.*, 2016, **689**, 554–563.
117 J. S. Cho, J. M. Won, J.-K. Lee and Y. C. Kang, *Nano Energy*, 2016, **26**, 466–478.
118 Y. J. Hong and Y. C. Kang, *RSC Adv.*, 2014, **4**, 58231–58237.
119 S. H. Ju and Y. C. Kang, *Ceram. Int.*, 2009, **35**, 1205–1210.
120 S. Ju, J. Kim and Y. Kang, *Met. Mater. Int.*, 2010, **16**, 299–303.
121 S. H. Ju and Y. C. Kang, *J. Power Sources*, 2010, **195**, 4327–4331.
122 K. Y. Jung, Y. C. Kang and Y. K. Park, *J. Ind. Eng. Chem.*, 2008, **14**, 224–229.
123 S. H. Ju and Y. C. Kang, *J. Power Sources*, 2008, **178**, 387–392.
124 H. Y. Koo, S. H. Lee and Y. C. Kang, *J. Ceram. Soc. Jpn.*, 2008, **116**, 955–959.
125 H. Y. Koo, S. H. Ju, S. K. Hong, D. S. Jung, Y. C. Kang and K. Y. Jung, *Jpn. J. Appl. Phys.*, 2006, **45**, 9083–9087.
126 W. Deng, S. Ci, H. Li and Z. Wen, *Chem. Eng. J.*, 2017, **330**, 995–1001.
127 M. H. Kim and Y. C. Kang, *Int. J. Electrochem. Sci.*, 2013, **8**, 3676–3686.
128 D. Y. Kim, S. H. Ju and Y. C. Kang, *Mater. Res. Bull.*, 2007, **42**, 362–370.
129 H. S. Kang, Y. C. Kang, H. Y. Koo, S. H. Ju, D. Y. Kim, S. K. Hong, J. R. Sohn, K. Y. Jung and S. B. Park, *Mater. Sci. Eng., B*, 2006, **127**, 99–104.
130 S. H. Ju, D. Y. Kim and Y. C. Kang, *Ceram. Int.*, 2007, **33**, 1093–1098.
131 S. H. Ju and Y. C. Kang, *Ceram. Int.*, 2009, **35**, 1633–1639.
132 S. H. Ju, D. Y. Kim, E. B. Jo and Y. C. Kang, *J. Alloys Compd.*, 2008, **450**, 457–462.
133 S. H. Ju, H. C. Jang and Y. C. Kang, *J. Ceram. Soc. Jpn.*, 2009, **117**, 922–925.
134 S. H. Ju, D. Y. Kim, E. B. Jo and Y. C. Kang, *J. Mater. Sci.*, 2007, **42**, 5369–5374.
135 Y. C. Kang, H. S. Roh, S. B. Park and K. Y. Jung, *Jpn. J. Appl. Phys.*, 2004, **43**, 5302–5306.
136 G. D. Park, J.-H. Lee, J.-K. Lee and Y. C. Kang, *Nano Res.*, 2014, **7**, 1738–1748.
137 C. Wu, X. Tong, Y. Ai, D.-S. Liu, P. Yu, J. Wu and Z. M. Wang, *Nano-Micro Lett.*, 2018, **10**, 40.
138 J.-O. Shim, Y. J. Hong, H.-S. Na, W.-J. Jang, Y. C. Kang and H.-S. Roh, *ACS Appl. Mater. Interfaces*, 2016, **8**, 17239–17244.
139 T.-H. Kim, C.-H. Kwak and J.-H. Lee, *ACS Appl. Mater. Interfaces*, 2017, **9**, 32034–32043.
140 J. S. Cho, K. M. Yang and Y. C. Kang, *CrystEngComm*, 2014, **16**, 6170–6174.
141 J. Liu, S. Z. Qiao, J. S. Chen, X. W. D. Lou, X. Xing and G. Q. M. Lu, *Chem. Commun.*, 2011, **47**, 12578–12591.
142 L. S. Lin, J. Song, H. H. Yang and X. Chen, *Adv. Mater.*, 2018, **30**, 1704639.
143 X. W. Lou, C. M. Li and L. A. Archer, *Adv. Mater.*, 2009, **21**, 2536–2539.
144 N. Liu, H. Wu, M. T. McDowell, Y. Yao, C. Wang and Y. Cui, *Nano Lett.*, 2012, **12**, 3315–3321.
145 W. Qiu, J. Jiao, J. Xia, H. Zhong and L. Chen, *Chem. – Eur. J.*, 2015, **21**, 4359–4367.
146 K. Kamata, Y. Lu and Y. Xia, *J. Am. Chem. Soc.*, 2003, **125**, 2384–2385.
147 T. Zhang, J. Ge, Y. Hu, Q. Zhang, S. Aloni and Y. Yin, *Angew. Chem., Int. Ed.*, 2008, **47**, 5806–5811.
148 D. Chen, L. Li, F. Tang and S. Qi, *Adv. Mater.*, 2009, **21**, 3804–3807.
149 Y. Chen, H. Chen, L. Guo, Q. He, F. Chen, J. Zhou, J. Feng and J. Shi, *ACS Nano*, 2009, **4**, 529–539.
150 Y. J. Hong, M. Y. Son and Y. C. Kang, *Adv. Mater.*, 2013, **25**, 2279–2283.
151 S. H. Choi and Y. C. Kang, *Chem. – Eur. J.*, 2014, **20**, 5835–5839.
152 L. Zhou, H. Xu, H. Zhang, J. Yang, S. B. Hartono, K. Qian, J. Zou and C. Yu, *Chem. Commun.*, 2013, **49**, 8695–8697.
153 J.-S. Park and Y. C. Kang, *J. Mater. Chem. A*, 2017, **5**, 8616–8623.
154 Y. N. Ko, Y. C. Kang and S. B. Park, *Nanoscale*, 2013, **5**, 8899–8903.
155 Y. N. Ko, S. B. Park and Y. C. Kang, *Chem. – Asian J.*, 2014, **9**, 1011–1015.
156 Y. J. Hong, K. C. Roh, J.-K. Lee and Y. C. Kang, *Nanoscale*, 2017, **9**, 17991–17999.
157 M. Y. Son, Y. J. Hong and Y. C. Kang, *Chem. Commun.*, 2013, **49**, 5678–5680.

158 M. Y. Son, Y. J. Hong, J.-K. Lee and Y. C. Kang, *Nanoscale*, 2013, **5**, 11592–11597.
159 J. H. Kim and Y. C. Kang, *Small*, 2017, **13**, 1701585.
160 S. H. Choi and Y. C. Kang, *ACS Appl. Mater. Interfaces*, 2014, **6**, 2312–2316.
161 C. M. Sim, Y. J. Hong and Y. C. Kang, *ChemSusChem*, 2013, **6**, 1320–1325.
162 Y. J. Hong, M. Y. Son, B. K. Park and Y. C. Kang, *Small*, 2013, **9**, 2224–2227.
163 S. H. Choi, J.-K. Lee and Y. C. Kang, *Nanoscale*, 2014, **6**, 12421–12425.
164 Y. N. Ko, S. B. Park, J.-H. Lee and Y. C. Kang, *RSC Adv.*, 2014, **4**, 40188–40192.
165 M. H. Kim, Y. J. Hong and Y. C. Kang, *RSC Adv.*, 2013, **3**, 13110–13114.
166 Y. N. Ko, Y. C. Kang and S. B. Park, *RSC Adv.*, 2014, **4**, 17873–17878.
167 S. H. Choi and Y. C. Kang, *ChemSusChem*, 2013, **6**, 2111–2116.
168 K. M. Yang, Y. J. Hong and Y. C. Kang, *ChemSusChem*, 2013, **6**, 2299–2303.
169 S. H. Choi and Y. C. Kang, *Chem. – Eur. J.*, 2014, **20**, 3014–3018.
170 J. Leng, Z. Wang, X. Li, H. Guo, H. Li, K. Shih, G. Yan and J. Wang, *J. Mater. Chem. A*, 2017, **5**, 14996–15001.
171 J. H. Ahn, G. D. Park, Y. C. Kang and J.-H. Lee, *Electrochim. Acta*, 2015, **174**, 102–110.
172 S. H. Choi and Y. C. Kang, *Small*, 2014, **10**, 474–478.
173 Y. N. Ko, S. H. Choi, S. B. Park and Y. C. Kang, *Nanoscale*, 2014, **6**, 10511–10515.
174 J. H. Kim and Y. C. Kang, *Nano Res.*, 2017, **10**, 3178–3188.
175 S. H. Choi and Y. C. Kang, *ACS Appl. Mater. Interfaces*, 2015, **7**, 24694–24702.
176 K. M. Yang, Y. N. Ko, J. Y. Yun and Y. C. Kang, *Chem. – Asian J.*, 2014, **9**, 443–446.
177 S. H. Choi and Y. C. Kang, *Chem. – Eur. J.*, 2013, **19**, 17305–17309.
178 J. H. Kim, Y. C. Kang, Y. J. Choi, Y. S. Kim and J.-H. Lee, *Electrochim. Acta*, 2014, **144**, 288–294.
179 C. M. Sim, S. H. Choi and Y. C. Kang, *Chem. Commun.*, 2013, **49**, 5978–5980.
180 S. H. Choi, Y. J. Hong and Y. C. Kang, *Nanoscale*, 2013, **5**, 7867–7871.
181 S. E. Skrabalak and K. S. Suslick, *J. Am. Chem. Soc.*, 2006, **128**, 12642–12643.
182 M. E. Fortunato, M. Rostam-Abadi and K. S. Suslick, *Chem. Mater.*, 2010, **22**, 1610–1612.
183 J. D. Atkinson, M. E. Fortunato, S. A. Dastgheib, M. Rostam-Abadi, M. J. Rood and K. S. Suslick, *Carbon*, 2011, **49**, 587–598.
184 C. Wang, Y. Wang, J. Graser, R. Zhao, F. Gao and M. J. O'Connell, *ACS Nano*, 2013, **7**, 11156–11165.
185 J. K. Kim, J. H. Kim and Y. C. Kang, *Chem. Eng. J.*, 2018, **333**, 665–677.
186 Y. J. Hong and Y. C. Kang, *Carbon*, 2015, **88**, 262–269.
187 Y. J. Hong and Y. C. Kang, *Nanoscale*, 2015, **7**, 701–707.
188 X. L. Fan, T. Gao, C. Luo, F. Wang, J. K. Hu and C. S. Wang, *Nano Energy*, 2017, **38**, 350–357.
189 Y. J. Hong and Y. C. Kang, *Small*, 2015, **11**, 2157–2163.
190 H. S. Ju, Y. J. Hong, J. S. Cho and Y. C. Kang, *Carbon*, 2016, **100**, 137–144.
191 Y. J. Hong, J. K. Lee and Y. C. Kang, *J. Mater. Chem. A*, 2017, **5**, 988–995.
192 A. Perro, S. Reculusa, S. Ravaine, E. Bourgeat-Lami and E. Duguet, *J. Mater. Chem.*, 2005, **15**, 3745–3760.
193 A. Walther and A. H. E. Müller, *Chem. Rev.*, 2013, **113**, 5194–5261.
194 S. H. Choi and Y. C. Kang, *Nanoscale*, 2013, **5**, 4662–4668.
195 G. D. Park, J. K. Lee and Y. C. Kang, *J. Mater. Chem. A*, 2017, **5**, 25319–25327.
196 S. H. Kim, B. Y. H. Liu and M. R. Zachariah, *Chem. Mater.*, 2002, **14**, 2889–2899.
197 H. S. Ju, J. S. Cho, J. H. Kim, Y. J. Choi and Y. C. Kang, *Phys. Chem. Chem. Phys.*, 2015, **17**, 31988–31994.
198 K. M. Jeon, J. H. Kim, Y. J. Choi and Y. C. Kang, *J. Appl. Electrochem.*, 2016, **46**, 469–477.
199 X. Fan, X. P. Jiang, W. Wang and Z. P. Liu, *Mater. Lett.*, 2016, **180**, 109–113.
200 H. Zhang, H. Xu, H. Jin, C. Li, Y. Bai and K. Lian, *RSC Adv.*, 2017, **7**, 30032–30037.
201 H. Ying, S. Zhang, Z. Meng, Z. Sun and W.-Q. Han, *J. Mater. Chem. A*, 2017, **5**, 8334–8342.
202 J. Qin, T. Wang, D. Liu, E. Liu, N. Zhao, C. Shi, F. He, L. Ma and C. He, *Adv. Mater.*, 2018, **30**, 1704670.
203 J. K. Kim, S.-K. Park, J.-S. Park and Y. C. Kang, *J. Mater. Chem. A*, 2019, **7**, 2636–2645.
204 J. H. Choi, S.-K. Park and Y. C. Kang, *Small*, 2019, **15**, 1803043.
205 C. Zheng, X. Hu, X. Sun, S. J. Yoo and X. Li, *Electrochim. Acta*, 2019, **306**, 339–349.
206 X. Hu, X. Sun, S. J. Yoo, B. Evanko, F. Fan, S. Cai, C. Zheng, W. Hu and G. D. Stucky, *Nano Energy*, 2019, **56**, 828–839.
207 M. S. Jo, S. Ghosh, S. M. Jeong, Y. C. Kang and J. S. Cho, *Nano-Micro Lett.*, 2019, **11**, 3.
208 R. Balgis, T. Ogi, W.-N. Wang, G. M. Anilkumar, S. Sago and K. Okuyama, *Langmuir*, 2014, **30**, 11257–11262.
209 S. H. Choi, Y. N. Ko, K. Y. Jung and Y. C. Kang, *Chem. – Eur. J.*, 2014, **20**, 11078–11083.
210 Y. N. Ko, S. B. Park, S. H. Choi and Y. C. Kang, *Sci. Rep.*, 2014, **4**, 5751.
211 S. H. Oh, J. K. Kim, Y. C. Kang and J. S. Cho, *Nanoscale*, 2018, **10**, 18734–18741.
212 F. Iskandar, A. B. D. Nandiyanto, K. M. Yun, C. J. Hogan Jr., K. Okuyama and P. Biswas, *Adv. Mater.*, 2007, **19**, 1408–1412.
213 Y. N. Ko, S. B. Park and Y. C. Kang, *Small*, 2014, **10**, 3240–3245.
214 Y. Yang, J. Li, J. Huang, J. Huang, J. Zeng and J. Zhao, *Electrochim. Acta*, 2017, **247**, 771–778.
215 Y. N. Ko, S. B. Park, K. Y. Jung and Y. C. Kang, *Nano Lett.*, 2013, **13**, 5462–5466.

216 A. K. Peterson, D. G. Morgan and S. E. Skrabalak, *Langmuir*, 2010, **26**, 8804–8809.
217 S. E. Skrabalak and K. S. Suslick, *J. Am. Chem. Soc.*, 2005, **127**, 9990–9991.
218 W. H. Suh, A. R. Jang, Y. H. Suh and K. S. Suslick, *Adv. Mater.*, 2006, **18**, 1832–1837.
219 H. Liu, Z. Shi, J. Zhang, L. Zhang and J. Zhang, *J. Mater. Chem.*, 2009, **19**, 468–470.
220 A. Naldoni, C. L. Bianchi, C. Pirola and K. S. Suslick, *Ultrason. Sonochem.*, 2013, **20**, 445–451.
221 H. Sohn, M. L. Gordin, T. Xu, S. Chen, D. Lv, J. Song, A. Manivannan and D. Wang, *ACS Appl. Mater. Interfaces*, 2014, **6**, 7596–7606.
222 L. Liu, Y. Wei, C. Zhang, C. Zhang, X. Li, J. Wang, L. Ling, W. Qiao and D. Long, *Electrochim. Acta*, 2015, **153**, 140–148.
223 D. Wang, A. Fu, H. Li, Y. Wang, P. Guo, J. Liu and X. S. Zhao, *J. Power Sources*, 2015, **285**, 469–477.
224 C. Zhao, L. Liu, H. Zhao, A. Krall, Z. Wen, J. Chen, P. Hurley, J. Jiang and Y. Li, *Nanoscale*, 2014, **6**, 882–888.
225 J.-L. Shi, H.-J. Peng, L. Zhu, W. Zhu and Q. Zhang, *Carbon*, 2015, **92**, 96–105.
226 G. D. Park, J. Lee, Y. Piao and Y. C. Kang, *Chem. Eng. J.*, 2018, **335**, 600–611.
227 G. D. Park, J. H. Kim, J.-K. Lee and Y. C. Kang, *J. Mater. Chem. A*, 2018, **6**, 21410–21418.
228 D. S. Jung, T. H. Hwang, J. H. Lee, H. Y. Koo, R. A. Shakoor, R. Kahraman, Y. N. Jo, M.-S. Park and J. W. Choi, *Nano Lett.*, 2014, **14**, 4418–4425.
229 L. Kong and I. Taniguchi, *J. Power Sources*, 2016, **312**, 36–44.
230 H. Du, K. Huang, M. Li, Y. Xia, Y. Sun, M. Yu and B. Geng, *Nano Res.*, 2018, **11**, 1490–1499.
231 H. Ma, F. Cheng, J. Y. Chen, J. Z. Zhao, C. S. Li, Z. L. Tao and J. Liang, *Adv. Mater.*, 2007, **19**, 4067–4070.
232 T. H. Hwang, Y. M. Lee, B.-S. Kong, J.-S. Seo and J. W. Choi, *Nano Lett.*, 2012, **12**, 802–807.
233 C. K. Chan, H. Peng, G. Liu, K. McIlwrath, X. F. Zhang, R. A. Huggins and Y. Cui, *Nat. Nanotechnol.*, 2008, **3**, 31–35.
234 B. Jerliu, E. Hüger, L. Dörrer, B.-K. Seidlhofer, R. Steitz, V. Oberst, U. Geckle, M. Bruns and H. Schmidt, *J. Phys. Chem. C*, 2014, **118**, 9395–9399.
235 D. S. Jung, T. H. Hwang, S. B. Park and J. W. Choi, *Nano Lett.*, 2013, **13**, 2092–2097.
236 X. Zhu, S. H. Choi, R. Tao, X. Jia and Y. Lu, *J. Alloys Compd.*, 2019, **791**, 1105–1113.
237 Q. Xu, J. Y. Li, J. K. Sun, Y. X. Yin, L. J. Wan and Y. G. Guo, *Adv. Energy Mater.*, 2017, **7**, 1601481.
238 S. J. Lee, H. J. Kim, T. H. Hwang, S. Choi, S. H. Park, E. Deniz, D. S. Jung and J. W. Choi, *Nano Lett.*, 2017, **17**, 1870–1876.
239 I. Taniguchi, D. Song and M. Wakihara, *J. Power Sources*, 2002, **109**, 333–339.
240 X. Jia, Z. Chen, X. Cui, Y. Peng, X. Wang, G. Wang, F. Wei and Y. Lu, *ACS Nano*, 2012, **6**, 9911–9919.
241 J. H. Kim and Y. C. Kang, *Nanoscale*, 2014, **6**, 4789–4795.
242 K.-C. Hsiao, S.-C. Liao and J.-M. Chen, *Electrochim. Acta*, 2008, **53**, 7242–7247.
243 H.-G. Jung, J. Kim, B. Scrosati and Y.-K. Sun, *J. Power Sources*, 2011, **196**, 7763–7766.
244 G.-W. Zhou, J. Wang, P. Gao, X. Yang, Y.-S. He, X.-Z. Liao, J. Yang and Z.-F. Ma, *Ind. Eng. Chem. Res.*, 2012, **52**, 1197–1204.
245 B. Zou, Y. Wang and S. Zhou, *Mater. Lett.*, 2013, **92**, 300–303.
246 Z. Zhang, W. Ren, Y. Wang, J. Yang, Q. Tan, Z. Zhong and F. Su, *Nanoscale*, 2014, **6**, 6805–6811.
247 X. Hou, J. Wang, M. Zhang, X. Liu, Z. Shao, W. Li and S. Hu, *RSC Adv.*, 2014, **4**, 34615–34622.
248 M. Y. Son, J.-K. Lee and Y. C. Kang, *Sci. Rep.*, 2014, **4**, 5752.
249 X. Zhu, Q. Li, Y. Fang, X. Liu, L. Xiao, X. Ai, H. Yang and Y. Cao, *Part. Part. Syst. Charact.*, 2016, **33**, 545–552.
250 D. Liu, Z. Kong, X. Liu, A. Fu, Y. Wang, Y.-G. Guo, P. Guo, H. Li and X. S. Zhao, *ACS Appl. Mater. Interfaces*, 2018, **10**, 2515–2525.
251 M. J. Allen, V. C. Tung and R. B. Kaner, *Chem. Rev.*, 2010, **110**, 132–145.
252 Y. Shao, J. Wang, H. Wu, J. Liu, I. A. Aksay and Y. Lin, *Electroanalysis*, 2010, **22**, 1027–1036.
253 R. Raccichini, A. Varzi, S. Passerini and B. Scrosati, *Nat. Mater.*, 2015, **14**, 271–279.
254 H.-G. Jung, Y. S. Jeong, J.-B. Park, Y.-K. Sun, B. Scrosati and Y. J. Lee, *ACS Nano*, 2013, **7**, 3532–3539.
255 L. Ji, M. Rao, H. Zheng, L. Zhang, Y. Li, W. Duan, J. Guo, E. J. Cairns and Y. Zhang, *J. Am. Chem. Soc.*, 2011, **133**, 18522–18525.
256 G. Kucinskis, G. Bajars and J. Kleperis, *J. Power Sources*, 2013, **240**, 66–79.
257 J. S. Cho, J.-K. Lee and Y. C. Kang, *Sci. Rep.*, 2016, **6**, 23699.
258 S. Y. Lee and Y. C. Kang, *Chem. – Eur. J.*, 2016, **22**, 2769–2774.
259 S. H. Choi and Y. C. Kang, *Nanoscale*, 2015, **7**, 3965–3970.
260 S. H. Choi and Y. C. Kang, *Nanoscale*, 2015, **7**, 6230–6237.
261 S.-K. Park, J.-S. Park and Y. C. Kang, *ACS Appl. Mater. Interfaces*, 2018, **10**, 16531–16540.
262 J. S. Cho, S.-K. Park, K. M. Jeon, Y. Piao and Y. C. Kang, *Appl. Surf. Sci.*, 2018, **459**, 309–317.
263 G. D. Park, J. H. Kim, S.-K. Park and Y. C. Kang, *ACS Appl. Mater. Interfaces*, 2017, **9**, 10673–10683.
264 J. S. Cho, S. Y. Lee, J.-K. Lee and Y. C. Kang, *ACS Appl. Mater. Interfaces*, 2016, **8**, 21343–21349.
265 S. H. Choi and Y. C. Kang, *Chem. – Eur. J.*, 2014, **20**, 6294–6299.
266 S. H. Choi, J.-K. Lee and Y. C. Kang, *Nano Res.*, 2015, **8**, 1584–1594.
267 S. H. Choi, Y. N. Ko, J.-K. Lee and Y. C. Kang, *Sci. Rep.*, 2014, **4**, 5786.
268 J. M. Won, M. Y. Son, J.-H. Seo and Y. C. Kang, *J. Alloys Compd.*, 2016, **688**, 647–653.

269 S. M. Lee, S. H. Choi and Y. C. Kang, *Chem. – Eur. J.*, 2014, **20**, 15203–15207.
270 S. M. Lee, S. H. Choi, J.-K. Lee and Y. C. Kang, *Electrochim. Acta*, 2014, **132**, 441–447.
271 S. H. Choi and Y. C. Kang, *ChemSusChem*, 2014, **7**, 523–528.
272 S. H. Choi, K. Y. Jung and Y. C. Kang, *ACS Appl. Mater. Interfaces*, 2015, **7**, 13952–13959.
273 G. D. Park and Y. C. Kang, *Chem. – Eur. J.*, 2015, **21**, 9179–9184.
274 A. Mondal, S. Maiti, K. Singha, S. Mahanty and A. B. Panda, *J. Mater. Chem. A*, 2017, **5**, 23853–23862.
275 S. H. Choi and Y. C. Kang, *Carbon*, 2014, **79**, 58–66.
276 J. K. Kim, G. D. Park and Y. C. Kang, *J. Korean Ceram. Soc.*, 2019, **56**, 65–70.
277 J. Luo, X. Zhao, J. Wu, H. D. Jang, H. H. Kung and J. Huang, *J. Phys. Chem. Lett.*, 2012, **3**, 1824–1829.
278 G. D. Park and Y. C. Kang, *Chem. – Eur. J.*, 2016, **22**, 4140–4146.
279 S. K. Kim, H. Kim, H. Chang, B.-G. Cho, J. Huang, H. Yoo, H. Kim and H. D. Jang, *Sci. Rep.*, 2016, **6**, 33688.
280 S. H. Choi, Y. N. Ko, J. K. Lee and Y. C. Kang, *Adv. Funct. Mater.*, 2015, **25**, 1780–1788.
281 D. Parviz, S. D. Metzler, S. Das, F. Irin and M. J. Green, *Small*, 2015, **11**, 2661–2668.
282 E. T. Thostenson, Z. Ren and T.-W. Chou, *Compos. Sci. Technol.*, 2001, **61**, 1899–1912.
283 L. Agüí, P. Yáñez-Sedeño and J. M. Pingarrón, *Anal. Chim. Acta*, 2008, **622**, 11–47.
284 J. J. Gooding, *Electrochim. Acta*, 2005, **50**, 3049–3060.
285 T. Kim, Y. H. Mo, K. S. Nahm and S. M. Oh, *J. Power Sources*, 2006, **162**, 1275–1281.
286 X. Jia, Y. Kan, X. Zhu, G. Ning, Y. Lu and F. Wei, *Nano Energy*, 2014, **10**, 344–352.
287 D. Gueon, J. T. Hwang, S. B. Yang, E. Cho, K. Sohn, D.-K. Yang and J. H. Moon, *ACS Nano*, 2018, **12**, 226–233.
288 J. H. Kim, Y. J. Oh and Y. C. Kang, *Carbon*, 2018, **128**, 125–133.
289 S. H. Choi and Y. C. Kang, *Nanoscale*, 2016, **8**, 4209–4216.
290 S. H. Oh, M. S. Jo, S. M. Jeong, Y. C. Kang and J. S. Cho, *Chem. Eng. J.*, 2019, **368**, 438–447.
291 W. He, H. Tian, X. Wang, F. Xin and W. Han, *J. Mater. Chem. A*, 2015, **3**, 19393–19401.
292 Y. Yang, J. Li, D. Chen and J. Zhao, *J. Electrochem. Soc.*, 2017, **164**, A6001–A6006.
293 S.-K. Park, G. D. Park and Y. C. Kang, *Nanoscale*, 2018, **10**, 11150–11157.
294 S.-K. Park, S. H. Yang and Y. C. Kang, *Chem. Eng. J.*, 2018, **349**, 214–222.
295 S. H. Choi, J.-H. Lee and Y. C. Kang, *ACS Nano*, 2015, **9**, 10173–10185.
296 S. H. Choi, J. H. Kim, Y. J. Choi and Y. C. Kang, *Electrochim. Acta*, 2016, **190**, 766–774.
297 G. D. Park and Y. C. Kang, *Nanoscale*, 2018, **10**, 8125–8132.
298 S.-K. Park and Y. C. Kang, *ACS Appl. Mater. Interfaces*, 2018, **10**, 17203–17213.
299 E. O. Kirkendall, *Trans. AIME*, 1942, **147**, 104–109.
300 Y. Yin, R. M. Rioux, C. K. Erdonmez, S. Hughes, G. A. Somorjai and A. P. Alivisatos, *Science*, 2004, **304**, 711–714.
301 B. D. Anderson and J. B. Tracy, *Nanoscale*, 2014, **6**, 12195–12216.
302 W. Wang, M. Dahl and Y. Yin, *Chem. Mater.*, 2012, **25**, 1179–1189.
303 H. J. Fan, M. Knez, R. Scholz, D. Hesse, K. Nielsch, M. Zacharias and U. Gösele, *Nano Lett.*, 2007, **7**, 993–997.
304 J. G. Railsback, A. C. Johnston-Peck, J. Wang and J. B. Tracy, *ACS Nano*, 2010, **4**, 1913–1920.
305 M. Ibáñez, J. Fan, W. Li, D. Cadavid, R. Nafria, A. Carrete and A. Cabot, *Chem. Mater.*, 2011, **23**, 3095–3104.
306 M. F. Sarac, W.-C. Wu and J. B. Tracy, *Chem. Mater.*, 2014, **26**, 3057–3064.
307 A. E. Henkes, Y. Vasquez and R. E. Schaak, *J. Am. Chem. Soc.*, 2007, **129**, 1896–1897.
308 J. S. Cho and Y. C. Kang, *Small*, 2015, **11**, 4673–4681.
309 P. W. Voorhees, *J. Stat. Phys.*, 1985, **38**, 231–252.
310 G. D. Park and Y. C. Kang, *Small*, 2018, **14**, 1703957.
311 G. D. Park, J. S. Cho and Y. C. Kang, *ACS Appl. Mater. Interfaces*, 2015, **7**, 16842–16849.
312 G. D. Park, J. S. Cho and Y. C. Kang, *Nanoscale*, 2015, **7**, 16781–16788.
313 G. D. Park, S.-K. Park and Y. C. Kang, *ACS Sustainable Chem. Eng.*, 2018, **6**, 11759–11767.
314 G. D. Park, J. S. Cho and Y. C. Kang, *Nano Energy*, 2015, **17**, 17–26.
315 G. D. Park, J. H. Hong, J.-K. Lee and Y. C. Kang, *Nanoscale*, 2019, **11**, 631–638.
316 G. D. Park, J. K. Lee and Y. C. Kang, *Adv. Funct. Mater.*, 2017, **27**, 1603399.
317 G. D. Park, J. H. Kim and Y. C. Kang, *Nanoscale*, 2018, **10**, 13531–13538.
318 G. D. Park and Y. C. Kang, *Nano Res.*, 2018, **11**, 1301–1312.
319 J. M. Won, J. H. Kim, Y. J. Choi, J. S. Cho and Y. C. Kang, *Ceram. Int.*, 2016, **42**, 5461–5471.
320 J. M. Won, J. S. Cho and Y. C. Kang, *J. Alloys Compd.*, 2016, **680**, 366–372.
321 J. S. Cho, H. S. Ju and Y. C. Kang, *Sci. Rep.*, 2016, **6**, 23915.
322 L. Ma, T. Chen, G. Zhu, Y. Hu, H. Lu, R. Chen, J. Liang, Z. Tie, Z. Jin and J. Liu, *J. Mater. Chem. A*, 2016, **4**, 15041–15048.
323 X. Xu, J. Liu, Z. Liu, J. Shen, R. Hu, J. Liu, L. Ouyang, L. Zhang and M. Zhu, *ACS Nano*, 2017, **11**, 9033–9040.
324 J. Guo, Z. Yang and L. A. Archer, *J. Mater. Chem. A*, 2013, **1**, 8710–8715.
325 Y. Xu, Q. Liu, Y. Zhu, Y. Liu, A. Langrock, M. R. Zachariah and C. Wang, *Nano Lett.*, 2013, **13**, 470–474.
326 N. Zhang, Y. Liu, Y. Lu, X. Han, F. Cheng and J. Chen, *Nano Res.*, 2015, **8**, 3384–3393.

327 M. Y. Son, J. H. Kim and Y. C. Kang, *Electrochim. Acta*, 2014, **116**, 44–50.
328 B. Shao and I. Taniguchi, *J. Power Sources*, 2012, **199**, 278–286.
329 T. N. L. Doan and I. Taniguchi, *J. Power Sources*, 2011, **196**, 5679–5684.
330 M. H. Kim, Y. C. Kang, S. M. Jeong, Y. J. Choi and Y. S. Kim, *Mater. Chem. Phys.*, 2013, **142**, 438–444.
331 T. N. L. Doan and I. Taniguchi, *J. Power Sources*, 2011, **196**, 1399–1408.
332 S. Sel, O. Duygulu, U. Kadiroglu and N. E. Machin, *Appl. Surf. Sci.*, 2014, **318**, 150–156.
333 S.-H. Ng, T. J. Patey, R. Büchel, F. Krumeich, J.-Z. Wang, H.-K. Liu, S. E. Pratsinis and P. Novák, *Phys. Chem. Chem. Phys.*, 2009, **11**, 3748–3755.
334 T. J. Patey, S. H. Ng, R. Büchel, N. Tran, F. Krumeich, J. Wang, H.-K. Liu and P. Novák, *Electrochem. Solid-State Lett.*, 2008, **11**, A46–A50.
335 A. Birrozzi, M. Copley, J. von Zamory, M. Pasqualini, S. Calcaterra, F. Nobili, A. Di Cicco, H. Rajantie, M. Briceno, E. Bilbé, L. Cabo-Fernandez, L. J. Hardwick, D. Bresser and S. Passerini, *J. Electrochem. Soc.*, 2015, **162**, A2331–A2338.
336 O. Waser, M. Hess, A. Güntner, P. Novák and S. E. Pratsinis, *J. Power Sources*, 2013, **241**, 415–422.
337 J. H. Kim and Y. C. Kang, *Int. J. Electrochem. Sci.*, 2013, **8**, 3379–3389.
338 J. A. Azurdia, A. McCrum and R. M. Laine, *J. Mater. Chem.*, 2008, **18**, 3249–3258.
339 R. Strobel and S. E. Pratsinis, *J. Mater. Chem.*, 2007, **17**, 4743–4756.
340 H. Schulz, W. J. Stark, M. Maciejewski, S. E. Pratsinis and A. Baiker, *J. Mater. Chem.*, 2003, **13**, 2979–2984.
341 L. Mädler, W. J. Stark and S. E. Pratsinis, *J. Mater. Res.*, 2002, **17**, 1356–1362.
342 X. Feng, D. C. Sayle, Z. L. Wang, M. S. Paras, B. Santora, A. C. Sutorik, T. X. Sayle, Y. Yang, Y. Ding, X. Wang and Y.-S. Her, *Science*, 2006, **312**, 1504–1508.
343 R. N. Grass and W. J. Stark, *Chem. Commun.*, 2005, 1767–1769.
344 M. J. Height, L. Mädler, F. Krumeich and S. E. Pratsinis, *Chem. Mater.*, 2006, **18**, 572–578.
345 J. H. Kim, J.-H. Lee and Y. C. Kang, *Chem. – Asian J.*, 2014, **9**, 2826–2830.
346 S. H. Choi, J.-H. Lee and Y. C. Kang, *Nanoscale*, 2013, **5**, 12645–12650.
347 S. H. Choi and Y. C. Kang, *Int. J. Electrochem. Sci.*, 2013, **8**, 6281–6290.
348 G. D. Park, S. H. Choi and Y. C. Kang, *RSC Adv.*, 2014, **4**, 17382–17386.
349 J. Luo, J. Liu, Z. Zeng, C. F. Ng, L. Ma, H. Zhang, J. Lin, Z. Shen and H. J. Fan, *Nano Lett.*, 2013, **13**, 6136–6143.
350 K. Cao, L. Jiao, H. Liu, Y. Liu, Y. Wang, Z. Guo and H. Yuan, *Adv. Energy Mater.*, 2015, **5**, 1401421.
351 J. H. Kim, S.-K. Park, Y. J. Oh and Y. C. Kang, *Chem. Eng. J.*, 2018, **334**, 2500–2510.
352 Y. J. Oh, J. H. Kim, S.-K. Park, J.-S. Park, J.-K. Lee and Y. C. Kang, *Chem. Eng. J.*, 2018, **351**, 886–896.
353 Y. J. Oh, J. H. Kim and Y. C. Kang, *Chem. Eng. J.*, 2019, **373**, 86–94.
354 S.-K. Park, J. K. Lee and Y. C. Kang, *Adv. Funct. Mater.*, 2018, **28**, 1705264.
355 Z. Wang, R. Jia, J. Zheng, J. Zhao, L. Li, J. Song and Z. Zhu, *ACS Nano*, 2011, **5**, 1677–1684.
356 D. H. Lee, W. J. Lee and S. O. Kim, *Nano Lett.*, 2009, **9**, 1427–1432.